NOVEL PHASE-MODULATED OPTICAL FIBER SENSORS

by

Kent Austin Murphy

Dissertation submitted to the Faculty of the

Virginia Polytechnic Institute and State University

in partial fulfillment of the requirements for the degree of

DOCTOR OF PHILOSOPHY

in Electrical Engineering

APPROVED:

Richard O. Claus

R.O. Claus, Chairman

S. B. Desu

J. C. Duke

G. J. Indebetouw

T. C. Poon

August, 1992

Blacksburg, Virginia

NOVEL PHASE-MODULATED OPTICAL FIBER SENSORS

by

Kent Austin Murphy
Richard O. Claus, Chairman
Electrical Engineering

(ABSTRACT)

Optical fiber systems have been developed during the past twenty-five years with primary applications in long distance, high speed digital information communication. Optical fiber sensors have also been developed over the past fifteen years for the nondestructive inspection and evaluation of materials used in the aerospace, energy, transportation, and medical industries. Optical fibers may be used as the field-sensitive elements in sensors for the measurement of environmental parameters such as displacement, strain, temperature, vibration, chemical concentrations and electromagnetic fields. Their advantages for such measurements include 1) an inherent immunity to electromagnetic interference (EMI), 2) avoidance of ground loops, 3) the capability of responding to a wide variety of measurands, 4) excellent resolution, 5) the avoidance of sparks, especially important for applications within explosive environments, and 6) operation at temperatures of approximately 800°C for silica waveguides and above 1900°C for sapphire waveguides.

Phase-modulated optical fiber sensors have been shown to possess the highest sensitivities to a given measurand. This dissertation describes several novel phase-modulated optical fiber sensors. The sensors described include a strain gage, a temperature sensor for applications up to and including 1700°C, a displacement sensor with sub-Angstrom resolution, and a vibration mode filter. For each sensing concept, a description and method of operation is given, followed by fabrication methods and experimental results.

Acknowledgements

This work has been possible due to the contributions and support of several people and organizations.

I wish to thank the members of my committee Profs. R. O. Claus, S. B. Desu, J. C. Duke, G. J. Indebetouw, and T. C. Poon. It has been a pleasure and an honor to work with each of them.

I would like to express my appreciation to Prof. R. O. Claus, my advisor and mentor, for giving me the opportunity to attend graduate school and to work at FEORC, and for helping me grow professionally. Prof. R. O. Claus truly changed the course of my life.

I am grateful to Dr. Ashish M. Vengsarkar, a true friend, for supporting me every step of the way throughout my years as a graduate student. I also wish to thank Dr. Anbo Wang, Mike Gunther, R. F. Hellbaum, Russell May, Chris Koob, Jonathan Greene, Brian Fogg, Mark Miller, Tuan Tran, Suzanne Starr, George Wang, and Sridhar Gollapudi for their valuable suggestions and assistance during the experimentation, data gathering and presentation of this work. Also, thanks to all of the staff and students at FEORC.

A special thanks to my parents for giving me the freedom to try new things and the resources to get them all started.

Finally, my biggest thanks to my wife, Cheryl, and two sons, Brent and Brice. Cheryl made many sacrifices so that I could pursue my goals, and offered constant encouragement, inspiration, and support. She was always there when I needed her. I apologize, to the three of them, for neglecting them over the past few years.

Financial support for this work was provided by NASA Langley, the Department of Energy, Wright Patterson Air Force Base, Litton, McDonnell Douglas, and the Virginia Center for Innovative Technology.

Table of Contents

List of Figures

1. Introduction

The physical integrity of the materials used to construct buildings, bridges, dams, refineries, mines, energy production facilities, aerospace and ground-based transportation vehicles, and various military weapons platforms is of natural concern for both safety and economic reasons. Optical fiber sensors are an attractive and viable means of monitoring the structural health due to their electromagnetic interference immunity, ground loop avoidance, large range of operating temperature, small size, light weight, multiplexing capabilities, and high sensitivities.

During the past fifteen years, a variety of environmental sensors which employ optical fibers as the sensing elements have been developed and demonstrated [1-3]. External perturbations such as strain, pressure, temperature, acoustic waves and vibrations induce a change in the phase, intensity, wavelength, polarization and/or modal content of the electromagnetic wave propagating through the optical fiber. This change in one or more properties of light can then be related to the measurand. Phase modulated, or interferometric fiber optic sensors often possess the highest sensitivities to a given measurand. As an example, a fiber optic interferometric strain gage exhibits 0.001 microstrain resolution whereas the conventional resistive element strain gages possess 10.0 microstrain resolution.

Fiber optics is a likely choice in the aerospace industry with the growing use of composite materials and the move toward higher performance with sophisticated flight control systems which will necessitate the use of a complex network of sensors that can monitor several parameters simultaneously over the entire lifetime of the structure. The monitoring needs throughout the lifetime of the structure will include:

i) Birth: To monitor the curing process of the composite laminate during manufacture.
ii) Lifetime: To assess damage and effects such as structural vibrations, strain and stress concentrations due to adverse environmental conditions. This information can be fed back to a control system to ensure aerodynamic stability.
iii) Degradation: To inform the central command about events that could lead to

catastrophic failures. A prediction system would prevent disastrous accidents and detect significant flaws such as excessive thermal build-up, pressure leaks and unwanted vibrations, which could indicate needed inspections.

Large structures can also be instrumented with sensors and actuators so that they respond to changes in the surrounding environment. For example, tall buildings can be constructed with embedded fiber optic sensors and control actuators so that the buildings automatically respond to wind forces or to earthquake-induced surface motions. The fiber optic sensors can then be used to detect vibration and map strain in critical components of the building. These sensors would provide the data necessary for a central control system that would drive the actuators to compensate for unwanted vibrations and prevent catastrophic failures. The sensing, decision making, and actuation would have to take place in the fraction of a second in order to maintain control of the large structure.

Possible applications of fiber optic sensor systems for bridges include the mapping of strain in bridge components, evaluating bridge joints, and detection and monitoring of corrosion and crack propagation. Fiber sensors can be embedded in concrete to monitor strain transfer between the concrete and the embedded reinforcement rods. Implementing fiber sensors for corrosion detection would provide advance warning of repair needs before catastrophic failure. Fiber sensors can also detect temperature and moisture levels on the bridge to provide early hazard warnings to motorists or automatically dispense deicing chemicals. Networks of multiplexed fiber sensors measuring multiple measurands can be used for instrumenting buildings, bridges, or dams for a variety of parameters concerning safety and operating efficiency.

Another large structure candidate that could implement fiber optic sensors is the superconducting accelerator. When designing a superconducting accelerator dipole magnet it is extremely important to understand the applied stress on the coil windings, because the superconducting capabilities are subsequently reduced under these conditions. These stresses are a result of: 1) the mechanical harnessing of the magnets which prevent movement during operation, 2) thermal stresses during cool-down, and 3) magnetic field dependent stresses. Currently, these stresses are calculated using finite element models and

are yet to be verified by an actual strain measurement during operation due to difficulty of obtaining strain measurements in magnetic fields. The Fabry-Perot strain sensor described in this dissertation has recently been demonstrated at -268°C on magnets used in superconducting accelerators. The sensors measured strain with 0.01 microstrain resolution in a liquid helium bath and a 13 Tesla magnetic field [4]. This strain information will allow verification of the finite element model and give feedback during operation to improve control and safety during the experiments.

Magnetic levitation (Maglev) trains are currently in operation in Japan and Germany. Pending the development of new materials, they are likely to become a cost effective alternative to air travel for distances of 100 to 600 miles. To attain speeds of 300 miles per hour and ensure safe operation at these speeds, monitoring the train system's guideways will necessitate the detection of mechanical and thermal strain, magnetic fields, and damage due to vibration or corrosion. The strain information could be used as an input to a control system to actively keep the guideway within proper tolerances, while the corrosion and damage detection measurements would help determine the need for guideway repairs and inspections. The Maglev trains, like the superconducting magnet, will provide a challenging environment for sensing systems due to high magnetic fields, corrosive deicing chemicals, and long distances between the sensors and the central control station.

Safety concerns in the mining industry have lead to many applications of optical fiber sensors including stress monitoring in roof bolts and wall supports that predict failure and sound warnings if critically loaded. Optical fibers greatly reduce the concerns of spark and explosion hazards, when compared to conventional electrical sensing systems. There is still some concern regarding the optical powers within the fibers because the powers are enough to ignite dust particles, but these dangers are more prominent in their electrical counterparts. Optical fibers can also be used to monitor air quality by detecting unsafe levels of mine gases such as methane.

The nuclear industry provides another challenging sensing opportunity for optical fiber sensors. High levels of radiation, extreme temperatures, and corrosive environments make fiber optics a likely choice for sensing essential parameters in the nuclear industry. Sapphire optical fibers are especially attractive for this application due to their high melting

temperatures (over 2000°C). Fiber sensors could provide a means of monitoring pressure and corrosion in fuel and waste storage facilities to insure proper containment.

In light of this significant body of research and need for highly sensitive, all-dielectric sensors, this dissertation describes several novel phase-modulated optical fiber sensors with possible applications in the aforementioned areas. Chapter 2 describes a Fabry-Perot strain gage, a sapphire fiber temperature sensor for applications up to and including 1700°C is presented in Chapter 3, a description of a microphone capable of withstanding 1000°C utilizing a Michelson interferometer with sub-Angstrom resolution is presented in Chapter 4, and a two-mode, elliptical-core fiber distributed strain sensor and vibration mode filter are presented in Chapter 5. For each sensing concept, a description and method of operation is given, followed by fabrication methods and experimental results. Finally, a summary is given and future directions of research are mentioned.

2. Fabry-Perot Strain Sensor

This chapter describes the design and operation of a fiber optic Fabry-Perot strain gage. The sensor is demonstrated on an F-15 at Wright Patterson Air Force Base and in a combustor at the Westinghouse Science and Technology Center. The strain sensor has been demonstrated at temperatures ranging from -200 to 900°C. The Fabry-Perot strain gage with a one centimeter gage length can be operated in differential mode with 0.01 microstrain resolution in real-time, and in an absolute mode with 0.5 nanometer resolution with a three second scan time.

The sensor description and theory of operation are given in Section 2.1, differential sensor demonstrations are given in Section 2.2, absolute strain sensing is described in Section 2.3, and Section 2.4 describes how four Fabry-Perot sensors have been embedded in a graphite/epoxy composite laminate and successfully demonstrated in an impact detection and location system.

2.1 SENSOR DESCRIPTION

Fiber optic Fabry-Perot (FP) sensors reported in the literature have been highly sensitive to temperature, mechanical vibration, acoustic waves, and magnetic fields [5]. Techniques to create the FP cavity have varied from the creation of Bragg gratings in or on the fiber [6] to the use of air-glass interfaces at the fiber ends as the reflectors [7]. A relatively new technique described by Lee and Taylor involves fabricating semireflective splices in a continuous length of fiber [8]. The remainder of this section describes an optical fiber extrinsic FP interferometer (EFPI) for measuring strain and microdisplacements.

A detailed drawing describing the construction of the extrinsic FP interferometer can be seen in Figure 1. A single mode fiber (λ_0 = 1300 nm), used as the input/output fiber, and a multimode fiber, used purely as a reflector, form an air gap that acts as a low-finesse FP cavity. The far end of the multimode fiber is shattered so the reflections from the far end do not add to the detector noise. The Fresnel reflection from the glass/air interface at the front of the air gap (reference reflection) and the reflection from the air/glass interface at the far end of the air gap (sensing reflection) interfere in the input/output fiber. Although

multiple reflections occur within the air gap, the effect of reflections subsequent to the ones mentioned above can be shown to be negligible. The two fibers are allowed to move in the silica tube and changes in the air gap length cause changes in the phase difference between the reference reflection and the sensing reflection. This changes the intensity of the light monitored at the output arm of a fused biconical tapered coupler.

The interference of the two-wave interferometer can be evaluated in terms of a plane-wave approximation. A coherent, approximately-plane wave detected at the output of the sensor can be represented in terms of its complex amplitude U_i (x, z, t) , given by

$$U_i (x, z, t) = A_i \exp (j\phi_i), \quad i = 1, 2, \tag{2.1}$$

where the variable A_i can be a function of the transverse coordinate x and the distance traveled, z, and the subscripts i =1, 2 stand for the reference and the sensing reflections, respectively. Assuming that the reference reflection coefficient $A_1 = A$, the sensing reflection coefficient A_2 can be approximated by the simplified relation [9]

$$A_2 = A\left[\frac{t\,a}{a + 2s \tan\left(\sin^{-1}(NA)\right)}\right], \tag{2.2}$$

where a is the fiber core radius, t is the transmission coefficient of the air-glass interface (≈ 0.98), s is the end separation and NA is the numerical aperture of the single-mode fiber, given by $NA = (n_1^2 - n_2^2)^{1/2}$. The terms n_1 and n_2 are the refractive indices of the core and the cladding, respectively. The observed intensity at the detector is a superposition of the two amplitudes and is given by

$$I_{det} = | U_1 + U_2 |^2 = A_1^2 + A_2^2 + 2 A_1 A_2 \cos (\phi_1 - \phi_2), \tag{2.3a}$$

which can be rewritten as

$$I_{det} = A^2\left[1 + \frac{2t\,a}{a + 2s \tan [\sin^{-1}(NA)]} \cos\left(\frac{4\pi s}{\lambda}\right) + \left(\frac{t\,a}{a + 2s \tan [\sin^{-1}(NA)]}\right)^2\right], \tag{2.3b}$$

where we have assumed that $\phi_1 = 0$ and $\phi_2 = 2s\ (2\pi/\lambda)$, and λ is the wavelength of operation in free space. The simplified loss relation (2) for the misalignment of two fibers is sufficient for understanding the drop in the output intensity of the sensor as a function of the gap displacement. For a strain sensor, it is useful to plot the detected intensity versus gap-separation s, as shown in Figure 2. The fringe contrast drops as the displacement increases; this is to be expected since the relative intensity of the sensing reflection starts dropping with respect to the reference reflection.

The extrinsic FP interferometer was tested as a displacement sensor by attaching one fiber to a stationary block and the second fiber to a micropositioner which produces a known displacement between the fiber ends. For comparison with the theoretical results, Figure 3 shows an oscilloscope trace of the continuously monitored output intensity of the sensor for s = 0 to s = 203 μm. The experimentally counted number of fringes for the displacement was 310.5 which corresponds to a displacement of 202 micrometers.

Most FP sensors described in the past have been useful in the measurement of quasi-static strain alone. That is, when the induced strain changes its polarity, the FP interferometers would not be able to detect this change if the switch in direction took place at a maximum or minimum of the transfer function curve. Methods for obtaining directional strain information using thin-film, or resistive gages have been demonstrated [10]. It can be shown that two signals 90° shifted in phase will resolve this issue and can be used with EFPI strain sensors to measure the relative direction of dynamically varying strain. A theoretical description of the sensor operation is presented and two different configurations to obtain a quadrature phase-shifted operation are described.

Figure 4 shows a typical sinusoidal variation of the output intensity with respect to changes in the phase difference between the reference and the sensing reflections. If the phase difference ϕ varies sinusoidally with time and the peak-to-peak variation is large enough to push the sensor out of its linear range, fringes are observed at the output of the detector as shown in the figure. The basic principle of operation of the detection scheme for a dynamic strain measurement system can now be described by considering two sinusoidal transfer functions out of phase by 90°. Assuming that the transfer function for the first detector (D_1) leads that of the second (D_2), we find that the output waveform for D_1 leads that of D_2

until time t_1. At time t_1, the phase ϕ changes direction (because of a change in direction of the strain) and the output waveforms switch their lead-lag properties. Notice the output from D_2 now leads that of D_1 until time t_2 when the strain changes direction again. Keeping track of the lead-lag phenomenon between the two detectors gives unambiguous information about the relative direction of the strain.

If only one detector were used, the switch in direction would not be detectable if the strain changed direction at a peak of the transfer function curve. With two signals out of phase by 90°, if the direction change occurs at one peak (of either D_1 or D_2), the other transfer function curve will provide information about the direction change.

Practical methods of obtaining two signals 90° out of phase with respect to one another are shown in Figures 5 (a) and (b). In Figure 5 (a), two single-mode fibers are inserted into one hollow silica tube and the gap-separations for the two fibers are adjusted actively by moving the fibers in and out of the tube until a 90° phase shift is achieved at the output. Note that two different sources are used in order to avoid interference effects between the two signals returning to the coupler if only one source was used to launch light into the single-mode fibers. It may, however, be possible to use a single source and using two different lengths of lead fibers for the two sensors such that the difference in the lengths is greater than the coherence length of the laser. Figure 5 (b) is a slight variation of the earlier scheme; here, two different silica tubes are used to adjust the quadrature phase-shift actively. Since the two tubes have external diameters on the order of a few hundred micrometers, the two sensors monitor almost the same environmental perturbations.

To test the validity of the quadrature phase-shifted sensors, the sensor was attached (using the scheme shown in Figure 5 (b) to a cantilever titanium beam with an epoxy. The fiber sensor was attached along the length of the beam and beam vibrations were monitored. A typical oscilloscope trace is shown in Figure 6. The figure clearly shows the shift in the lead/lag properties of the two signals as the relative direction of the strain in the beam changes from increasing to decreasing. Sensitivities of 5. 54 ° phase shift / microstrain-cm have been obtained.

2.2 DEMONSTRATION

The following two sections describe on-site demonstrations and results of the EFPI strain sensor.

2.2.1 WESTINGHOUSE SCIENCE AND TECHNOLOGY CENTER

The objective of this research program was to develop instrumentation methods to allow the in situ analysis of ceramic cross flow (CXF) filters. Information from such instrumentation is needed to determine how the filters perform during operation, how subsequent filter and combustor designs may be improved based on the knowledge of such performance, and how and where damage and degradation occur. These tests were performed using silica optical fibers modified to withstand the high temperature and harsh chemical environment of the combustor. A quadrature phase-shifted extrinsic Fabry-Perot intefrometric (QPS-EFPI) sensor was tested as a thermally-induced strain gage on a ceramic cross-flow (CXF) filter at Westinghouse Science and Technology Center, in Pittsburgh. CXF filters are used for hot gas clean-up of coal-fired power generation systems, such as pressurized fluidized-bed combustors and integrated gasifier-combined cycles. The ceramic cross flow filter, as mentioned in the introduction, is analogous to cross-flow heat exchangers, except gas is passed between channels instead of thermal energy (heat). Filter elements are constructed of a porous ceramic (alumina or silicon nitride) material. The filter element size of interest is approximately 30 cm high by 30 cm long by 10 cm wide. Particles are removed from the gas stream by direct interception, diffusion, and inertial impaction.

The ceramic filter consists of multiple layers of thin, flat, porous ceramic with grooves which form channels in each layer. Consecutive layers of ceramic are oriented such that the channels formed are perpendicular to each other. One of the sides of the filter element is sealed. Gas enters the filter through the openings of the channel on the two sides that are perpendicular to the sealed end, permeates the porous ceramic, and exits through the openings on the side that is parallel to the sealed end. The filter elements are periodically backflushed with a brief, high-pressure cleaning pulse of air or nitrogen to remove the particles that were deposited on the dirty side of the dividing walls.

At the beginning of the tests the filter was still warm (100° F) from the heating process it underwent the previous night. The electric heaters were turned on to provide a slow warming of the filter which is normally done to prevent thermal shock to the filter. Figure 7 is a plot of strain and temperature versus time from one of the QPS-EFPI sensors during the following stages: i) electric heater warm-up, ii) cool-air to the back plate to start torch, iii) cool air increase, iv) flame on, v) flame out, vi) flame on again and, finally, vi) closed bypass valve to induce rapid heating. Each of these stages is noticeable on the plot. At 420° C the torch was turned off and the filter vessel was allowed to cool. The sensor performed equally well during the cool-down cycle.

2.2.2 WRIGHT PATTERSON AIR FORCE BASE F-15

This section presents the results obtained from the static and dynamic loading of an F-15 mounted within a full-scale test frame for the purpose of fatigue testing at the Structures Test Facility, Wright Laboratory, Flight Dynamics Directorate, Structures Division, Wright-Patterson Air Force Base, Ohio. QPS-EFPI sensors attached to the wings of the airplane were loaded dynamically as well as in a static fashion and the results obtained from a software based fringe pattern decoding scheme are in excellent agreement with the colocated resistive foil strain gages.

The thrust toward fiber optic sensor-based smart structures and skins requires that highly stable, ruggedized sensors be available for testing in embedded or attached applications. While laboratory experiments have demonstrated the applicability and potential of using stable fiber optic sensors for in-flight monitoring systems, no results have been reported on sensors experiencing gravitational forces in flight simulation studies. An important consideration in choosing a specific sensor is the format in which the final output is available. While fiber optic sensors operated in the laboratory can be considered to be successful if output fringe patterns can be observed, practical operation can be deemed feasible only when an analog/digital output is available to the end-user without having to see the fringes. Thus, for this particular application, the use of fiber-based sensors and resistance-based strain gages should be transparent to the user.

The fiber sensor heads were attached with epoxy to the underside of the wing, approximately three feet from the root. Four conventional electrical strain gages were positioned around the fiber sensors. Two fiber sensor heads were built and assembled for use with one laser source. A single-longitudinal mode (SLM) laser diode operated at λ = 1300 nm launched light into a 2×2 fused biconical tapered (FBT) coupler. The two arms of the coupler were concatenated to one FBT coupler each and the sensor head was attached to one of the output arms of the couplers via one hundred meters of single mode fiber cable. The reflections from the two sensors were detected at the photodetectors and the outputs from the detectors were connected to an oscilloscope as well as to a data acquisition system that kept track of the interference pattern. The one hundred meter length of fiber carried data to the simulation instrumentation room where the data acquisition system was located.

The wing was loaded from zero to one hundred percent in twenty percent increments. The one hundred percent load is representative of an F-15 at 6,096 meters (20,000 feet) with a gross weight of 17,615 kilograms (38,800 pounds) performing a 7.0 g maneuver. A typical output plot of one of the fiber sensors for a 20 to 40 % loading sequence is shown in Figure 8. Using a computerized data acquisition system it was possible to deduce the strain on the wing. For this calculation, it was assumed that the attached sensor faithfully represents the strain experienced by the structure. That is, a perfect strain transfer from the wing to the fiber sensor was assumed. An elongation of 0.65 μm would then correspond to a complete fringe shift on the oscilloscope. Measuring the number of fringes as well as fractions of fringes, a plot of the strain versus time is shown in Figure 9. Corresponding plots from the three electrical strain gages matched the fiber sensor outputs. A very repetitive signal consistency was observed and data for other loading cycles was similarly obtained.

Data gathered during cyclic loading of the aircraft is instructional because the intent of the structural loading is to replicate an actual flight spectrum. A typical portion of the loading profile consists of several fluctuating load levels that represent different in-flight maneuvers and their associated g-forces. Using a data acquisition system strain levels corresponding to the cyclic loading were obtained. Figure 10 shows a comparison of the fiber sensor output and the electrical strain gage closest to the fiber sensor. The minimum detectable

phase shift was 0.0996 ° which corresponds to a minimum detectable strain of 0.01 μstrain for a gauge length of 19.03 mm with no measurable hysteresis. In comparison, the resolution obtainable from the electrical strain gages was ± 20 μstrain at any given instant due primarily to bridge supply noise.

2.3 ABSOLUTE STRAIN SENSING TECHNIQUES

This section describes a method for absolute measurement of displacement using an EFPI sensor. The sensors described previously are differential in nature and cannot give an absolute measure of displacement. To produce an absolute sensor, a wideband optical source must be used rather than a monochromatic laser diode source. By scanning the various wavelength components of the sensor output, an absolute measurement of the gap separation is obtained.

The output of the EFPI is described by

$$I = I_o \sin\left(\frac{4\pi \cdot L \cdot n}{\lambda_s} + \varphi_o\right), \tag{2.4}$$

where L is the distance between the two endfaces of the fibers, n is the refractive index of the material filling the gap (for air, n = 1), λ_s is the wavelength in vacuum of the ideal monochromatic source, and φ_o is some initial phase.

Let λ_s take on two different values, λ_1 and λ_2, where $\lambda_1 < \lambda_2$ and redefine the argument of the sinusoid to be

$$\varphi_{1,2} = \frac{4\pi \cdot L}{\lambda_{1,2}}, \tag{2.5}$$

then the phase difference becomes

$$\Delta\varphi = \varphi_1 - \varphi_2 = \frac{4\pi \cdot L \cdot \lambda_1 \cdot \lambda_2}{\lambda_2 - \lambda_1}. \tag{2.6}$$

φ_o is assumed to be a constant resulting from the initial gap separation. Rewriting Equation

(2.6) gives

$$L = \frac{\Delta\varphi \cdot \Delta\lambda}{4\pi \cdot \lambda_1 \cdot \lambda_2}, \tag{2.7}$$

where $\Delta\lambda$ is the difference of the two wavelengths to be scanned. By scanning the phase difference accumulated between λ_1 and λ_2, Equation (2.7) can be used to compute the corresponding gap length.

A white light source was used to provide the wideband excitation necessary to operate the sensor in an absolute configuration. An EFPI was attached to a translation stage to provide accurate displacements and the sensor output was monitored on an Ando AQ 6103C Optical Spectrum Analyzer. The EFPI leads were constructed from 1300 nm circular core fiber with a cutoff wavelength of approximately 1100 nm for single mode operation. A representative output scan, as well as the theoretical prediction, is provided in Figure 11.

From Equation (2.4), there are three parameters that must be measured to compute the gap L, these parameters are the two wavelengths of interest and the associated phase between them. Two methods were used to compute the gap separation, 1) the constant phase method - λ_1 and λ_2 were found for $\Delta\varphi = 4\pi$, and 2) the constant wavelength method - $\Delta\varphi$ was found between λ_1 = 1100 nm and λ_2 = 1300 nm. The results can be seen in Figure 12, the dotted line indicates the measured gap displacements produced using the translation stage. The accumulated error is due to inaccuracies in reading actual displacements from the micrometer.

This method of using the scanned wavelength response of the EFPI is limited to static measurements because of the three second scan speed of the optical spectrum analyzer. Finally, the Ando AQ 6103C Optical Spectrum Analyzer has a resolution of 0.1 nanometers for wavelength measurements, which corresponds to an absolute gap measurement resolution of 5 nm.

2.4 IMPACT DETECTION AND LOCATION SYSTEM

The detection of ultrasonic frequency acoustic stress waves in materials has important applications in nondestructive evaluation (NDE): the quantitative determination of microstructural properties, the inspection of materials for quality control, and the in-situ analysis of materials which may include the measurement of acoustic emission (AE) events and the detection of impacts. Many techniques have been employed to detect acoustic waves. Methods using piezoelectric transducers made of quartz, lithium niobate or lead zirconium titanate (PZT) are quite common. In recent years, fiber optic interferometric sensors (FOIS) have emerged as viable alternatives to piezoelectrics as effective means of detecting and quantifying acoustic fields. FOIS have been shown to possess the high sensitivity required to respond to the Angstrom particle displacement amplitudes associated with acoustic waves, the wide operating temperature range (-200°C to 950° C) afforded by the material characteristics of optical fibers, and a wideband frequency response limited in many cases by detection electronics alone. Most FOIS rely on either 1) the longitudinal deformation of a sensor fiber caused either directly by axial strain, or indirectly via the Poisson effect through lateral pressure on the fiber, or 2) the photo-elastic effect which results in refractive index changes in the core and cladding materials of the fiber. These effects can cause changes in the optical propagation constants or optical path lengths in the interferometer, or both, resulting in a differential phase shift which may be observed as a variation of the output signal intensity [11 – 16].

In some practical interferometric configurations, a long segment of the fiber needs to be exposed to the acoustic field in order for the sensor to be sensitive to sub-Angstrom acoustic amplitudes [13]. A long fiber sensing length, however, will often increase the susceptibility of the interferometer to phase noise caused by vibration and temperature variation. Moreover, such conventional interferometers which rely on long integrating sensing segments are likely to encounter problems of fading and drifting [17].

The sensor system described here consists of multiple in-line extrinsic Fabry-Perot interferometers (EFPI), each having an external reflecting surface placed close to the end of a single-mode input/output fiber. The sensor has a gage length that can be varied during fabrication from several microns to several millimeters, and shows an increase in

temperature stability as well as an improved immunity to phase-modulated noise over previous designs. For example, intrinsic Fabry-Perot interferometers, used in the past to detect ultrasonic waves in and on materials [15], have suffered from complicated fabrication procedures, polarization-induced signal fading, susceptibility to extraneous perturbations, and demands for long coherence length sources.

Several methods of detecting and locating acoustic sources using conventional piezoelectric transducers have been considered. Tobias described a method of locating an acoustic source on a flat plate using three sensors [18]. Later, Asty expanded on Tobias' work by generalizing the theory to calculate acoustic source location on a sphere, again using three sensors. This theory could be applied to the case of a flat plate by letting the radius of the sphere approach infinity [19]. The methods suggested by Tobias and Asty still exhibit some ambiguity in source location by using only three sensors. Asty suggested the possibility of using four sensors to allow unambiguous location calculations, but did not elaborate on a method to accomplish this task. Later, acoustic source location using two pairs of sensors forming an exact square was described by Bobreto et al. [20]. Using this method, complex families of geometrical curves are used to determine the AE source location, thus not allowing real-time source location calculations.

Spillman and Fuhr were the first, to our knowledge, to use optical fiber sensors to detect and locate impacts [21]. They used two perpendicularly-oriented, distributed and integrating-effect optical fiber sensors attached to the surface and near two edges of a rectangular composite panel, and detected two arrival times for the acoustic waves generated by the impact.

An impact detection and location system utilizing four EFPI acoustic sensors embedded inside a ten-ply 3501-6 resin/AS4 graphite fiber composite laminate was constructed according to the three-dimensional geometry shown in Figure 13. As indicated, the sensors were embedded between adjacent plies having parallel graphite fiber orientation, with the long axis of each fiber and sensor head parallel to the graphite fiber direction of the plies. This minimizes the size of the local resin rich region which typically surrounds such embedded elements. Short lengths of high temperature polymer tubing were slipped over the fibers to extend several millimeters into the edges of the laminae prior to cure and

protect the first several centimeters of each fiber from possible damage where it exited the laminate.

The cured laminate containing the six EFPI sensors was backed with a wooded panel and supported vertically as shown in Figure 14. Each pair of EFPI sensors was interrogated using a separate support optics and electronics system; the figure shows two pairs, or four individual sensors, addressed at once, as required by the impact location calculation algorithm described below. The three oscilloscopes are arranged to determine the differences in the times of arrival of signals from sensors 1 and 2, 3 and 4, and 1 and 3. From this data, impact location may be uniquely determined.

The panel was impacted by both throwing and shooting 0.22-gage pellets from distances ranging from 10 cm to 5 meters, and at angles between on-axis and approximately 45° off-axis. Impacts generated by shooting the projectiles locally damaged the laminate in some cases. It was observed that for impacts as close as 1 cm from the location of the embedded sensor heads, local damage to the laminate did not result in the subsequent non-functioning of the sensors.

The geometry of a panel impact experiment indicating the coordinates of the sensors embedded in the panel are shown in Figure 13 (a). When a projectile is incident upon the panel, acoustic waves (surface and bulk) are excited in the composite material. The four sensors embedded in the panel are used to determine the time at which the local superposition of these acoustic waves reaches the sensors. In this section, the approximate location of an impact is derived in general from these four measured arrival times.

From Figure 14 we have

$$\Delta t_i' \, v_i = r_i \ , \ (i = 1, \cdots , 4) \ . \tag{2.8}$$

where v_i is the propagation speed of the acoustic wave along the direction from Q to sensor i, $\Delta t_i'$ is the propagation time of the acoustic wave from Q to the sensor, and r_i is the distance between point Q and the sensor. Generally, the information obtained from these

multiple sensors is a set of relative time delays between the arrival times of the acoustic waves at different sensor locations rather than an absolute measure of the propagation time of the acoustic wave from the impact site to the sensor locations. That is

$$\Delta t_i = \Delta t_i' + \Delta t_o, \quad (i = 1, \cdots, 4). \tag{2.9}$$

Assuming the material is isotropic , $v_i = v$ $(i = 1, \cdots, 4)$, and substituting Equation (2.9) into Equation (2.8), we have

$$(\Delta t_1 - \Delta t_o)\, v = r_1 , \tag{2.10a}$$

$$(\Delta t_2 - \Delta t_o)\, v = r_2 , \tag{2.10b}$$

$$(\Delta t_3 - \Delta t_o)\, v = r_3 , \tag{2.10c}$$

and

$$(\Delta t_4 - \Delta t_o)\, v = r_4 . \tag{2.10d}$$

From Equation (2.10 a) we have

$$\Delta t_o = \Delta t_1 - \frac{r_1}{v} . \tag{2.11}$$

Substituting Equation (2.11) into Equations (2.10a), (2.10c) and (2.10d), we obtain

$$(\Delta t_2 - \Delta t_1)\, v = r_2 - r_1 \tag{2.12a}$$

$$(\Delta t_3 - \Delta t_1)\, v = r_3 - r_1 \tag{2.12b}$$

$$(\Delta t_4 - \Delta t_1)\, v = r_4 - r_1 \tag{2.12c}$$

From Equations (2.13) it is noted that, if the propagation speed of the acoustic waves in the material is exactly known, three sensors should be enough to allow determination of the impact location. The advantages of instead using four sensors are several. First, the use of four sensors makes this technique applicable to isotropic materials for which the acoustic wave speed may be not known. Secondly, the use of four sensors reduces the possible inaccuracies caused by measurement errors of the acoustic wave velocity. To solve for the impact location using four sensors, Equations (2.12) first can be rewitten as

$$(1 - A)\, r_1 = r_2 - A\, r_3 \tag{2.13a}$$

$$(1 - B)\, r_1 = r_2 - B\, r_4 \tag{2.13b}$$

where

$$A = \frac{(\Delta t_2 - \Delta t_1)}{(\Delta t_3 - \Delta t_1)} \tag{2.14a}$$

$$B = \frac{(\Delta t_2 - \Delta t_1)}{(\Delta t_4 - \Delta t_1)} \tag{2.14b}$$

Since Equations (2.13) is a nonlinear equation group, a numerical solution method is necessary to obtain the coordinates (x,y) of the impact location and Newton's method may be used.

Any equation group which contains two unkowns, x and y, can be written as

$$u(x, y) = 0 \tag{2.15a}$$

$$v(x, y) = 0. \tag{2.15b}$$

If $P_o\ (x_o, y_o)$ is tried as an initial solution and

$$\left| \begin{array}{cc} \frac{\partial u}{\partial x} & \frac{\partial u}{\partial y} \\ \frac{\partial v}{\partial x} & \frac{\partial v}{\partial y} \end{array} \right|_{P_o} \neq 0, \tag{2.16}$$

then the possible solution of Equations (2.15a,b) can be expressed as

$$x_{n+1} = x_n + \frac{1}{J_n} \left| \begin{array}{cc} \frac{\partial u}{\partial y} & u \\ \frac{\partial v}{\partial y} & v \end{array} \right|_{P_n}, \tag{2.17a}$$

$$y_{n+1} = x_n + \frac{1}{J_n} \left| \begin{array}{cc} u & \frac{\partial u}{\partial x} \\ v & \frac{\partial v}{\partial x} \end{array} \right|_{P_n}, \tag{2.17b}$$

where

$$J_n = \left| \begin{array}{cc} \frac{\partial u}{\partial x} & \frac{\partial u}{\partial y} \\ \frac{\partial v}{\partial x} & \frac{\partial v}{\partial y} \end{array} \right|_{P_n}, \tag{2.18}$$

When the difference between P_{n+1} and P_n in Equation (2.17) is considered to be small enough, the calculation process for determining a solution is completed.

For each impact of the specimen, acoustic wave arrival time signatures and relative time delays were obtained for each of three pairs of embedded EFPI sensors. Figures 15, 16, and 17 show impact-generated acoustic wave signatures detected by the four EFPI sensors. Since no attempt was made to control the position of the quadrature point of the sensors on their respective sinusoidal transfer functions during the tests, the initial slopes of the acoustic events are arbitrary. The arrival time of each acoustic wave was identified as the first received data point above the maximum value of the noise signal preceding impact. This simple rule allowed the determination of the Δt_i terms in Equation (2.12), and the solution of the algorithm for the location of the impact site on the surface of the panel. Typical results for the calculated and measured coordinates of impact locations using this procedure are the following (all dimensions are in millimeters), Trial 1: calculated, $x = 31.3$, $y = 121.5$; measured, $x = 28$, $y = 124$, Trial 2: calculated, $x = 76$, $y = 149$; measured, $x = 70$, $y = 148$. It is noted that the complicated acoustic wave transmission properties of the composite laminate may cause internal scattering, guided mode and interface wave propagation effects, mode conversion, and symmetric and antisymmetric plate mode behavior, all of which may cause errors in the determination of effective acoustic wave velocities and times of arrival.

In summary, an array of four wideband surface acoustic wave sensors employing an extrinsic optical fiber Fabry-Perot interferometer design have been used to determine the location of projectile impacts on the composite panel in which they were embedded. The extrinsic nature of the sensor head element allows the sensor to be tuned for maximum sensitivity and passively stabilized for continuous operation. Low frequency impact-generated stress waves in polymer-based composites have been detected using this sensor. The sensor is simple to construct since it does not involve the deposition of metallic films, and its extrinsic nature allows the use of relatively inexpensive low coherence length laser sources. An experimental resolution of impact location to within 5 millimeters has been obtained.

3. Sapphire Interferometer

This chapter describes the use of a short-length, multimode sapphire rod as an extension to a Michelson configuration, but operated as a low-finesse Fabry-Perot cavity. The device is demonstrated as an interferometric sensor, where the interference between the reflections from two sapphire-air interfaces is observed for microdisplacements of the target sapphire. The sensor is configured to measure temperature and is successfully tested up to 1700°C.

The sapphire fiber sensor description is given in Section 3.1, and Section 3.2 describes how the sensor can be used to measure high temperatures.

3.1 SENSOR DESCRIPTION

Existing silica-based optical fibers are currently being used in a wide variety of sensing applications where the operating temperatures do not exceed 500°C. In a number of applications where higher temperatures are encountered and harsh environments are unavoidable, it is imperative that both optical waveguides and optical waveguide coatings fabricated from materials other than silica be considered. The development of advanced high temperature materials, and the increasing demand for the control of advanced high temperature combustion and industrial processes, require sensor instrumentation which can perform reliably in high temperature environments. During the past ten years, optical fiber instrumentation has been applied to a wide variety of materials and process instrumentation situations. Optical fiber sensor methods offer the advantages of multiplexed and multimeasurand operation, combined with the avoidance of electromagnetic interference effects and ground loop networking problems [31]. Sapphire (Al_2O_3) is one such candidate material that possesses reasonable optical propagation properties in both fiber and rod form, and can potentially perform without significant degradation under harsh conditions, including temperatures up to 2000°C.

Conventional communication grade optical fiber waveguides are made of silica, typically 125 to 140 microns in diameter, and are coated with acrylate polymers which perform well over the full range of extended ambient environmental temperatures, but which degrade at temperatures much above 150°C. Above those temperatures, higher temperature polymer

coatings are required. These are typically polyimide-based, and allow operation to the 400°C to 500°C range. Applications at still higher temperatures require the use of metal or ceramic-coated silica fibers. Gold-coated silica fibers, for example, perform well up to the temperatures where 1) the dopants in conventional silica fibers begin to migrate and thus adversely affect both waveguide guidance and attenuation properties, and 2) the doped silica begins to soften [32]. These temperatures are approximately 800-900°C.

At still higher temperatures, the options are limited. For selected measurements, platinum gauges are alternatives, although typically they have the disadvantages of electromagnetic interference, ground loop instrumentation difficulties, and single-measurand capability. Sapphire-fiber/rod-based interferometric sensors offer an alternative technology which avoids some of these intrinsic disadvantages while offering competitive sensitivity and resolution performance.

In experiments reported thus far, unclad sapphire rods have been used only in intensity-based sensors because of their large numerical apertures. Numerical apertures of silica-clad sapphire rods have been found to vary from 0.55 to 0.83 but their available core diameters are not sufficiently small to allow single-mode operation at optical wavelengths. Since phase-modulated interferometric sensors which require single-mode optical fiber waveguides are many times more sensitive than their multimode counterparts, methods of fabricating single-mode sapphire fibers are being investigated.

Optical quality sapphire rods can be grown as single crystals using several standard methods [33]. Outer diameters of typical commercially available sapphire rod waveguides vary between fifty and several hundred microns, with lengths up to several meters. In contrast to conventional silica based optical fibers, these rods do not have outer cladding regions of lower refractive index than the core material. Such cladding layers normally are required to effectively confine the propagating optical power within the waveguide, and to thus limit both optical attenuation and cross-coupling which may occur between adjacent waveguides, as well as into the surrounding environment.

Such sapphire rods also do not have external coating layers designed to protect the sapphire from the surrounding environment. These types of protective coatings have been shown to

be of special importance in applications involving exposure to harsh chemical contaminants at high temperatures [34]. Coating layer materials are also important for the transfer of strain and temperature from the material to be evaluated to the sapphire fiber sensor element. For high temperature measurement applications, the coefficient of thermal expansion mismatch between the sapphire fiber element and the host material may lead to a loss of interfacial contact, and a resulting discontinuity in heat flow and strain at the boundary. Alternatives for the possible solution of this problem, including multi-layer geometries of different coating materials, have been suggested [35].

Since single mode sapphire optical fibers are currently not available, an interferometric sensor has been implemented here with bulk sapphire rods. Figure 18 shows the geometry for a particular implementation. Here a five millimeter diameter sapphire rod was used as a bulk optical component that acts as a conduit to an external reflector. A graded index lens couples light from an input single mode silica optical fiber into the rod and produces a collimated optical beam with a waist size on the order of one millimeter. Thus, the optical beams which propagate down the length of the sapphire rod and back approximately at the center of the rod do not substantially interact with the outer surface of the rod and hence the external physical environment. For ease of assembly, the lens, the input fiber and the rod are mounted in a conventional optical fiber connector ferrule and for durability the components have been attached together using low temperature epoxy-based adhesives. The temperature limitations of this design are imposed by the low temperature epoxy as well as by the higher temperatures at which the dopants in the lens migrate, thus altering the index of refraction profile of the lens and degrading its collimation properties. As long as the ferrule and its associated optical components are protected from the hot zone by some method of active cooling, this design could be used in very high temperature environments.

The interferometric geometry shown in Figure 18 has been used to measure the displacement of a metallic surface at high temperature in an oven. As shown in Figure 18, the space between the end of the sapphire rod and the metallic surface forms a low finesse Fabry-Perot cavity, the length of which changes as the reflector surface is displaced. The back reflected interference signal travels along the sapphire rod, back through the lens and into the single mode fiber through which it is coupled to the in-line fused biconical tapered coupler to an optical detector. The output of the detector is proportional to the intensity of

the interference pattern generated by the Fabry-Perot etalon. Standard techniques for the determination of displacement, either by counting successive interference fringes for relatively large displacements, or by monitoring intensity modulation within one optical fringe for relatively small displacements, may then be used to determine displacement as a function of time [36].

Figure 19 shows surface displacements measured at room temperature. Here the interferometer reflector was displaced mechanically by means of a micropositioner. The top trace shows a number of fringes corresponding to a 0.1 millimeter total displacement; the bottom trace is an expanded view of part of the multifringe signal which clearly shows that the effect being measured is a sinusoidal interference effect.

The previous design is limited in that the air gap may be easily corrupted with airborne particulates. To extend the sensor applicability to environments that may contain these contaminants, an enclosed feature was added as shown in Figure 20. By enclosing the cavity, this sensor becomes amenable for embedding within composites (metal matrix, carbon fiber, etc.) where there is a possibility of material flowing and obscuring the etalon. This sensor has a well defined gage length which allows for determination of temperature or strain experienced by a structure.

Figure 21 is an example of the response to strain. Here the above sensor configuration was attached to a translation stage to apply strain to the system. The usual methods to determine the strain may then be applied from the sensor output.

3.2 TEMPERATURE SENSING AT 1700°C

A temperature sensor was constructed as shown in Figure 22. To reduce the temperature at the GRIN lens interface a 110 mm-long sapphire rod with a diameter of 1.51 mm (manufactured by Saphikon, Inc.) was used to construct a sapphire EFPI to measure temperature up to 1740°C. In the arrangement shown in Figure 22, there are two kinds of adhesive. One is the ceramic adhesive (manufactured by Cotronics Corp.) which can sustain high temperature up to 1648°C. The other adhesive is a standard low temperature,

two-part epoxy with an approximate maximum operation temperature of 70°C. With this long rod, the temperature at the GRIN lens was held to below 50°C and thus acceptable for the long term performance of the low temperature epoxy used to align the optical components.

In the experiment, the Fabry-Perot cavity inside the hollow core sapphire tube was heated using an oxygen and propane torch flame, while the tip of a conventional thermocouple was placed directly on the cavity touching the sapphire tube to monitor the temperature. The length of the Fabry-Perot cavity was about 314 microns. This sensor was heated above 1500°C several times. The highest temperature measured was about 1740°C.

To calculate the number of fringes (m) generated by introducing a ΔT temperature difference in the Fabry-Perot cavity, we use the extrinsic Fabry-Perot interferometer formula

$$m = \frac{2\,\Delta(Ln)}{\lambda}, \tag{3.1}$$

where $\Delta(Ln)$ is the change in optical length of the cavity after ΔT is introduced and λ is the wavelength of the laser source (1300 nm).

The change in optical length of the cavity is described by

$$\Delta(Ln) = n\Delta L + L\Delta n, \tag{3.2}$$

where L is the cavity length, and for air, n =1, and $\Delta n = 1.0 \times 10^{-6}$ /°C.

Here,

$$\Delta L = \alpha\, L\, \Delta T, \tag{3.3}$$

where α is the linear c-axis coefficient of thermal expansion of sapphire (5.3×10^{-6}/°C) and L is the air gap (Fabry-Perot cavity) length (314 microns) at room temperature.

Substituting into Equation (3.3), the number fringes due to a change in cavity length is calculated to be

$$m_{\Delta L} = \frac{2\,\alpha\,L\,\Delta T}{\lambda} = \frac{2 \text{ x } 5.3\text{x}10^{-6}/^{\circ}\text{C x } 314\ \mu\text{m x } \Delta T}{1300\ \text{nm}} \approx 2.6 \text{ x } \frac{\Delta T}{1000\ ^{\circ}\text{C}}. \qquad (3.4)$$

The number of fringes due to index of refraction changes is $m_{\Delta n} \approx -0.5/1000°C$. The corresponding theoretical values (neglecting refractive-index changes in the air) for the high temperature measurements are compared to the experimentally obtained number of fringes in Figure 23.

The laser was supplied with a drive current below threshold, to operate effectively as an LED, to shorten the coherence length. The short coherence length of the LED eliminates the output signal contribution from the interference between the two endfaces of the long sapphire rod. Therefore, only the small air gap EFPI signal contributes to the output.

Figure 23 shows a discrepancy between the theoretical prediction and the experimental measurement, especially for higher temperatures. This discrepancy may arise from the fact that the sapphire hollow tube experiences a higher temperature than the sapphire rods inside. Therefore, the real expansion of the air gap is greater than the theoretical assumption. This may be also the reason that the higher the temperature, the larger the discrepancy between theoretical and experimental data.

4. Temperature Insensitive Michelson Interferometer

This chapter describes the design and operation of a fiber optic temperature insensitive Michelson interferometer (TIMI) displacement sensor. The sensor is capable of measuring displacements with sub-Angstrom resolution with no measurable signal drift due to temperature changes. The TIMI is demonstrated in a diaphragm-based pressure transducer configuration.

A description of the temperature insensitive Michelson interferometer is given in Section 4.1, and high temperature/high acoustic pressure transducer incorporating a TIMI is described and demonstrated in Section 4.2.

4.1 SENSOR DESCRIPTION

Single mode fiber optic interferometric sensors (FOIS) have been shown to possess high sensitivities for various applications. Measurement of real time phase-shifts has been demonstrated in acoustic, temperature, magnetic and strain sensors [1,37-39]. In the FOIS reported so far, the reference and the sensing arms usually are physically at different locations and hence a minuscule change in temperature in the reference arm may affect the phase difference detected at the output of the sensor. This thermally-induced signal drift may lead to a misinterpretation of the observed change in phase due to temperature changes being attributed to the external perturbation to be measured.

It is essential to maintain the FOIS continuously at the quadrature point of operation. To achieve such performance, Jackson et al. have used a piezoelectrically stretched fiber and active feedback in the reference arm to solve this problem [40]. Similarly, an integrated optic microdisplacement sensor, which uses a Y junction and a polarization preserving fiber, has been reported [41]. Passive stabilization schemes using 3×3 couplers and active optical schemes have also been demonstrated [42,43].

The thrust of past research has been in the area of thermal compensation, while the technique presented here involves reducing the thermal dependence. The construction of the temperature insensitive Michelson interferometer (TIMI) sensor can be described as

follows:

1) A fused biconical tapered coupler was constructed from a 4/125 μm single mode fiber with numerical aperture 0.1.
2) The two output arms of the coupler were cleaved immediately after the coupling length.
3) The coupler was attached to Invar strips with epoxy and polished until two cores, very close to each other, could be observed.
4) Aluminum was selectively deposited at the end of one of the cores.

The core with the mirrored end was used as the reference arm and the uncoated core served the purpose of the sensing arm. A schematic of the sensor is shown in Figure 24.

In order to test the stability of this sensing scheme, two Michelson configurations were placed side-by-side and their performance was evaluated in terms of temperature drifts. The experimental set-up, shown in Figure 25, consists of the miniaturized FOIS and a standard, simple, homodyne Michelson interferometer placed in front of a vibrating mirror attached to a vibrating diaphragm. One would normally expect a $\pi/2$ phase shift in the detected signal for a one meter length homodyne Michelson arrangement for a temperature gradient of 10 millidegrees between the arms [1]. The miniaturized FOIS has both arms very close to each other which makes it very difficult to predict the expected phase shifts due to a given temperature gradient. One way of comparing the two schemes is to continuously monitor the outputs and observe the drifts due to small changes in the environmental conditions. Figures 26 (a) - 26 (c) show the oscilloscope waveforms of the two sensors at millisecond intervals for a single fringe, and Figures 27 (a) and 27 (b) depict the same for multiple fringes. Signal fading is observed in the standard Michelson due to temperature induced shifts in the quadrature point of operation. In comparison, no measurable change in quadrature point was observed for the TIMI waveforms over more than three hours.

We have obtained signal-to-noise ratios (SNR) of 65 dB with a minimum detectable phase shift of 0.0017 rad which corresponds to a minimum detectable displacement of 0.03 nm. The fringe contrast is determined by the relative intensities of the reference and the sensing signals. The relative amplitudes of the interfering signals depend intrinsically on the

reflectivity of the sensing surface and the distance of the sensor head from the reflective surface. In this sense, it is useful to know the optical properties of the microdisplaced surface prior to the construction of the sensor. In practice, it was found that reflectivites of 40 % at the reference reflection result in high fringe contrast for metallic sensing surfaces. Shot noise limited detectors should allow SNRs in the 70-80 dB range, as predicted theoretically [1].

For the measurement of microdisplacements, the stability of the sensor placement itself plays an important role in the observed signals. One would expect the sensor sensitivity to be highly dependent on the vertical displacement of the probe from the surface as well as on the angular orientation. To determine this dependence, the change in the output voltage obtained from the detector as the distance x and the angle θ were varied was experimentally measured. A schematic of the experiment is shown in Figure 28.

Figures 29 and 30 show the results of this analysis. Both figures show the critical dependence of the sensor performance on the orientation of the sensor. An angular misalignment of 0.05° or a vertical displacement of 30 μm is shown to result in a 3 dB drop in the detected signal. This result implies that the probe can be used in applications where the sensor can be brought very close to the surface which experiences the microdisplacements.

The TIMI is virtually insensitive to temperature drifts when compared to the simple, homodyne, Michelson interferometer. It can be used for the measurement of microdisplacements in high temperature ($T \geq 700$ °C with specialized fibers) environments and bandwidth limited by the detection electronics only. The TIMI can be used for the measurement of any external perturbation which manifests itself as a microdisplacement. Standard Michelson or Mach-Zehnder configurations provide for piezoelectric coils to be introduced for stabilization or electronic circuitry to be combined for phase-error feedbacks. The proximity of the two arms in the miniaturized version makes it difficult to introduce such stabilization schemes. The inherent stability of the sensor, however, eliminates the need for feedback circuitry. The sensor allows high-sensitivity, low-frequency measurements which simply are not available with conventional interferometric techniques.

2.2 PRESSURE TRANSDUCER TESTED AT NASA LANGLEY

Direct acoustic measurements in hostile environments such as SCRAM jets, turbojets, and rocket engines require instrumentation that can withstand high heat flux and high vibrations. These measurements are needed for several applications including computational fluid dynamics code validation, structural acoustics tests, and jet noise abatement tests [44].

This section describes an experimental fiber optic interferometric-based microphone developed jointly with NASA Langley [45]. The microphone is composed of a temperature insensitive Michelson interferometer (TIMI) and a reflective plate diaphragm. The interferometer monitors the diaphragm plate deflections, which is directly related to the acoustic pressure difference on each side of the diaphragm. The transducer is water cooled to provide thermal protection for the TIMI and to stabilize the mechanical properties of the diaphragm.

The diaphragm design was such that the maximum deflection observed would be within the linear range of the TIMI. This linear range is approximately 50 nanometers. The pressure-deflection relationship for a circular diaphragm constructed with a homogeneous and isotropic material of flat and uniform thickness, fixed edges and loaded with a uniform pressure can be described by

$$y = \frac{3(1-\nu^2)P}{16Et^3}(a^2 - r^2)^2 \quad , \tag{4.1}$$

where y is the deflection at any radial distance, P is the pressure, t the thickness, "a" is the radius of the diaphragm, r is the radial distance from the center, E and ν are the Young's modulus and Poisson's ratio of the diaphragm material, respectively [46]. Other restrictions of Equation (4.1) include the plate thickness should not be more than 20% of the diameter, the maximum deflection should not be more than 30% of the thickness of the plate and the median plane of the diaphragm should not experience any tensile forces. The

maximum deflection occurs at the center of the diaphragm were r=o, which reduces Equation (4.1) to

$$y_o = \frac{3(1-\nu^2)Pa^4}{16Et^3} \quad . \tag{4.2}$$

Both the laminar and the turbulent volume flow rate sensors will use a fiber optic sensor to measure the deflection of a diaphragm. The diaphragm was designed to operate in the expected pressure range, and with the aforementioned restrictions in mind still remain within the linear range of the fiber optic sensor.

The natural frequency is described by

$$f_n = 9.22 \frac{t}{a^2} \left[\frac{E}{w(1-\nu^2)} \right]^{\frac{1}{2}} \quad , \tag{4.3}$$

where w is the specific weight of the material. Equation (4.3) does not account for damping due to edge-mounting adhesive. It is important to design the diaphragm with a natural frequency above the desired working range to insure linear operation.

In light of Equations (4.2) and (4.3), a copper diaphragm was fabricated from 0.05 mm foil with a 1.25 mm diameter. This diaphragm will exhibit a maximum center deflection of 39 nm for a pressure differential of 1.4 kP, which is within the linear range of operation for the TIMI. The natural frequency of the diaphragm is calculated to be 100 kHz, which is well above the desired working range of several kHz for structural acoustic load testing.

The high thermal conductivity and low modulus of elasticity of copper is ideal for the diaphragm construction. The low modulus of elasticity of copper allows the use of a diaphragm that is thicker than conventional diaphragm-based microphones, while maintaining usable natural frequency and suitable deflection for use with the TIMI. Thicker and smaller diameter diaphragms exhibit more symmetrical temperature distributions, which along with the high thermal conductivity of copper allows the diaphragm to be held at a constant temperature throughout the desired temperature range.

The TIMI-based microphone, as shown in Figure 31, was compared to the conventional piezoelectric transducers (PZT) currently used at the thermal acoustic fatigue apparatus (TAFA) facility at NASA Langley. Figure 32 (a) shows the two oscilloscope traces from the TIMI-based and PZT microphones with a 1 kHz sine wave input at 1600°F. Note the electromagnetic interference (EMI) present in the PZT signal caused by the TAFA facility electromechanical switching. The fiber optic TIMI is immune to EMI, as are all fiber-based sensors. Figure 32 (b) shows fast Fourier transforms (FFT) of the time varying voltage outputs recorded form Figure 32 (a). The TIMI-based microphone exhibits a 10 dB better dynamic range over the PZT microphone. The 1 kHz input for this test was one of the most sensitive frequencies for the PZT, which does not have a flat response to frequency due to its geometry.

A room temperature test was conducted on a similar TIMI-based microphone to determine linearity with acoustical inputs form 130 to 160 dB. Figure 33 is a plot of the TIMI output in volts versus the acoustic input level in dB. The TIMI-based microphone is linear over the entire range of interest.

5. Two-Mode Fiber Sensing

This chapter describes the operation of two-mode fiber sensors and presents the design and experimental results of several sensing schemes utilizing elliptical- and circular-core, two-mode fiber. Techniques for desensitizing the lead-in and lead-out fibers are successfully implemented using a single-mode, elliptical-core fiber as the lead-in fiber and an offset circular-core single mode fiber as the lead-out fiber. Detection techniques for two-mode fiber sensors are reviewed and experimental results from a novel fringe-counting method to unambiguously detect the amplitude and direction of dynamic strain are reported. Also presented are the theory of operation and experimental results of spatially-weighted optical fiber sensors that enhance the detection of specific vibration modes from one dimensional beams placed in a clamped–free configuration. The sensitivity of the sensors is varied along the length of the fiber using two methods: 1) tapering two-mode, circular-core optical fibers, and 2) photoinduced refractive-index changes (gratings) in two-mode, elliptical-core optical fibers. Selective vibration mode suppression on the order of 15 dB has been obtained using the weighted sensors. Finally, future applications for distributed sensors are discussed.

The two-mode sensor description and theory of operation are given in Section 5.1, insensitive lead results are given in Section 5.2, demodulation techniques are described and tested in Section 5.3, and finally Section 5.4 describes the design and successful demonstration of spatially-weighted optical fiber sensors.

5.1 SENSOR OPERATION

Two- and few-mode, circular-core fibers have been used in the past as sensors for measurement of pressure, strain and vibrations [47, 48]. Two- and three-lobe far-field intensity distributions are obtained at the output by exciting appropriate modes within an optical fiber. The standard method of analysis involves a measurement of the exchange of optical power between these lobes in order to determine the nature of the external perturbation. The major obstacles in practical implementation of such sensing systems that use circular-core fibers have been the strict input conditions required to launch specific

modes and the instability of the cross-sectional intensity distribution of the second order modes [49].

Elliptical core (e-core) fibers guide only two of the four second order non-degenerate modes with a well defined intensity distribution. This property has been utilized in the demonstration of stable strain gages and other few-mode devices such as intermodal couplers, modal filters, and acousto-optic single side-band frequency shifters [50 - 52]. Although laboratory demonstrations of two-mode, e-core fiber interferometric sensors have been shown to be feasible, practical implementation requires special launching and detection techniques.

The increasing focus on attached or embedded fiber sensors in smart structure applications demands that ruggedized designs of the sensors be available. In the application of two-mode fiber sensors in harsh environments, it is necessary that the fiber that acts as a conduit, or a lead-in, for the transfer of optical power to the sensing element is not affected by the parameter being measured. Similarly, at the output end of the sensing fiber, it is desirable to have the detection electronics/optics immediately following the sensing portion, or, to carry the information to a remote location via an insensitive, lead-out fiber. Hence, two of the major problems that need to be addressed are the insensitivity of the lead fibers and the development of ruggedized detection schemes.

Several detection techniques for few-mode fiber sensors have been suggested. An elementary technique involves the placement of a spatial demodulator in the form of a pinhole, which samples only part of the far-field pattern [48]. An optical signal processing technique that uses a CCD array for the analysis of the speckle pattern at the output of a highly multimode fiber sensor has been recently demonstrated [53]. This technique can be adapted for a two-mode fiber sensor. We have also used two large-core fibers to pick up parts of the two-lobe, far-field pattern and have obtained satisfactory results. Most such methods used in the past require the output fiber to display the far-field pattern on a monitoring system. This technique is not optimal for remote sensing systems in which the sensing region may be restricted to hard-to-reach environments. The use of misaligned splices seems to eliminate the need to obtain far-field patterns. In such a scheme, a misaligned splice taps light from each mode equally into a single-mode fiber and relative

phase shifts between the LP_{01} and the LP_{11}^{even} modes manifest themselves as intensity variations at the output of the single-mode, lead-out fiber [54]. Kreit et al. have used offset splices with circular-core, two-mode fibers for the implementation of a differential interferometer [55]. Although this technique has been suggested in the past [50,51], experimental methods to achieve insensitive leads as well as detailed results demonstrating such a system have not been reported.

A brief qualitative description of the theory of elliptical-core, few-mode fiber sensors is given here. A thorough review of the theoretical aspects of two- and few-mode optical fiber sensors is given by Duncan [48]. A numerical evaluation of the dependence of the sensor parameters on fiber properties is given by Kumar and Varshney [56]. An analysis of the effect of external perturbation on the differential phase shifts between the two polarizations of each spatial mode as well as between the two spatial modes of each polarization has been presented by Huang et al. [57].

In the weakly-guiding approximation, single-mode circular core fibers can support the two orthogonal polarizations of the LP_{01} mode as well as the four degenerate, higher order, LP_{11} modes when operated just below their single mode cutoff wavelength. Two-lobe patterns can be obtained in the far-field at the output of the fiber and the oscillation of the power distribution between the lobes can be used to sense strain or vibration, as described below. However, environmental conditions can also introduce differential phase shifts between the almost degenerate four eigenmodes leading to an instability of the second-order mode pattern. These degeneracies limit the practical implementation of such sensors by causing the far field pattern to rotate in a random fashion when the fiber is subjected to bending loads.

The use of optical fibers with highly elliptical cores has been shown to remedy this situation [50]. Since the circular symmetry of the fiber has been eliminated, only two second-order modes, the LP_{11}^{even} modes, are guided by the e–core fibers just below the single-mode cut-off wavelength. The intensity distribution of the second order modes is stable and practical operation of a sensor system is possible since there is a considerable range of the optical spectrum over which the LP_{11}^{odd} modes are unguided.

The operation of the sensor can be described with reference to Figure 34. When the LP_{01} and the LP_{11}^{even} modes are excited equally in an e-core fiber, the output radiation pattern will be a superposition of the contributions from the two modes and will be a function of the phase difference between them. The evolution of the two-lobed output pattern for different values of the phase difference, ϕ, is shown in Figure 34 (b), where the ovals represent the bright intensity regions of the far-field pattern. For a change in ϕ of 2π there will be one complete oscillation of the intensity pattern. The analysis presented here will be limited to the nature of the output signals and their dependence on the differential propagation constant, $\Delta\beta$ ($\Delta\beta = \beta_{01} - \beta_{11}$).

The output signal, picked up through a spatial filter, from a two-mode fiber sensor is sinusoidal and can be expressed as

$$I(t) = I_0 + I_{ac} \cos[\phi(t)], \tag{5.1}$$

where ϕ is the phase difference between the LP_{01} and the LP_{11}^{even} modes and can be written as

$$\phi(t) = \int_a^b \Delta\beta \ \varepsilon(x, t)\, dx, \tag{5.2}$$

where ε is the strain experienced by the fiber, $\Delta\beta$ is the difference in the propagation constants of the LP_{01} and the LP_{11}^{even} modes, x denotes the longitudinal direction along the fiber axis, and *a* and *b* denote the two end-points of the two-mode sensing region of the fiber. $\Delta\beta$ is a constant for a standard fiber. In Section 5.4 it will be shown that fibers can be fabricated that allow $\Delta\beta$ to vary along their length, which implies that the strain sensitivity can be a function of the length along the fiber. Measurement of the deformation ΔL required in a specific type of fiber for a 2π change in ϕ, is the first step toward calibrating a strain/vibration sensor based on this principle. For the remainder of this chapter, the amount of strain (ΔL) required to produce a 2π change in ϕ will be defined as the fiber beat length.

The two-mode elliptical-core fiber used in a differential interferometric sensing scheme can be operated in two regimes:

1) The linear range where the induced perturbation is small enough to keep the phase shift between the LP_{01} and the LP_{11} modes to less than π. The resulting output is therefore a varying intensity pattern which depends on the parameter being measured. No fringes are observed.

2) The non-linear range in which large perturbations force the output into the non-linear range thereby inducing fringes. Most fiber optic sensors, being highly sensitive, operate in this mode and fringe counting techniques need to be used in order to process the output signal.

5.2 INSENSITIVE LEAD

The lead insensitive sensor consists of an e-core single mode fiber as the lead-in fiber, an e-core, two-mode fiber as the sensor, and a circular core single mode fiber as the lead-out fiber. The details of the fiber segments are listed in table form in Figure 35 (a). Linearly polarized light is launched parallel to the major axis of the ellipse of the single mode lead-in fiber. The polarization preserving properties of the e-core fiber make this fiber section relatively insensitive to external perturbations. At the first fusion splice, the ellipses of the single-mode and the dual mode fibers may or may not be aligned. This depends entirely on the sensitivity desired from the sensor. It has been shown that the elongation required for a complete oscillation of the two-lobe pattern is smaller for linearly polarized light launched parallel to the minor axis of the ellipse [51]. Hence for maximum sensitivity of the sensor, the major axes of the ellipses of the two fibers being spliced should be perpendicular to each other. However, the trade-off is the loss of optical power, which could lead to a smaller signal-to-noise-ratio and, possibly, a restriction on the maximum length of the lead fibers being used in remote sensing applications. At the second fusion splice, the axes of the sensing fiber and the circular core single mode fiber are offset from each other so the lead-out fiber picks up equal amounts of contribution from the LP_{01} and the LP_{11} modes from only one of the lobes. This splice results in a varying intensity at the output of the single mode fiber that is proportional to the phase difference between the two optical modes in the sensing fiber. The fused lead-out fiber thus acts as an in-line, ruggedized, low-profile spatial demodulator.

The three fibers were fusion spliced actively, as follows:

1) A length of dual mode e-core fiber was wrapped around a piezoelectric cylinder, which was driven by a signal generator at 24 kHz (a resonant frequency of the PZT, which creates a large displacement). Linearly polarized light (λ=633 nm) was launched parallel to the major axis of the elliptical core of the fiber to equally excite the LP_{01} and the LP_{11} modes. The piezoelectric cylinder induced a dynamic strain in the fiber resulting in a known oscillation of the lobes at the fiber output. This variation in optical intensity was monitored actively. The lead-out fiber was offset from the dual-mode fiber to pick up the maximum contrast ratio in the intensity of the two-lobe output and then spliced with a fusion splicer. This process thus achieved the aim of splicing the lead-out fiber to tap off equal amounts of power from both modes.

2) The single mode, e-core, lead-in fiber was aligned with the sensing fiber until a maximum output was obtained from the circular core lead-out fiber. The contrast ratio was compared with that obtained from step 1) above, and the fibers were spliced. The axes of the lead-in and the sensing fibers were parallel to each other. The fusion splice may turn out to be slightly misaligned in order that the two modes are equally excited in the sensing fiber.

To test the lead insensitive splices a measurement of static strain was carried out by holding the fiber ends with micro-positioners and monitoring the output power as the fiber was strained, as shown in Figure 35 (b). A preliminary experiment was first conducted to determine the deformation ΔL in the sensing fiber which would lead to a phase change of 2π. A 70 cm length of dual-mode elliptical core fiber was subjected to strain using a simple micropositioner. The two-lobe pattern at the output was passed through a spatial demodulator to monitor the intensity variation in a single lobe. A linear increase in strain resulted in a sinusoidal intensity variation at the detector placed behind the demodulator. The variation is shown in a normalized form in Figure 36. The amount of deformation, or the beat length, ΔL, required for one oscillation period for the e-core fiber (ANDREW, 1.5 $\mu m \times 2.5\ \mu m$ core, 80 μm cladding) was determined to be 101.6 μm.

To test the insensitivity of the lead-in and the lead-out fibers, only the lead sections were subjected to strain and the output power was measured. Figure 36 shows the variation of the output power for the lead-in and the lead-out fibers on the same scale as that of the sensing fiber. We see that the fluctuation in the lead fiber signals is very small compared to the sensor signal variation. The loss that is observed for large elongations can be attributed to the increase in the attenuation due to the decrease in radius of the fiber. The lead fibers were thus found to be relatively insensitive to static strain effects.

The effects of strain on a spliced fiber system were tested with the apparatus shown in Figure 35 (b). A strain applied to the fiber with the three sections will result in an elongation in each of the sections. It is essential that the elongation in each of the individual sections be quantified to allow evaluation of the strain in the sensing fiber and hence the strain in the system. Consider a sensor with total length L, with the individual lengths of the lead-in fiber, the sensing fiber and the lead-out fiber given by L_1, L_2, and L_3, respectively. The deformation in the total sensor length can be expressed as,

$$\Delta L = \sum_{i=1}^{3} \frac{P_i L_i}{A_i E_i} , \tag{5.3}$$

where P is the longitudinal force applied to the fiber ends, A is the cross-sectional area of the fiber, E is Young's modulus, and the subscript i denotes each of the three sections. Assuming equal forces P_i on each of the segments and approximately the same Young's moduli for each of the three fibers, the deformation (ΔL_2) in the sensing fiber can be calculated for any deformation in the spliced fiber system.

Four sensors were built with different lengths of fiber in each section. The lengths of the fiber sections are given in table form in Figure 37 (a). The goal of this experiment was to determine the deformations ΔL required for the spliced sensors to produce a 2π phase change at the output and then calculate the deformation (ΔL_2) in the sensing fiber. If the effect of the splices and lead fibers on the sensor performance are negligible, the calculated (ΔL_2) should be close to 101.6 μm. Using the values, $A_1 = A_2 = 5026.55$ $(\mu m)^2$ and $A_3 = 12271.85$ $(\mu m)^2$, the required elongations of the spliced fibers were calculated. The four

sensors, described in Figure 37 (a), were subjected to strain and experimental observations for a 2π phase shift were tabulated. The results, along with the errors, are shown in table form in Figure 37 (b).

The results show it is possible to extract information about the strain in the sensing arm from the spliced fiber system to a worst case accuracy of approximately 10 %. Small errors of the order of 0.3 % indicate that the spliced sensor can give a faithful indication of the deformation in the sensing fiber. The errors introduced in the calculations can be reduced by considering the effect of fusion splicing the three sections and the resulting change in the mechanical properties of the fibers. The splices were ruggedized by applying an epoxy around the fused regions and enclosing them in a strain relieved tubing. Despite the precautions taken during the fusion splicing and the strain relieving processes, it is expected that the packaging and the presence of the epoxies introduce errors in the simplistic model described by Equation (5.3).

As a test case, the spliced fiber sensor was attached with an epoxy to a cantilever beam made of aluminum and the tip displacement of the beam was monitored. A schematic of the setup is shown in Figure 38. The elongation in the sensing fiber attached to the cantilever beam can be expressed, in terms of the tip displacement δ_y, as

$$\Delta L = \frac{3\delta_y y}{L^3} \left(L\ell - \frac{\ell^2}{2} \right) , \qquad (5.4)$$

where L is the length of the beam, ℓ is the length of the sensing fiber and y is the distance of the fiber center from the neutral axis of the cantilever beam.

The induced phase shift in the output signal, as related to the tip displacement from Equation (5.2), plotted against the measured phase shift from the fiber optic sensor is shown in Figure 39. The length of the beam, L, was 61.44 cm and the length of the sensing fiber, ℓ, was 56.57 cm. The initial deviation from the theoretical data can be attributed to the effect of improper strain transfer between the binding epoxy and the optical fiber.

5.3 DEMODULATION TECHNIQUES FOR NONLINEAR OPERATION

The problems of nonlinear operation of interferometric sensors was described in Section 2.1 and is also applicable to two-mode fiber interferometric sensors. In the practical implementation of any interferometric scheme, it is essential to maintain the quadrature point (Q-point) of operation for maximum sensitivity. That is, the phase bias which determines the initial point of operation should lie within the linear range of the sinusoidal output curve. Since signal fading is a common problem in an interferometer, it is advantageous to have two signals out of phase by 90°, so that when one of the signals has a low sensitivity to the phase shift (and hence to the parameter being measured), the other signal has a high sensitivity. Several techniques to acquire such phase quadrature signals have been developed for single-mode interferometric systems. Specifically, the use of incorporating frequency or phase modulators to generate heterodyne signals [58], and the development of passive waveguide devices to obtain phase quadrature signals [59-61] have been reported. A scheme using the effect of Gouy phase-shifts has been recently suggested for two-mode elliptical-core fiber sensors [62].

Also as described in Section 2.1, if only one detector is used and the strain changes direction at a peak of the transfer function curve the change in direction of strain would not be detectable. The following paragraphs describe how the two signals, out of phase by 90°, will be obtained for the two-mode fiber sensor.

A 45° splitter-recombiner (S-R) was constructed to obtain two outputs which would be out of phase by 90° to make the desired dynamic strain measurement scheme feasible. The construction procedure was as follows:

1) A stripped e-core fiber was placed between four glass slides (each of dimensions 10 mm × 30 mm × 1 mm) as shown in Figure 40 (a). The fiber was bonded to the glass slides with an epoxy. A small section of the fiber, denoted by length ℓ, was not bonded to allow cleaving.

2) The open section of the fiber was cleaved to create two parts, each comprising of two

glass slides and an e-core fiber sandwiched between them.

3) Both the aforementioned parts were polished at a 45° angle to give a matched pair, shown in Figure 40 (b).

4) The two parts were realigned together with the help of a micropositioner and a liquid with a refractive index of 1.4 was introduced between them to produce a partial reflection.

5) When positioned actively, a part of both the modes was reflected to project the two-lobe pattern on a screen placed directly above the splitter-recombiner. The other portion of the two modes was propagated through the fiber in the second part of the device and a similar two-lobe pattern was obtained at the output of this fiber. This phenomenon is shown schematically in Figure 40 (c).

A description of the method of obtaining a 90° phase shift between the far-field patterns follows.

A HeNe laser (λ=633 nm) launched linearly polarized light into a two-mode, elliptical-core fiber which was wrapped around a piezoelectric cylinder excited at its resonant frequency of 24 kHz. The dynamic strain induced by the piezoelectric cylinder was monitored and the change in direction of the strain was determined by the lead-lag properties of the two signals, as described earlier. A static strain controller placed before the 45° S-R set the initial operating point. Another static strain controller was placed after the 45° S-R to adjust the phase difference between the two detectors D_1 and D_2. Figure 41 (a) shows the outputs of the two detectors before any adjustment of the second static strain controller has been made. In this case, the two signals were very nearly in phase with each other. Minor changes in the second controller led to a shift in the phase between the two outputs. Figure 41 (b) shows the tweaked outputs for an almost quadrature phase shifted system. The phase adjusted system was then used to determine the strain induced in the fiber due to the piezo-electric cylinder. Figure 42 shows that portion of the signal where a change in the direction of the strain takes place. Figure 42 shows that, as predicted, the signals switch their leading / lagging roles when the direction of the phase changes. Counting the number

of fringes on each side of these waveforms gives the magnitude of the strain.

A compact detection scheme can now be envisioned. A block diagram description is shown in Figure 43. It consists of a detection box which includes two detectors, one placed very close to the top surface of the 45° S-R and the other positioned at the output end of the fiber in the second half of the device. Both these detectors would be preceded by spatial demodulators in order to access information from one of the lobes at the far-field pattern. The extra length of the fiber at the output would have to be adjusted to get the desired 90° phase shift between the signals from D_1 and D_2. This phase difference can be permanently achieved by simply grinding and polishing the fiber between the glass slides to the desired length. The outputs from the detection box are taken into a processing unit which contains a comparator and a fringe counter. The comparator performs two functions: 1) it keeps track of the leading / lagging nature of the signals and thus indicates the direction of the strain, and 2) it informs the fringe counter to display a count of the fringes whenever a change in direction takes place. The number of fringes are converted into the induced strain by a process involving pre-calibration for a specific fiber design.

5.4 OPTICAL FIBER SENSORS WITH WEIGHTED SENSITIVITY

The next three sections describe a novel concept for creating a fiber sensor that can selectively enhance the detection of predetermined vibration modes of cantilever beams.

5.4.1 DESCRIPTION AND APPLICATIONS

Fiber optic senors have been used in the past for the measurement of several different parameters such as strain, temperature, pressure, electric and magnetic fields and vibration. Specifically, two-mode elliptical-core (e-core) fibers have been used as efficient vibration mode sensors when operated in the linear region [63]. In a recent paper, it was shown that these ruggedized e-core sensors could perform as vibration-mode filters when placed appropriately along the vibration antinodes of the beam [64].

The motivation for fabricating a sensor with a variable sensitivity along its length can be easily understood when the problem is attacked from a control systems viewpoint. Current

research in vibration sensing and control has shown that variable-sensitivity, spatially-distributed transducers may be more suitable than point sensors for optimal control architectures [65, 66]. Discrete point sensors have been shown to suffer from actuator/observer spillover leading to instabilities in the closed-loop system [67]. The development of piezo-electric spatially weighted sensors has led to extensive research on the advantages of modal sensors and actuators. Modal sensors, which sense the modal coordinate of a particular vibration mode of a structure, can be operated within a control system without extensive on-line real-time computation requirements. In their first description of modal sensors, Lee and Moon made sensing elements out of polyvinylidene fluoride (PVDF) films shaped in the form of specific modes of a structure [66]. The fundamental difference in operation principles between distributed modal sensors and conventional point sensors, as viewed by control systems analysts, is that flexible structures and distributed sensors are both infinite dimensional systems and hence compatible, whereas conventional point sensors are finite dimensional systems and hence require extensive signal processing techniques.

The following derivation will show the theory behind choosing the weighting function for the fiber, beginning with beam mechanics for cantilever beams.

The Euler equation for transverse vibration of beams is given by

$$\frac{\partial^2}{\partial x^2}\left[E\,I(x) \frac{\partial^2}{\partial x^2} y(x,t) \right] + \rho_\ell(x) \frac{\partial^2}{\partial t^2} y(x,t) = Q(t) \ , \tag{5.5}$$

where E is Young's Modulus, I(x) is the Moment of Inertia, ρ_ℓ is the linear density, Q(t) is the forcing function and y(x,t) is the transverse displacement of the beam. Assuming the beams to be isotropic, Equation (5.5) can be simplified to

$$EI \frac{\partial^4}{\partial x^4} y(x,t) + \rho_\ell \frac{\partial^2}{\partial t^2} y(x,t) = Q(t) \ . \tag{5.6}$$

Using the method of separation of variables, the solution will have the form

$$y(x,t) = \sum_{n=1}^{\infty} \psi_n(x)\eta_n(t), \tag{5.7}$$

where $\psi_n(x)$ represent the mode shapes of the beam and $\eta_n(t)$ represent the modal amplitudes. This approach necessitates an infinite sum of natural modes to completely describe the behavior of the beam. For practical implementation, this model can later be truncated to the first few modes of interest. Substituting Equation (5.7) into Equation (5.6) and setting the forcing function, Q(t), to zero we can solve independently for the functions $\psi_n(x)$ and $\eta_n(t)$ and arrive at a solution for the different modes of vibration of the beam.

The equation for $\psi_n(x)$, given by

$$\frac{\partial^4}{\partial x^4}\psi_n(x) - \frac{\rho_\ell a_n^2}{EI}\psi_n(x) = 0 \tag{5.8}$$

has a closed form solution determined by the boundary conditions of the beam. For a clamped-free beam (cantilever configuration), the boundary conditions are expressed mathematically as

$$\psi_n(x = 0) = \psi_n'(x = 0) = 0 \tag{5.9a}$$

and

$$\psi_n''(x = L) = \psi_n'''(x = L) = 0, \tag{5.9b}$$

with these boundary conditions the resulting solution can be written as,

$$\psi_n(x) = \frac{1}{\sqrt{L}}\left[\cosh(a_n x) - \cos(a_n x) - \kappa_n\left[\sinh(a_n x) - \sin(a_n x)\right]\right], \tag{5.10a}$$

where

$$\kappa_n = \frac{\cos(a_n L) + \cosh(a_n L)}{\sin(a_n L) + \sinh(a_n L)} \tag{5.10b}$$

and a_n is a characteristic value given by

$$\cos(a_n L)\cosh(a_n L) + 1 = 0. \tag{5.10c}$$

The key to the weighted sensing approach is that the mode shapes are orthogonal, i.e.,

$$\int_0^L \psi_m(x)\psi_n(x)\,dx = \delta_{mn}\ , \tag{5.11}$$

where δ_{mn} is the Kronecker delta and L is the length of the beam. This property will be used in the design of the fiber-based vibration-modal sensors.

In order to evaluate the vibration modes of the beam, the strain can be expressed as

$$\varepsilon(x, t) = \frac{\partial^2 y(x, t)}{\partial x^2}, \tag{5.12}$$

where y (x, t) denotes the deflection of the beam away from its equilibrium point.

Assuming $\Delta\beta$ (x) ($\Delta\beta$ is described in Equation(5.2) is a constant for standard fibers), and substituting Equation (5.12) into Equation (5.2) and integrating by parts leads to the equation

$$\phi(t) = \eta_n(t)\left(Q(a,b) + \int_a^b \Delta\beta''(x)\,\psi_n(x)\,dx \right), \tag{5.13a}$$

where

$$Q(a,b) = \left[\Delta\beta(x)\,\psi'_n(x)\right]_a^b - \left[\Delta\beta'(x)\,\psi_n(x)\right]_a^b \tag{5.13b}$$

and the primes indicate spatial derivatives with respect to x. Comparing Equations (5.13a) and (5.11) leads one to pick a possible weighting function given by $\Delta\beta''(x) = \psi_m(x)$. Except for the contributions of Q(a,b), $\phi(t)$ would filter out all but the mth mode for a fiber sensor spanning the entire length of the beam. It is possible to weight the information actually present in the structure by using a priori knowledge of the mode shapes of the structure. Instead of relying on the sensor placement to enable structural mode analysis, it would be advantageous if the sensor itself could provide the weighting capability. Hence fairly mode-specific information can be acquired without resorting to conventional analog or digital post acquisition processing. The function Q(a,b) is essentially a constant once the fiber sensor has been attached to (or, embedded in) the structure of interest. For a clamped-clamped beam, if the sensor gage length spans the entire beam, Q(a, b) is identically equal to zero irrespective of the weighting function.

The next two sections present spatially-weighted optical fiber sensors that filter specific vibration modes from one dimensional beams placed in a cantilever configuration. The sensitivity of the sensors is varied along the length of the fiber using two methods: 1) tapered two-mode, circular-core optical fibers, and 2) photoinduced refractive-index changes (gratings) in two-mode, e-core optical fibers. Selective vibration mode suppression on the order of 15 dB has been obtained using the weighted sensors. We describe experimental results and propose future applications for distributed sensors.

5.4.2 TAPERED FIBERS

This section describes a means of achieving the weighting function described in Section 5.4.1, specifically the fiber will be tapered to fabricate a circular-core, two-mode fiber sensor with $\Delta\beta$ as a function of length.

Previous research in the analysis of tapered fibers has used techniques developed by Marcuse [68] and Snyder [69], where the behavior of the propagating modes is analyzed in terms of a coupled-mode formalism that considers the taper as a perturbation. Numerical techniques such as the beam propagation method (BPM) first developed by Feit and Flick for graded-index fibers can also be used for such analyses [70 - 72]. In a recent paper, Bobb *et al.* have provided a complete theory for the analysis of biconical tapers and bends

in single-mode fibers [73]. Most such techniques rely heavily on numerical evaluation of the solutions and are complex. Here drastic assumptions are made in an effort to simplify the problem considerably. By assuming the fiber to be made up of discrete segments, each with its own differential propagation constant and each section acting as a waveguide independent of the section preceding or following it. Another assumption is that individual segments have uniform diameters given by the average values across their lengths.

The characteristic (or eigenvalue) equation for a $LP_{\ell m}$ mode is given by

$$\frac{U_{\ell m} J_{\ell-1}(U_{\ell m})}{J_{\ell}(U_{\ell m})} = \frac{W_{\ell m} K_{\ell-1}(W_{\ell m})}{K_{\ell}(W_{\ell m})}, \tag{5.14}$$

where $U_{\ell m}^2 = k_0^2 a^2 (n_1^2 - \beta_{\ell m}^2)$, $W_{\ell m}^2 = k_0^2 a^2 (\beta_{\ell m}^2 - n_2^2)$, and J and K are Bessel and modified Bessel functions respectively. Equation (5.14) can be evaluated numerically to generate the normalized propagation constants b_{01} and b_{11} for LP_{01} and LP_{11} modes, respectively, as functions of the normalized frequency, V. The definition for the normalized propagation constant is

$$b_{\ell m} = \frac{\frac{\beta_{\ell m}^2}{k_0^2} - n_2^2}{n_1^2 - n_2^2}, \tag{5.15a}$$

and for the normalized frequency,

$$V = \frac{2\pi a}{\lambda} \sqrt{n_1^2 - n_2^2}, \tag{5.15b}$$

where k_0 is the free space propagation constant given by $2\pi/\lambda$, n_1 is the core refractive index, n_2 is the cladding refractive index, λ is the free space wavelength of the source and a is the fiber core radius. The differential propagation constant as a function of V can be obtained, as shown in Figure 44. The range of interest spans values for V ($2.4 < V < 3.8$) over which no modes other than the LP_{01} and LP_{11} modes propagate. For a fiber with a linear taper, the $\Delta\beta''(x)$ is plotted in Figure 45.

Using the orthogonality property of the modes and Equation (5.13), one should be able to tailor fiber profiles that will lead to vibration selective weighted sensors. A direct superposition of the mode shapes and the $\Delta\beta''(x)$ function for different taper profiles shows good correlation. In Figure 46 a comparison is made with the first mode shape of a cantilever beam and a tapered fiber with the minimum radius of $a_{min} = 1$ μm, and the maximum radius $a_{max} = 1.15$ μm with a linear taper over the length of the beam. Similarly, the exponential taper can be tailored such that the weighting function matches the first mode of the clamped-clamped beam. The example demonstrates the possibility of tailoring the weighting profiles as desired for any mode of a cantilever beam. For higher order vibration modes the tapers will have to be more complex with at least one point of inflection between the two end points.

In this experiment the optical fiber sensor had an insensitive, lead-in, single-mode e-core fiber and an offset-spliced, lead-out multimode fiber that would spatially filter the contribution from only one of the two lobes at the output of the sensing region. This procedure is described in detail in Section 5.2.

A conventional e-core sensor was adhered to a cantilever (clamped-free) beam. Output signals from piezo-electric patches attached to the beam were compared to the signals obtained from the fiber sensor. The first three modes of vibration of the beam were excited and the outputs from the fiber optic sensor and the piezo-electric patch were monitored. Figure 47 shows a fast Fourier transform (FFT) of an oscilloscope waveform which shows that the sensor enhances the first mode of vibration in comparison with the piezo-electric sensor, and picks up other modes of vibration fairly well, with reduced sensitivities on the order of 2 and 4 dB for the second and third modes, respectively.

A weighted fiber sensor with a taper that matches the $\Delta\beta''(x)$ function to the first mode of the clamped-free beam was fabricated. The fiber was tapered linearly over the length of the beam. The sensing fiber was fabricated on a draw tower by varying the preform-feed and fiber-pull speeds as well as controlling the temperature of the furnace while the fiber was being drawn. Results obtained from the weighted fiber sensor are shown in Figure 48. The FFT's of the fiber sensor and the piezo-electric patch show that the second mode has

been suppressed by 7 dB and the third mode by 12 dB in comparison to the piezo-electric sensor output, while the first mode has been enhanced by 3 dB.
Modal suppressions of 7 and 12 dB were obtained for the second and third modes of vibration, respectively, for a clamped-free beam; in comparison, the PVDF-based modal sensors developed by Lee and Moon [66] have resulted in a 7.3 dB suppression of the second mode for the fundamental mode sensor and in a 15.45 dB suppression of the fundamental vibration mode for a sensor shaped to enhance the second mode sensitivity. A leak-through phenomenon, where a small response to modes other than those for which the sensor was designed, was also observed by the authors and the discrepancies were attributed to errors in shaping the PVDF films. For fiber optic sensors, a precision-controlled fabrication station is required for the development of such weighting functions and is currently being manufactured. Although only the first mode of vibration was filtered with tapered two-mode fibers, the approach is equally suited for higher-order modal sensing and control using exotic shapes for the fiber tapers.

5.4.3 PHOTOINDUCED GRATINGS

This section describes another means of achieving the weighting function described in Section 5.4.1. Specifically the fiber will be subjected to intense Argon-ion laser light (λ = 514.5 nm) to create periodic permanent refractive-index changes, or gratings. These gratings will be used to fabricate a e-core, two-mode fiber sensor with $\Delta\beta$ as function of length.

Hill gratings were first formed in 1978 by sustained exposure of germanosilicate fibers to a standing interference pattern resulting from two counter-propagating beams within the core [74,75]. Meltz and coworkers subsequently showed that Bragg gratings could be formed in germanium-doped fibers by exposing the core through the side of the cladding by using a transverse holographic method [76]. Recently, permanent index gratings in two-mode, elliptical-core optical fibers have been demonstrated, and several applications such as their use in intermodal switching and chirped filters for dispersion compensation have been proposed [77-79]. While Bragg gratings in single-mode fibers have been used as vibration [80], strain and temperature sensors [81].

To produce a weighted sensitivity fiber sensor, the effects of permanent-index gratings on the differential-phase modulation between the LP_{01} and LP_{11}^{even} modes (beat length) in e-core, two-mode fibers will be examined. The grating-based sensor fabrication process is made up of two distinct stages. First, a high-intensity Argon–ion laser beam (λ = 514.5 nm) is launched into a germanosilicate, e-core, two-mode fiber such that both modes are excited equally; a permanent refractive-index change is created due to the photosensitivity of the germanium-doped core with the same profile and periodicity as the two-lobe pattern as shown in Figure 49 (a). The second stage of the process concerns the use of the grating-induced fiber for sensing purposes by probing the fiber with a low-intensity beam. Such a two-mode fiber, with a permanent grating induced within its core, can no longer be described in terms of the original waveguide equations. Instead of a rigorous theoretical study, a set of experiments were conducted to show the beat length dependence on the induced grating.

Experiments were performed on an elliptical-core fiber (1.5 × 2.5 μm core dimensions) manufactured by Andrew Corporation with a single-mode cutoff wavelength of 628 nm. A linearly-polarized, Argon-ion laser beam (40 mW, 514.5 nm) was launched along the major axis of the fiber and the germanium-doped core was exposed for approximately 30 minutes. The fiber was then probed with a low-power (1 mW, 514.5 nm), x-polarized optical beam and the beat lengths were measured as a function of strain induced in the fiber. Figure 50 (a) shows the variation of the beat length for a fiber that was kept unstrained during the writing process. The gradual decline of the beat length with increasing strain is clearly visible. For fibers that were held at constant strain levels of 0.7%, 1.4 % and 1.8% while being exposed to the high-power beam, resonance (differential phase matching between the grating spacing and $\Delta\beta$) conditions were observed at the corresponding strain levels, as shown in Figures 50 (b) - (d).

These results show that strained fibers exposed to high-power writing beams can be used as sensing elements with varying beat lengths and hence, varying sensitivities. An extension of this concept to weighted sensors makes this effect more significant.

As described in Section 5.4.1, Equation (5.13a), one should pick a possible weighting function given by $\Delta\beta_{eq}''(x) = \psi_n(x)$. Here $\Delta\beta_{eq}''(x)$ is the equivalent $\Delta\beta$, which is not

calculated, and $\psi_n(x)$ is the n^{th} mode shape of the cantilever beam. Except for the contributions of $Q(L)$, from Equation (5.13a), $\phi(t)$ would then filter out all but the n^{th} mode for a fiber sensor spanning the entire length of the beam. Hence fairly mode-specific information can be acquired without resorting to conventional analog or digital post-acquisition processing. Again, the function $Q(L)$ is essentially a constant once the fiber sensor has been attached to (or, embedded in) the structure of interest.

The parameter $\Delta\beta_{eq}''$ can be made to vary as a function of x by inducing an x-dependent strain in a grating-based, two-mode, e-core fiber. The method demonstrated here consists of attaching a fiber to a one-dimensional beam and exposing the germanium-doped core to a high-intensity Argon-ion laser beam. During exposure, the beam is placed under static strain in a shape that is determined by the beam dynamics and the desired variation of the equivalent differential propagation constant. Results from above have shown that the beat length varies almost inversely with strain ($L_B \propto 1/\varepsilon$); this variation implies that $\Delta\beta_{eq}$ would be directly proportional to the induced strain ($\Delta\beta_{eq} \propto \varepsilon_{induced} = \psi_{induced}''$) as a result of the inverse dependence of the beat length and $\Delta\beta_{eq}$. The problem is thus reduced to finding the appropriate strain field to be applied to the beam while the grating is being written in a fiber. Since $\Delta\beta$ is directly proportional to the strain induced in the fiber, its second derivative, $\Delta\beta_{eq}''$, is directly proportional to the fourth derivative of the induced mode shape, $\psi_{induced}''''$. From Equations (5.13a) and (5.13b) and the foregoing argument, in order to selectively sense a specific vibration-mode of order n, the shape of the fiber attached to the beam, $\psi_{induced}$, should be such that its fourth derivative, $\psi_{induced}''''$, is proportional to ψ_n. Hence, the actual shape of the beam is given by [74]

$$\psi_{induced} \propto \iiint \psi_n(x)\, dx. \tag{5.16}$$

For a cantilever beam, the mode shapes ψ_n's are expressed in terms of a linear combination of sine, cosine, hyperbolic-sine and hyperbolic-cosine functions. From the mathematical properties of these functions, one can see that a quadruple integral restores the original functions, except for a scaling factor. As a consequence, the beam needs to be positioned in exactly the same shape as that of the specific vibration-mode one wishes to selectively enhance.

Prior to writing a grating in the fiber, low-power (1 mW, λ = 514.5 nm) probing of a two-mode, e-core fiber sensor provided the vibration-mode information of the cantilever beam under investigation. Fast Fourier transforms (FFT's) of the fiber sensor signal and an adjacent piezo-electric sensor signal attached to the beam are shown in Figure 51. A high-intensity Argon–ion laser beam (40 mW, λ = 514.5 nm) was launched into the germanosilicate, e-core, two-mode fiber attached to a cantilever beam using the experimental setup shown in Figure 52. Note that since the sensing fiber is looped around the beam length the phase parameter given by Equation (5.13a) will be doubled. The launch conditions were set such that both modes were excited equally in order to create a permanent refractive-index change with the same profile and periodicity as the two-lobe pattern. The beam was held in its second vibration-mode shape during the high-power exposure of the fiber core. Post-exposure analysis of the fiber sensor with a low-power beam at 514.5 nm resulted in the output signal shown in Figure 53. A comparison of Figures 51 and 53 indicates that the fiber sensor has suppressed the first mode of vibration by 15 dB. Note that the comparison is made between the relative magnitudes of the FFT's of the fiber output and the piezo-electric sensor signal in Figure 52 and then compared to the difference in the relative amplitudes of the corresponding signals in Figure 51 in order to eliminate any discrepancies that may arise due to excitation conditions.

In conclusion, the behavior of a two-mode, elliptical-core fiber gratings have been experimentally analyzed. And a two-mode, elliptical-core fiber with a chirped grating, with the sensitivity varying as a function of length, has been demonstrated as a selective vibration-mode sensor.

6. Conclusions

This dissertation described several novel phase-modulated optical fiber sensors. For each fiber sensor, a complete description of the theory and method of operation was given, and the fabrication procedures and the results of successful demonstrations were presented.

The extrinsic Fabry-Perot interferometric (EFPI) fiber optic strain gage was analyzed, fabricated, and tested as a high temperature strain monitor. The EFPI was compared to conventional resistive strain gages on an F-15 aircraft at Wright Patterson Air Force Base. Static and dynamic loading tests showed 0.01 microstrain resolution for the EFPI. Absolute displacements were also measured using the EFPI with a resolution of 5 nanometers. Finally, four EFPIs were used in a n impact detection and location system. Current research includes multiplexing issues, reliability testing, and designing and EFPI for operation at even higher temperatures.

The temperature insensitive Michelson interferometer (TIMI) has been demonstrated as a displacement sensor with sub-Angstrom resolution, and as a pressure transducer at NASA Langley. Current research involving the TIMI includes the measurement of absolute displacements of surface acoustic waves, and magnetic fields by monitoring the displacement of magnetostrictive materials.

The sapphire fiber interferometer was demonstrated in a temperature configuration up to 1700 °C. Current research involving the sapphire fiber interferometer includes a pressure transducer for monitoring pressure waves in jet and rocket engines, and a strain gage for attached and embedded materials inspection and evaluation.

Several elliptical-core, two-mode fiber sensors were proposed and demonstrated. The weighted fiber sensors described showed the ability of the fiber to selectively enhance the the detection of predetermined vibration mode shapes.

Developing new methods of fabricating the optical fibers with weighting functions will likely be an important area of future research. Two methods, tapers and photo-induced gratings, of producing the weighting function have been described and demonstrated.

Other possible methods of producing the weighting function include fibers that have been modified using dopant diffusion, or etching and recladding techniques.

Another important area of future research involving the spatially-weighted fiber sensors is the development of a weighted sensor that can be tuned. The tuning function can be realized by scanning wavelengths of the probe or interrogating optical beam to change the vibration mode selectivity. In other words, by changing the wavelength of operation the sensor can selectively filter any particular mode of vibration, i.e. the first, second, or third mode of vibration. The sensor can also be used to detect changes in vibration mode shape that result from damage, or controlled reconfiguration of the structure.

References

1. B. Culshaw, *Optical fibre sensing and signal processing*, Peter Peregrinus, London (1984).
2. R. O. Claus, K. D. Bennett, A. M. Vengsarkar, and K. A. Murphy, "Embedded optical fiber sensors for materials evaluation," J. Nondestructive Evaluation, 8:2: 371-381 (1989).
3. R.O. Claus, editor, Proc. of the Conf. on Optical Fiber Sensor-Based Smart Materials and Structures, Technomic Publishing, Virginia Tech, Blacksburg, VA.
4. J. M. van Oort, "The application of extrinsic Fabry-Perot fiber-optic strain sensors in accelerator dipole magnets," Proc. of the Conf. on Optical fiber sensor-based smart materials and structures, Virginia Tech, Blacksburg, VA (1992).
5. T. Yoshino, K. Kurosawa, K. Itoh, and T. Ose, "Fiber-Optic Fabry-Perot Interferometric," IEEE J. Quantum Electron., v. QE-18, 1624 (1982).
6. K. L. Belsley, J. B. Carroll, L. A. Hess, D. R. Huber, and D. Schmadel, "Optically Multiplexed Interferometric Fiber Optic Sensor System," Proc. Soc. Photo–Opt. Instrum. Eng., v. 566, 257 (1985).
7. A. D. Kersey, D. A. Jackson, and M. Corke, "A Simple Fibre Fabry-Perot Sensor," Opt. Comm., v. 45, 71 (1983).
8. C. E. Lee and H. F. Taylor, "Interferometric Opitcal Fibre Sensors Using Internal Mirrors," Electron. Lett, v. 24, 193 (1988).
9. G. Keiser, *Optical Fiber Communications*, McGraw-Hill Inc., New York, 1983.
10. J. Putz, J. Putz, A. Wicks, and T. Diller, "Thin-film shear stress gage," Proc. ASME Winter Annual Meeting, Symposium on Micro Structures, Sensors and Actuators, Dallas, November 26 (1990).
11. K. A. Murphy, M. F. Gunther, A. M. Vengsarkar and R. O. Claus, "Quadrature phase-shifted, extrinsic Fabry-Perot optical fiber sensors," Opt. Lett., vol. 16, pp. 273-275 (1991).
12. A. Dandridge, A. B. Tveten and T. G.Giallorenzi, "Homodyne demodulation scheme for fiber optic sensors using phase generated carrier," IEEE J. Quantum Electron., vol. QE-18, pp. 1647-1653 (1982).

13. K. Krakenes and K. Blotekjaer, "Sagnac interferometer for underwater sound detection: Noise properties," Opt. Lett., vol. 14, pp. 1152-1154 (1989).
14. K. S. Chiang, H. L. W. Chan and J. L. Gardner, "Detection of high-frequency ultrasound with a polarization-maintaining fiber," J. Lightwave Technol., vol. 8, pp. 1221-1227 (1990).
15. J. J. Alcoz, C. E. Lee and H. Taylor, "Embedded fiber-optic Fabry-Perot ultrasound sensor," IEEE Trans. Ultrason. Ferroelectric. and Freq. Control, vol.37, pp. 302-305 (1990).
16. J. S. Sirkis and H. W. Haslach, "Interferometric strain measurement by arbitrarily configured, surface-mounted, optical fibers," J. Lightwave Technol., vol. 8, pp. 1497-1503 (1990).
17. D. A. Jackson, R. Priest, A. Dandridge, and A. B. Tveten, "Elimination of drift in a single-mode optical fiber interferometer using a piezoelectrically stretched coiled fiber," Appl. Opt., vol. 19, pp. 2926-2929 (1980).
18. A. Tobias, "Acoustic emission source location in two dimensions by an array of three sensors," Nondestructive testing, v. 9, no. 1, pp. 9-12 (1976).
19. M. Asty, "Acoustic emission source location on a spherical and plane surface," NDT International, v. 11, no. 5, pp. 223-226 (1978).
20. V. M. Bobrenko and L. M. Polesskaya, "Determination of the coordinates of an acoustic-emission source by two pairs of receivers," Acoustical Methods, Plenum Plublishing Corporation (1981).
21. W. B. Spillman Jr. and P. L. Fuhr, "Impact detection and location system for smart skins applications," Proc. Soc. Photo-Opt. Instrumentation Eng., v. 1370, pp. 308-315, San Jose, CA (1990).
22. T. Tran, W. Miller, K. A. Murphy, A. M. Vengsarkar, and R. O. Claus, "Extrinsic Fabry-Perot fiber optic sensor for surface acoustic wave detection," Proc. Soc. Photo-Opt. Instrumentation Eng., v. 1584, pp. 178-186, Boston (1991).
23. C. D. Butter, and G.D. Hocker, "Fiber optics strain gage," Appl. Opt., vol. 17, pp. 2867-2869 (1978).
24. I. A. Viktorov, "Investigation of methods for exciting Rayleigh waves," Soviet Physics -Acoustics, vol. 7, pp. 236-244 (1962).
25. H. Kolsky, Stress Waves in Solids, Dover Publications, Inc., New York,(1963).

26. R. J. Wasley, *Stress Wave Propagation in Solids*, Marcel Dekker, Inc., New York (1973).
27. W. M. Ewing, W. S. Jardetzky, and F. Press, *Elastic Waves in Layered Media,* McGraw-Hill Book Co., Inc., New York (1957).
28. R. V. Schmidt, "Acoustooptic interactions between guided optical waves and acoustic surface waves," IEEE Trans. Sonics and Ultrason., vol. SU-33, pp. 22-33 (1976).
29. M. Abramowitz and I. Stegun, *Handbook of Mathematical Functions,* National Bureau of Standards,Washington, DC (1972).
30. A. Dandridge and A. B. Tveten, "Phase compensation in interferometric fiber-optic sensors," J. Opt. Soc. Amer., vol. 7, pp. 279-281 (1982).
31. E. Udd, ed., *Fiber Optic Sensors*, Wiley-Interscience, New York (1991).
32. S. E. Baldini, et al, "Cooperative implementation of a high temperature acoustic sensor," Proc. SPIE, vol. 1588, Boston, MA, September (1991).
33. K. A. Murphy, et al., "Sapphire fiber interferometer for microdisplacement measurements at high temperature," Proc. SPIE, vol. 1588, Boston, MA (1991).
34. K. A. Murphy, R. O. Claus and S. B. Desu, "Smart structures for fossil energy applications," Proc. Pittsburgh Energy Technology Center Conference, Pittsburgh, PA, September (1990).
35. A. Raheem, S. B. Desu and R. O. Claus, "High temperature refractory coating materials for sapphire waveguides," Proc. SPIE, vol. 1170, September (1989).
36. K. A. Murphy, M. F. Gunther, A. M. Vengsarkar, and R. O. Claus, "Fabry-Perot Fiber Optic Sensors in Full Scale Fatigue Testing on an F-15," Applied Optics, v. 31, no. 4, pp. 431-433, (1992).
37. J. A. Bucaro, H. D. Dardy, and E. F. Carome, "Optical fiber acoustic sensor," Applied Optics, v. 16, p. 1761 (1977).
38. F. R. Trowbridge and R. L. Phillips, "Metallic glass fiber-optic phase modulators," Optics Letters, v. 6, p. 636 (1981).
39. G. B. Hocker, " Fiber optic sensing of pressure and temperature," Applied Optics, v. 18, p. 1445 (1979).
40. D. A. Jackson, R. Priest, A. Dandridge, and A. B. Tveten, "Elimination of drift in a single-mode optical fiber interferometer using a piezoelectrically stretched coiled fiber," Applied Optics, v. 19, p. 2926 (1980).

41. H. Hosokawa, J. Takagi, and T. Yamashita, "Y-junction interferometer," Optical Fiber Sensors Conference, Technical Digest Series, v. 2, Part 1, p. 137, Conference Edition, New Orleans, LA (1988).
42. K. P. Koo, A. B. Tveten, and A. Dandridge, "Passive stabilization scheme for fiber optic interferometers using (3x3) fiber directional couplers", Applied Physics Letters, v. 41, pp. 616-618 (1982).
43. A. Olsson, C. L. Tang, and E. L. Green, "Active stabilization of a Michelson interferometer by an electrooptically tuned laser", Applied Optics, v. 19, pp. 1897-1899 (1980).
44. P. D. Dean, M. F. Bramlette, and R. H. Burrin, "Survey of Pressure Sensors for High-Temperature/High-Acoustic Environments," Lockheed Research Technical Report No. 31699 (1990).
45. R. F. Hellbaum, M. F. Gunther, K. A. Murphy, and R. O. Claus, "An Experimental Fiber Optic Microphone for Measurement of Acoustic Presure Levels in Hostile Environments," Sensors Expo 91, Chicago, Illinois, October 1-3 (1991).
46. M. Digiovanni, Flat and Corrugated Diaphragm Design Handbook, Marcel Dekker, Inc., New York (1982).
47. M. R. Layton and J. A. Bucaro, "Optical fiber acoustic sensor utilizing mode-mode interference," Applied Optics, v. 18, p. 666 (1979).
48. B. D. Duncan, "Modal interference techniques for strain detection in few-mode optical fibers," Master of Science Thesis, Department of Electrical Engineering, Virginia Polytechnic Institute and State University, April (1988).
49. A. Safaai-Jazi and R. O. Claus, "Synthesis of interference patterns in few-mode optical fibers," Proc. SPIE, v. 986, p. 180 (1988).
50. B. Y. Kim, J. N. Blake, S. Y. Huang, and H. J. Shaw, "Use of highly elliptical core fibers for two-mode fiber devices," Applied Optics, v. 12, p. 729 (1987).
51. J. N. Blake, S. Y. Huang, B. Y. Kim, and H. J. Shaw, "Strain effects on highly elliptical core two-mode fiber devices," Applied Optics, v. 12, p. 732 (1987).
52. B. Y. Kim, J. N. Blake, H. Engan, H. J. Shaw, "All-fiber acousto-optic frequency shifter," Optics Letters, v. 11, p. 389 (1986).
53. W. B. Spillman, Jr., B. R. Kline, L. B. Maurice, and P. L. Fuhr, "Statistical-mode sensor for fiber optic vibration sensing uses," Applied Optics, v. 28, p. 3166 (1989).

54. M. Imai and E. H. Hara, "Excitation of the fundamental and low order modes of optical fiber waveguides with Gaussian beams . Part 2: Offset beams," Applied Optics, v. 14, p. 169 (1975).
55. D. Kreit, R. C. Youngquist, and D. E. N. Davies, "Two-mode fiber interferometer/amplitude modulator," Applied Optics, vol. 25, p. 4433 (1986).
56. Arun Kumar and R. K. Varshney, "Propagation characteristics of dual-mode elliptical-core optical fibers," Optics Letters, v. 14, p. 817 (1989).
57. S. Y. Huang, J. N. Blake, and B. Y. Kim, "Perturbation effects on mode propagation in highly elliptical core two-mode fibers," To appear in Journ. Lightwave Technology.
58. J. H. Cole, B. A. Danver, and J. A. Bucaro, "Synthetic heterodyne interferometric demodulation", IEEE Journ. Quant. Electron., QE-18, p. 694 (1982).
59. B.Y. Kim and H. J. Shaw, "Phase-reading all-fiber-optic gyroscope", Optics Letters, v. 9, p. 378 (1984).
60. T. Niemeier and R. Ulrich, "Quadrature outputs from fiber interferometer with 4 × 4 coupler," Optics Letters, v. 11, p. 677, (1986).
61. D. W. Stowe and T. Y. Hsu, "Demodulation of interferometric sensors using a fiber-optic passive quadrature demodulator", Journ. Lightwave Technol., LT-1, p. 519 (1983).
62. S. Y. Huang, H. G. Park, and B. Y. Kim, "Novel quadrature phase detector using two-mode waveguides", To appear in Optics Letters.
63. K. A. Murphy, M. S. Miller, A. M. Vengsarkar, and R. O. Claus, "Elliptical-core, two-mode, optical fiber sensor implementation methods," J. Lightwave Technol., v. 8, p. 1688 (1990).
64. A. M. Vengsarkar, B. R. Fogg, W. V. Miller, K. A. Murphy, and R. O. Claus, "Elliptical-core, two-mode optical fibre sensors as vibration mode filters," Electron. Lett., v. 27, pp. 931-932, June (1991).
65. T. Bailey and J. E. Hubbard, "Distributed piezoelectric-polymer active vibration control of a cantilever beam", J. Guid. and Contr., v. 8, pp. 605 - 611 (1985).
66. C. -K. Lee and F. C. Moon, "Modal sensors/actuators," J. Appl. Mechanics, vol. 57, pp. 434-441 (1990).
67. M. J. Balas, "Feedback control of flexible systems," IEEE Trans. Auto. Contr, v. 23, pp. 673-679 (1978).
68. D. Marcuse, *Theory of Dielectric Waveguides*, Second Edition, Academic (1991).

69. A. W. Snyder and J. D. Love, *Optical Waveguide Theory*, Chapman & Hall (1983).
70. M. D. Feit and J. A. Fleck, "Light propagation in graded-index optical fibers," Appl. Opt., v. 17, pp. 3990-3998 (1978).
71. M. D. Feit and J. A. Fleck, "Calculation of dispersion in graded-index multimode fibers by a propagating beam method," Appl. Opt., v. 18, pp. 2843-2851 (1978).
72. J. Van Roey, J. Van der Donk, and P. E. Lagasse, "Beam propagation method: analysis and assessment," J. Opt. Soc. Am., v. 71, pp. 803-810 (1981).
73. L. Bobb, P. M. Shankar, and H. D. Krumboltz, "Bending effects in biconically tapered single-mode fibers," J. Lightwave Technol., v. 8, pp. 1084-1090 (1990).
74. A. M. Vengsarkar, J. A. Greene, and K. A. Murphy,"Photo-induced refractive-index changes in two-mode, elliptical-core fibers: Sensing application," Optics Letters, v. 16, no. 19, pp. 1541-1543, October (1991).

Figures

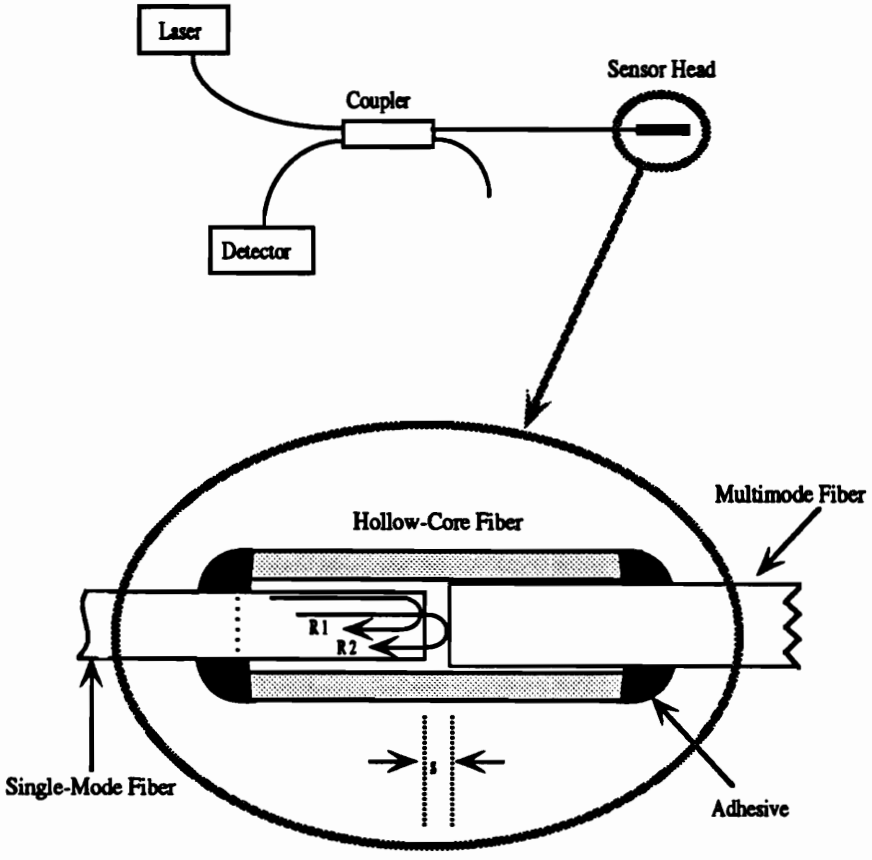

Figure 1. Construction of extrinsic Fabry-Perot sensor.

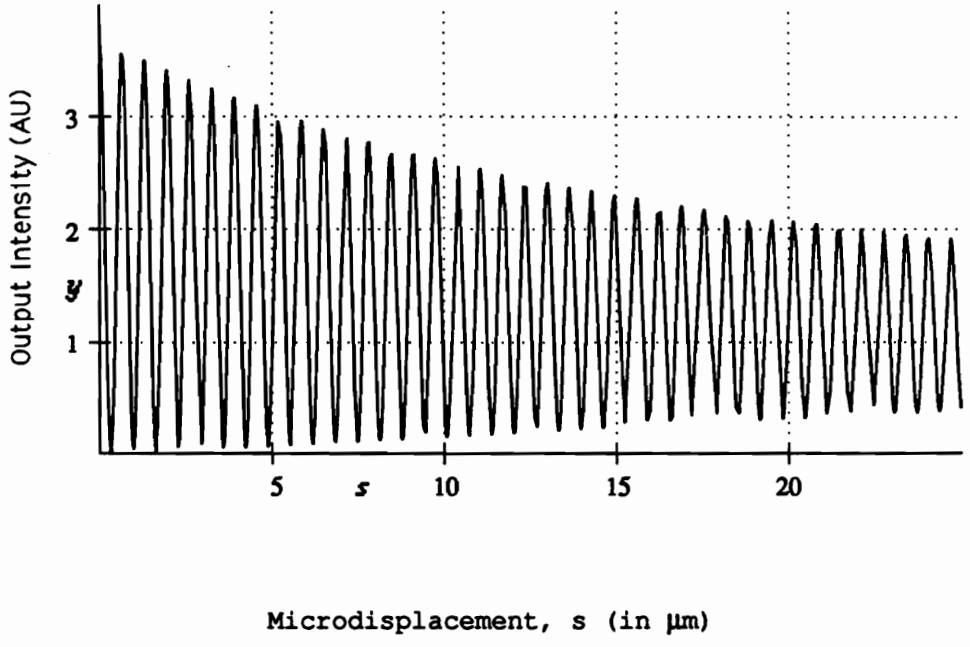

Figure 2. Theoretical plot of the variation of output intensity with increasing gap displacement.

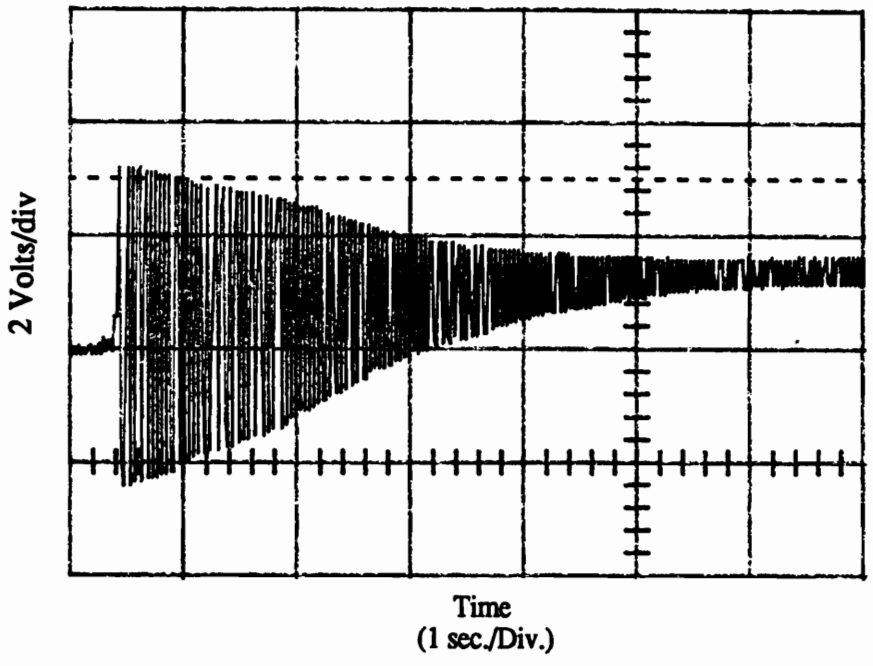

Figure 3. Oscilloscope trace of observed fringes for increasing gap displacement.

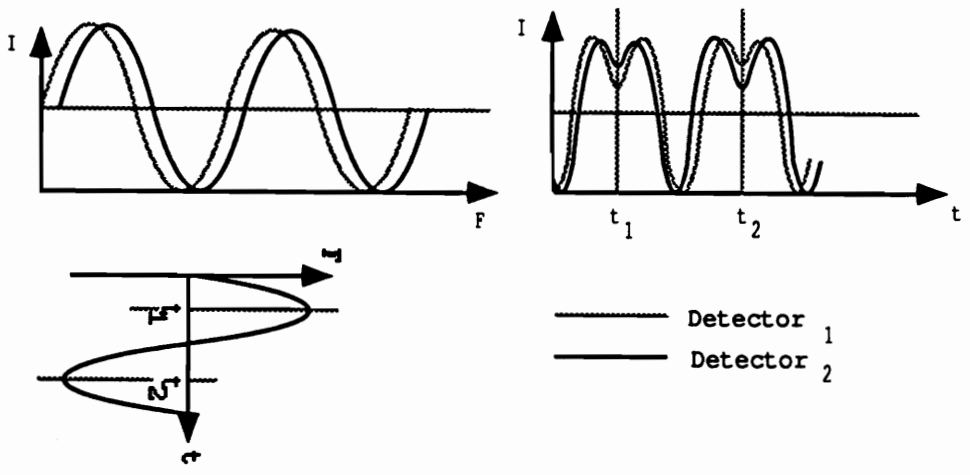

Figure 4. Principle of operation of quadrature phase-shifted sensors.

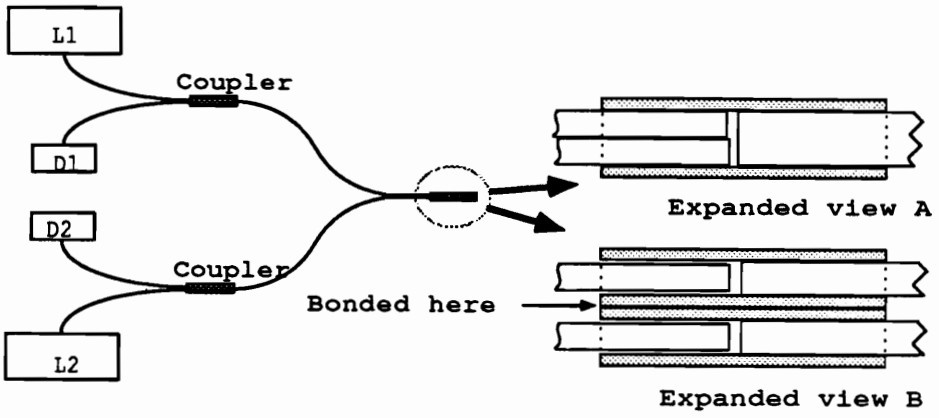

Figure 5. Quadrature phase-shifted sensors.

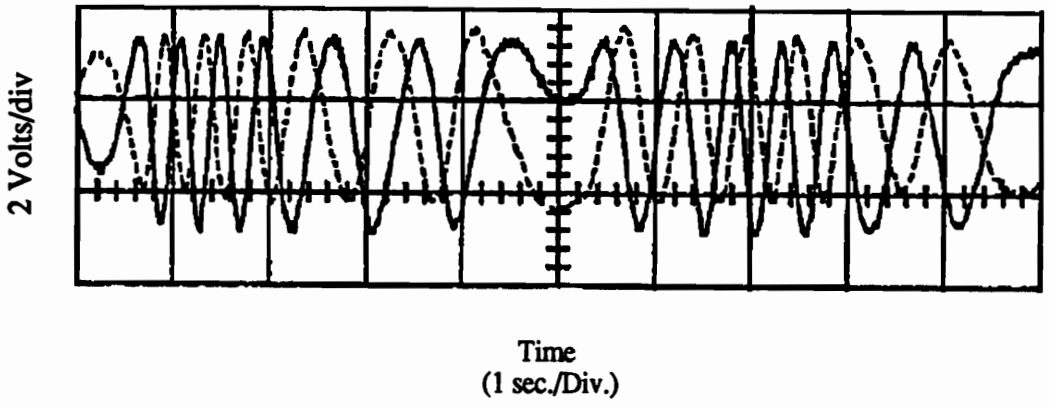

Figure 6. Oscilloscope trace of quadrature phase-shifted sensors showing lead-lag phenomenon.

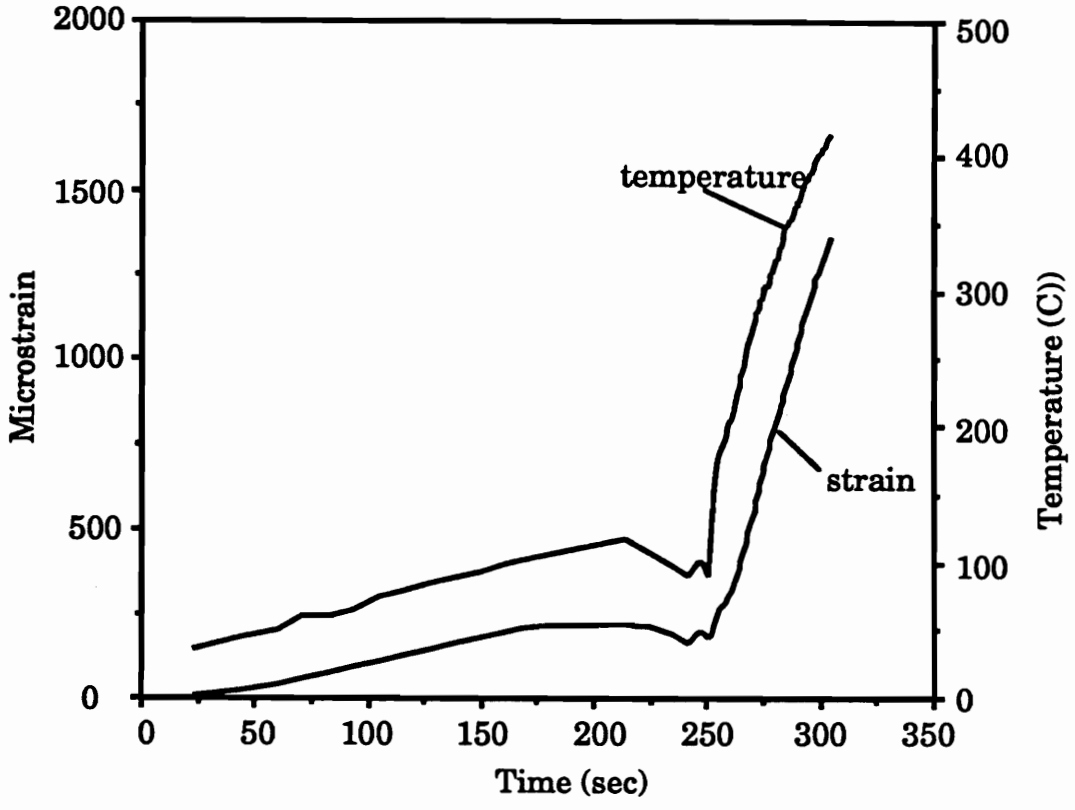

Figure 7. Results from Fabry-Perot sensor during high temperature testing at Westinghouse Science and Technology Center.

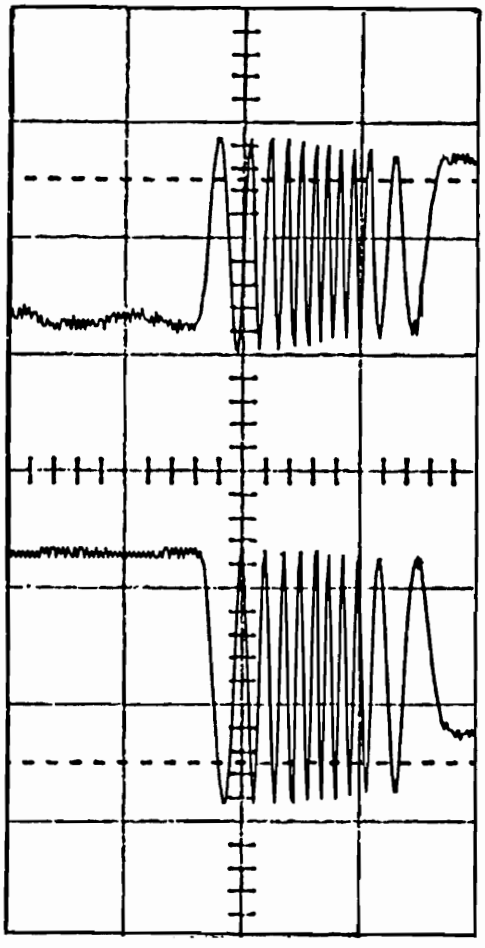

Figure 8. Sensor output waveforms for static loading from 20 to 40% loading. Horizontal scale: time/division, 1second, Vertical scale: voltage/division, 1 Volt.

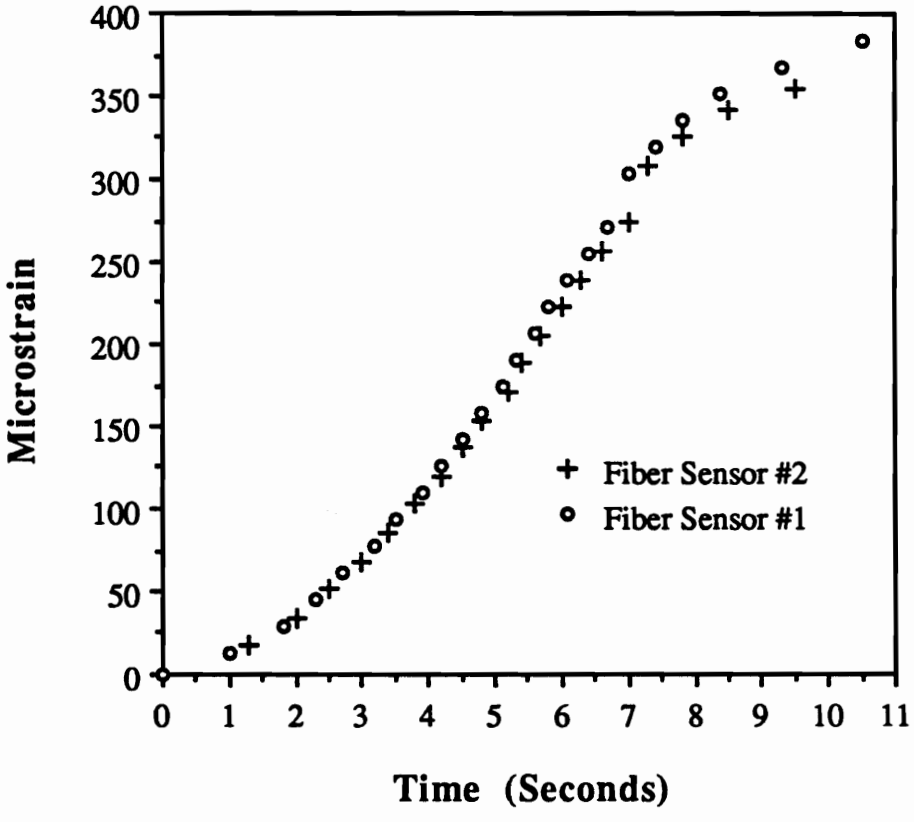

Figure 9. Data processor output showing the variation of strain versus time. Typical output waveforms shown in Figure 8 were fed into a computer program to acquire strain information versus time.

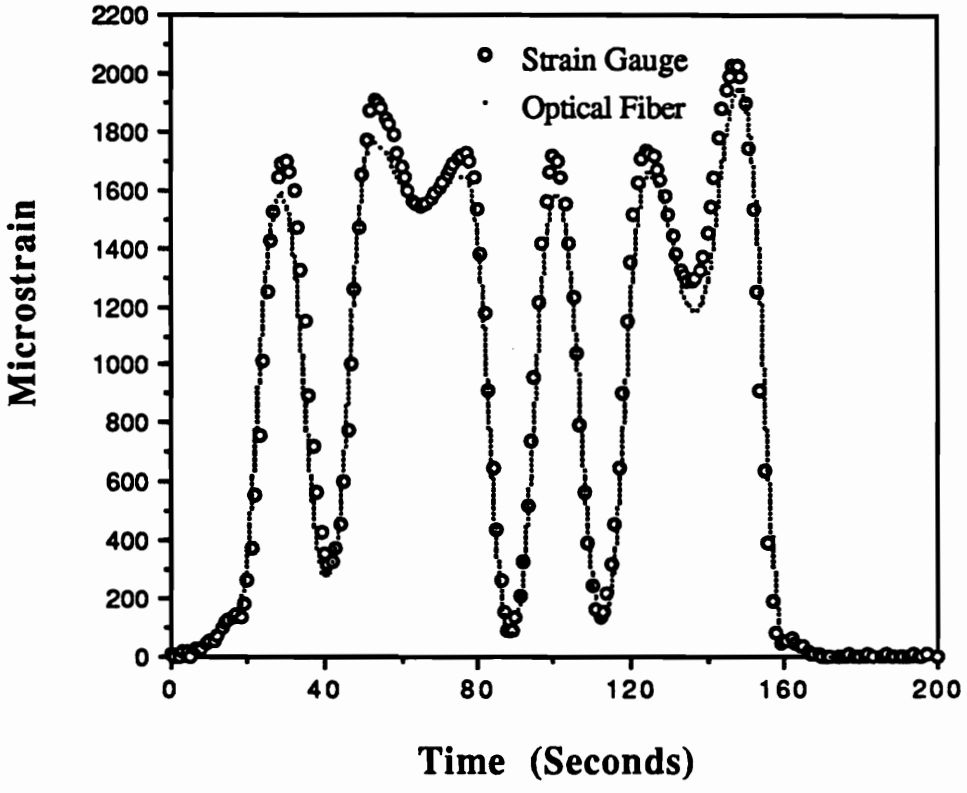

Figure 10. Processed output showing measured strain as a function of time during the loading cycle.

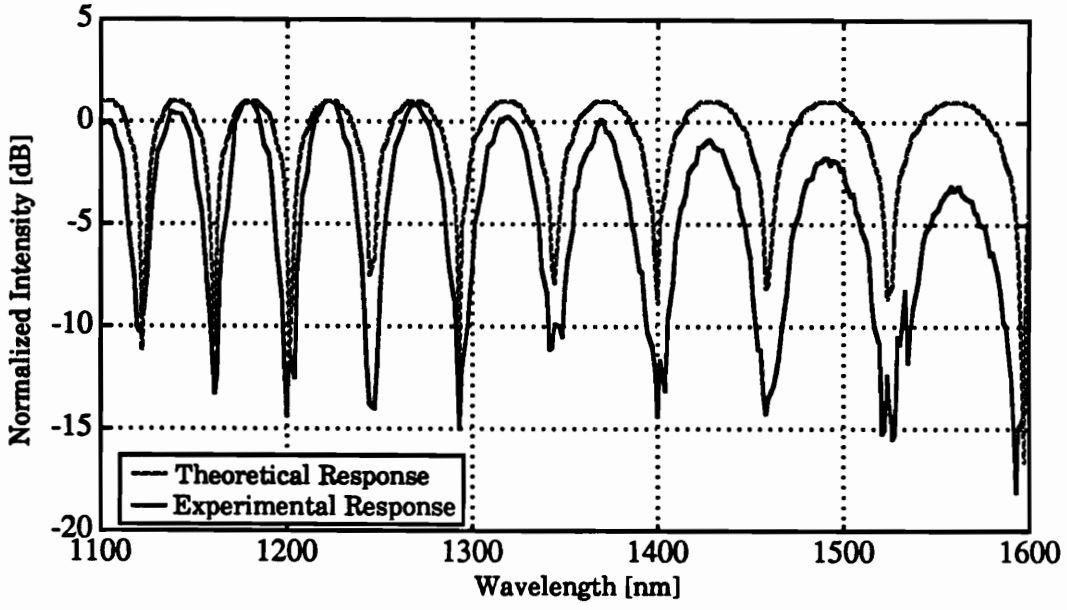

Figure 11. Sensor output as a function of wavelengths.

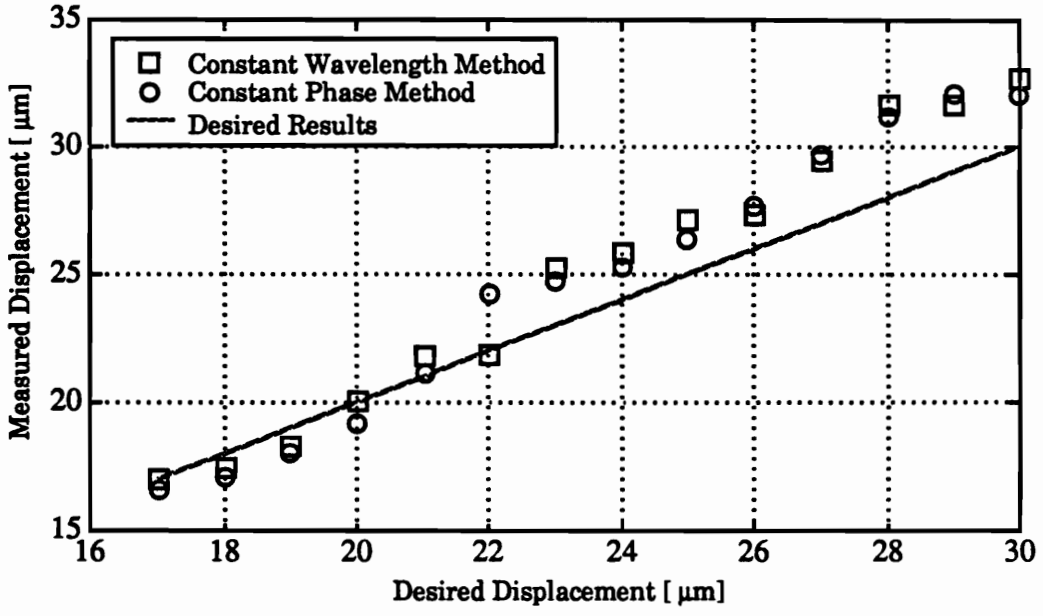

Figure 12. Displacement sensor output compared with positioner reading.

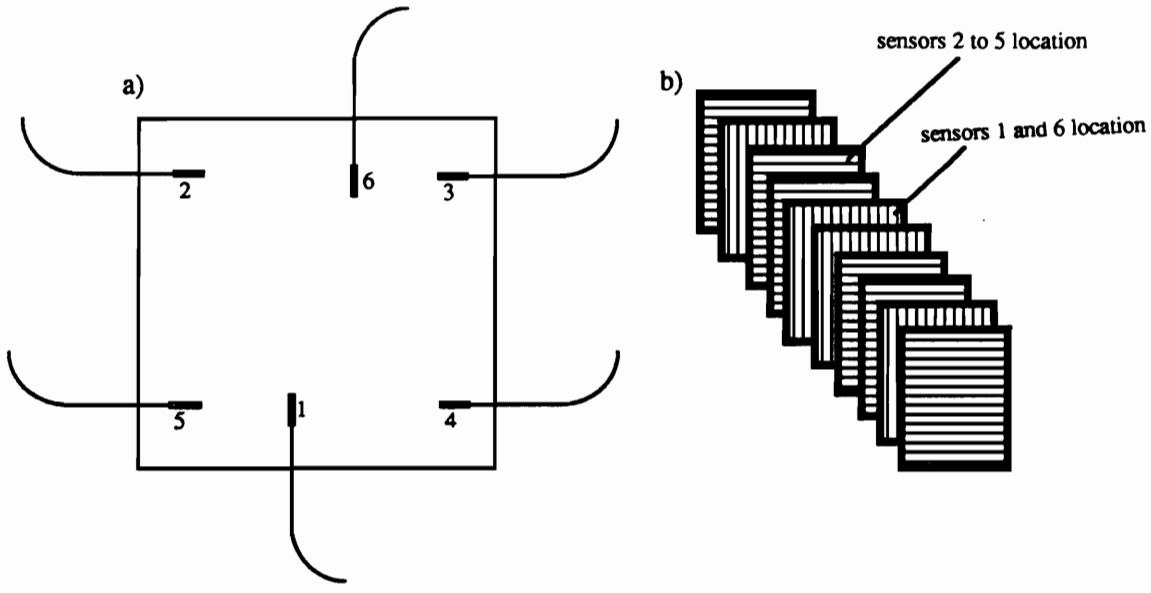

Figure 13. Schematic of EFPI sensors in a composite panel, a) sensor placement, b) location of sensors within composite layers.

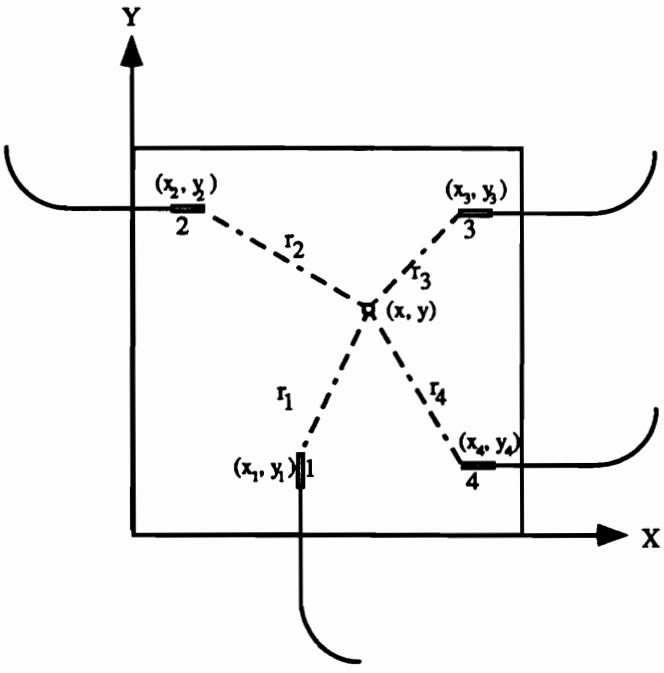

Figure 14. Development of coordinate system for impact location determination.

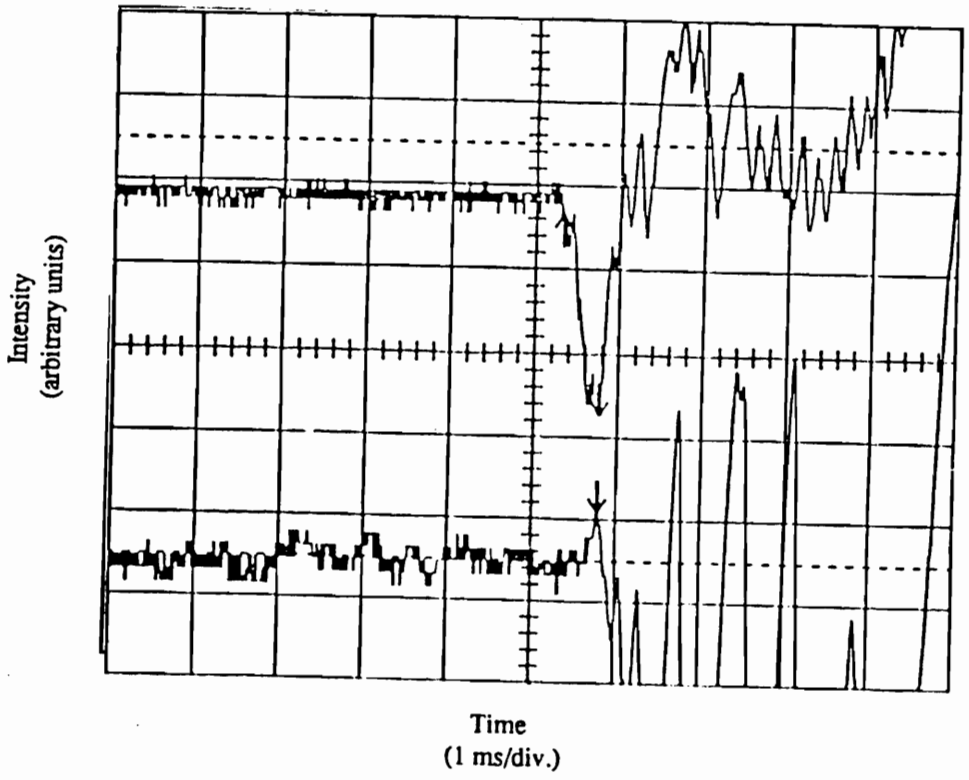

Figure 15. Output of sensors 5 (top) and sensor 2 (bottom) during impact.

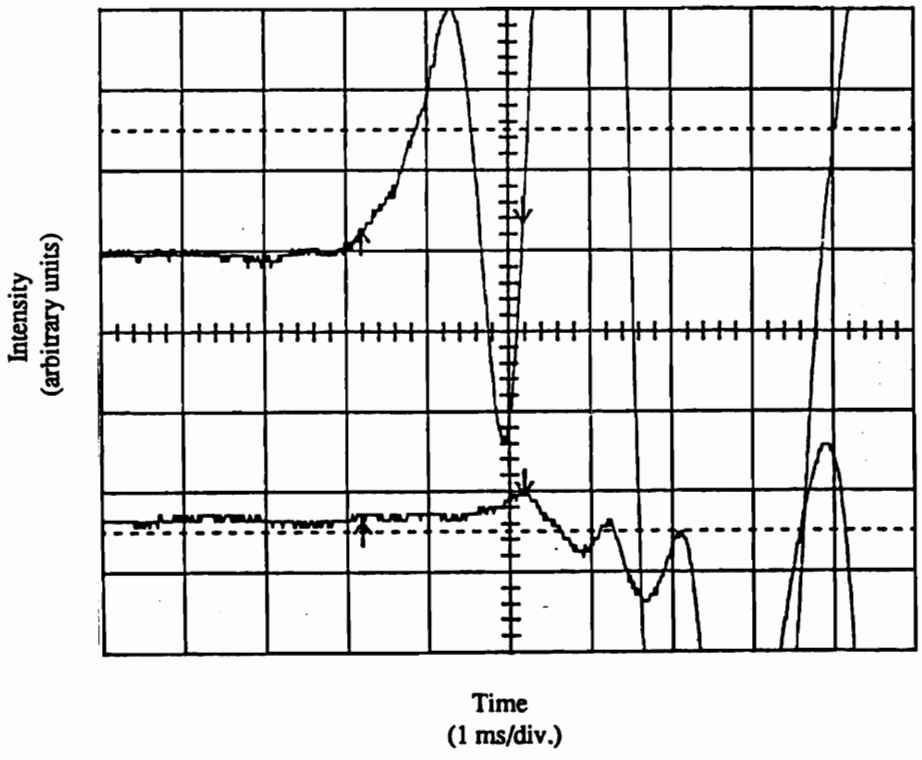

Figure 16. Output of sensors 4 (top) and sensor 2 (bottom) during impact.

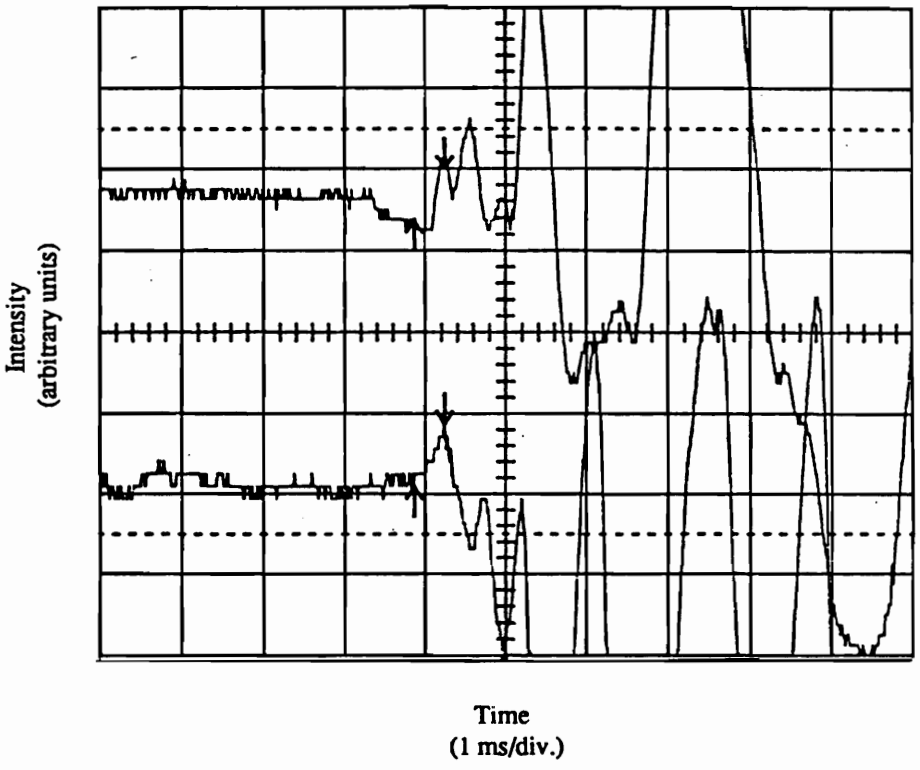

Figure 17. Output of sensors 3 (top) and sensor 2 (bottom) during impact.

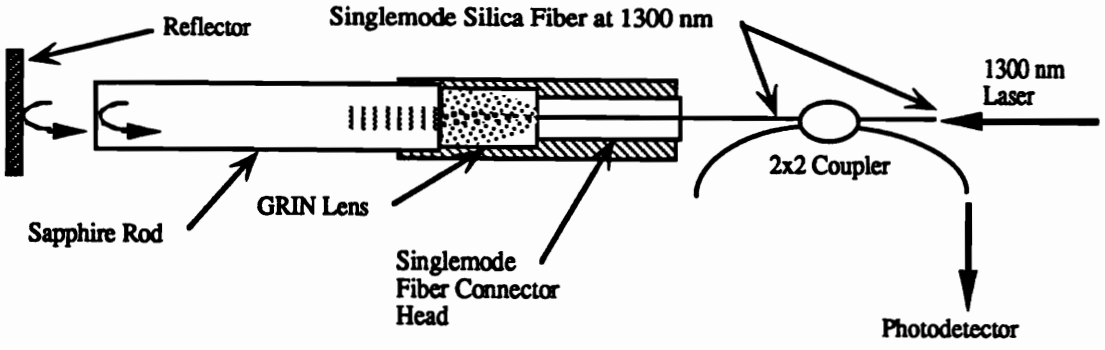

Figure 18. Example of sapphire rod interferometer as displacement sensor.

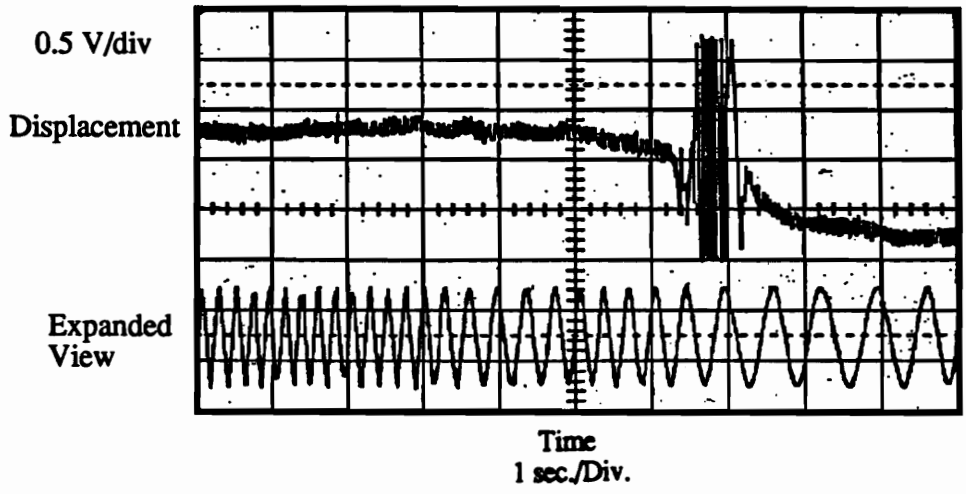

Figure 19. Displacement experiment of sapphire sensor.

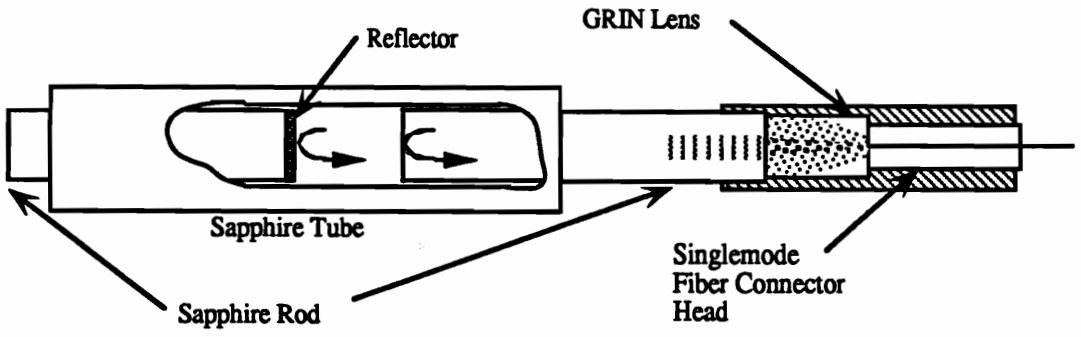

Figure 20. Sapphire extrinsic Fabry-Perot interferometer (EFPI).

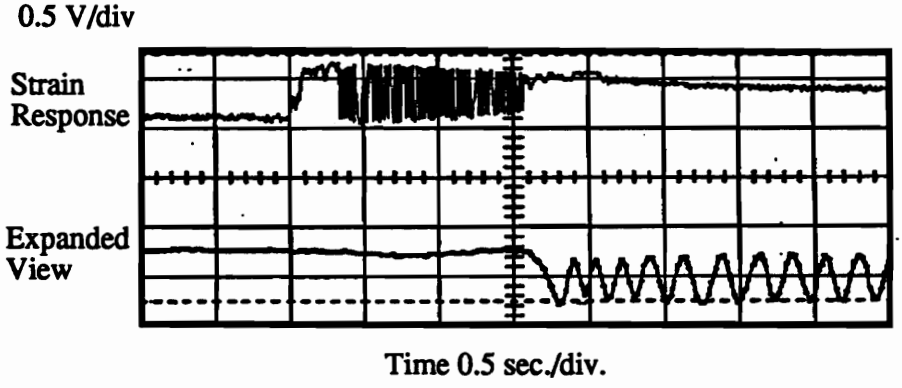

Figure 21. Oscilloscope trace of sapphire EFPI response to strain.

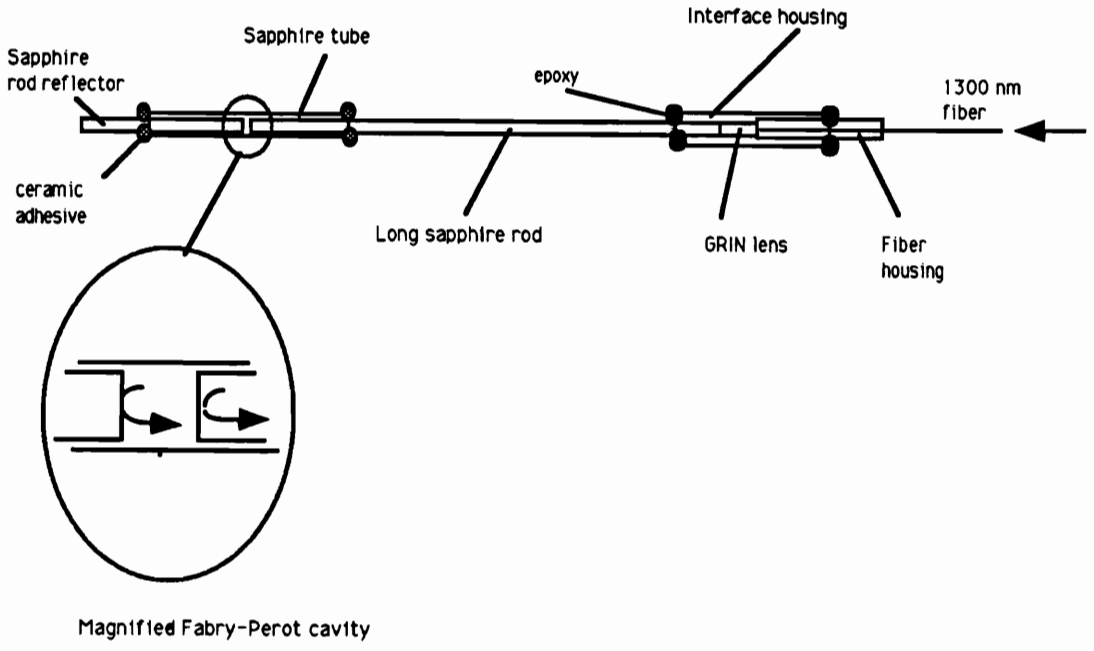

Figure 22. Long sapphire EFPI sensor to reduce heat transfer to optical components.

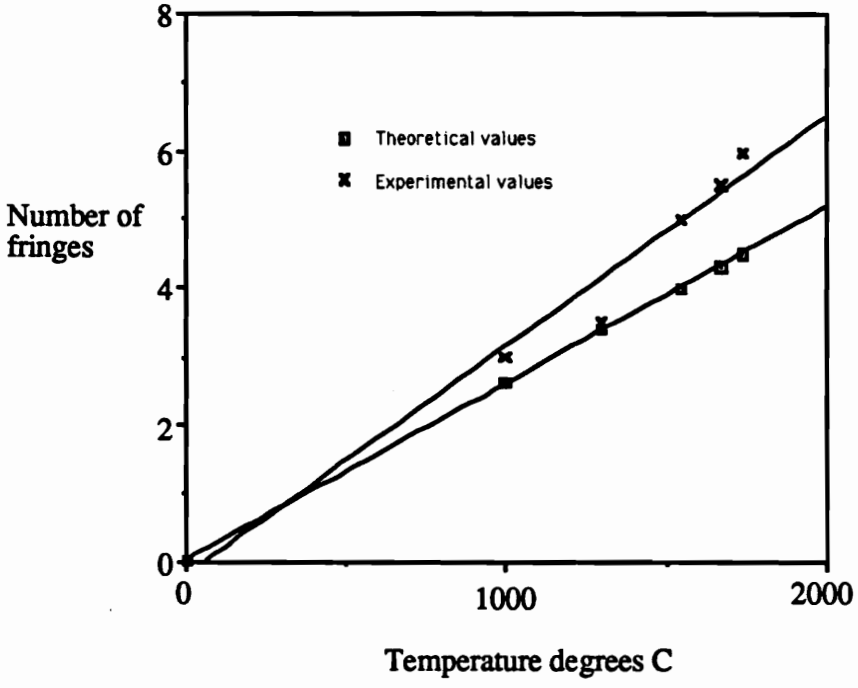

Figure 23. Experimental data from sapphire EFPI high temperature tests.

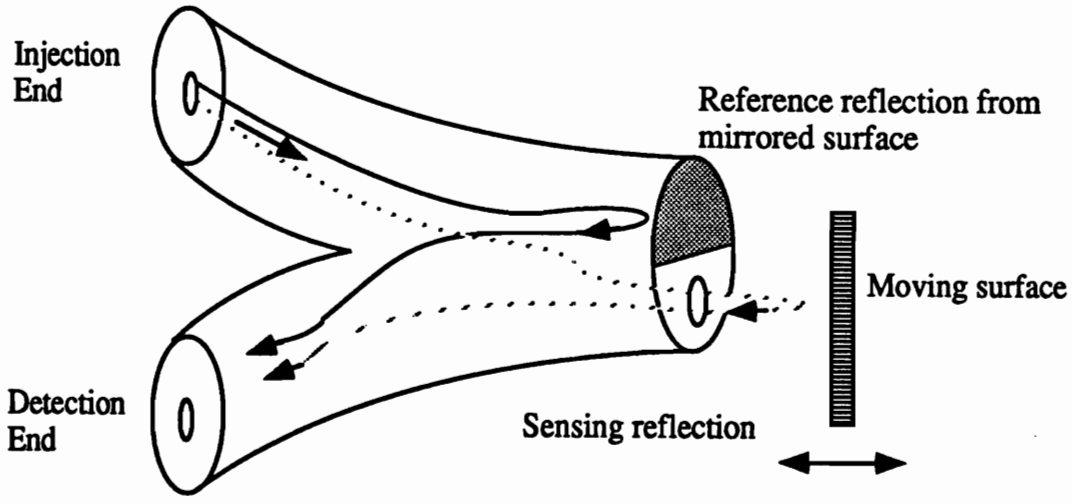

Figure 24. Details of temperature insensitive Michelson interferometer (TIMI).

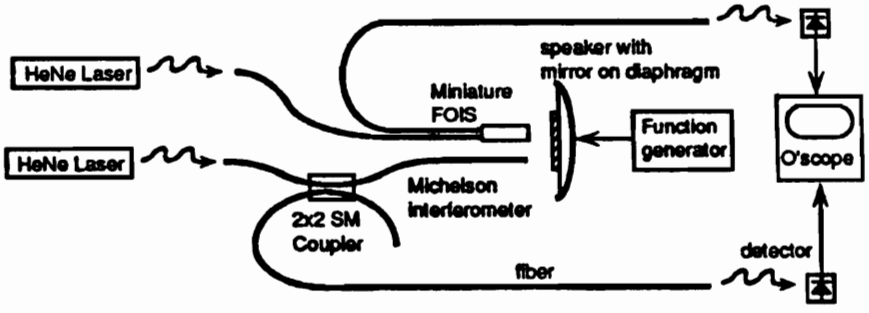

Figure 25. Experimental setup for comparing the TIMI and homodyne Michelson interferometer.

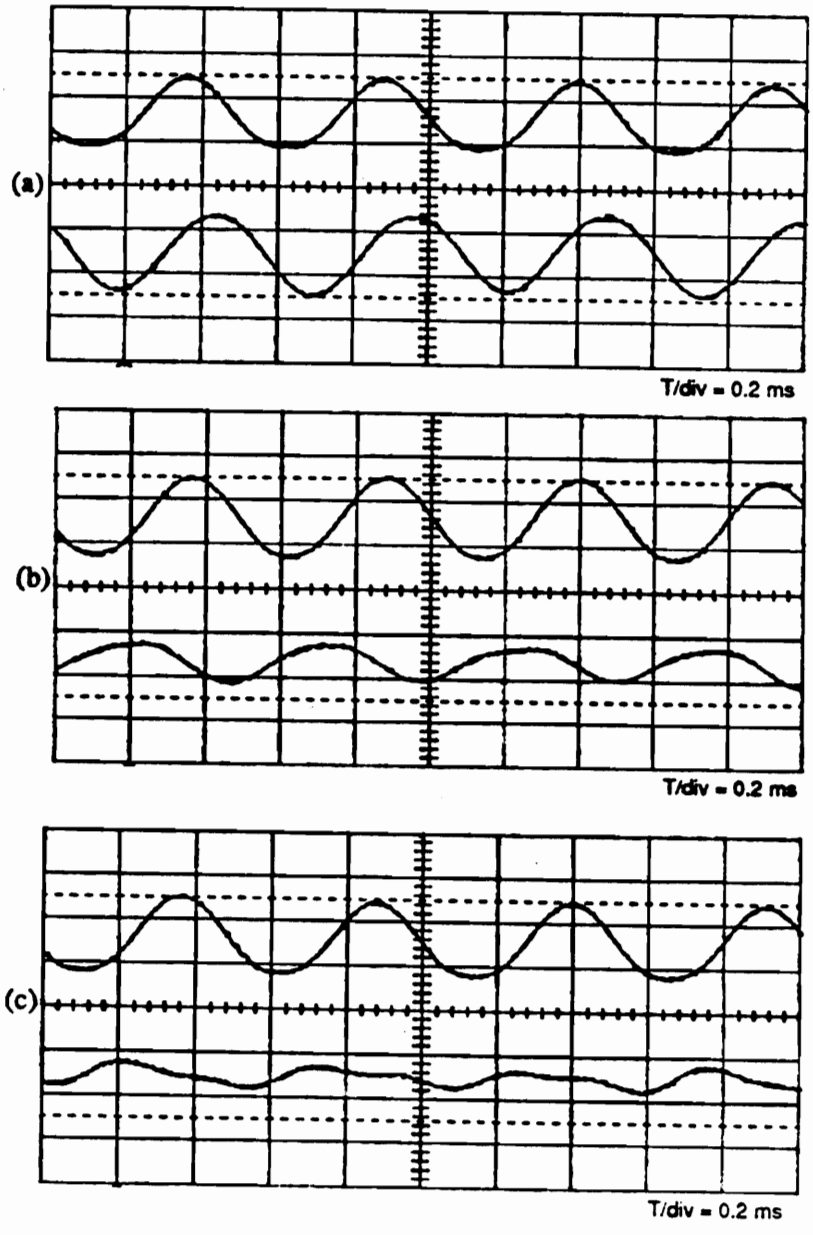

Figure 26. Comparison of the TIMI and homodyne Michelson interferometer for a single fringe: (a) t = 0 ms, (b) t = 100 ms, (c) t = 200 ms.

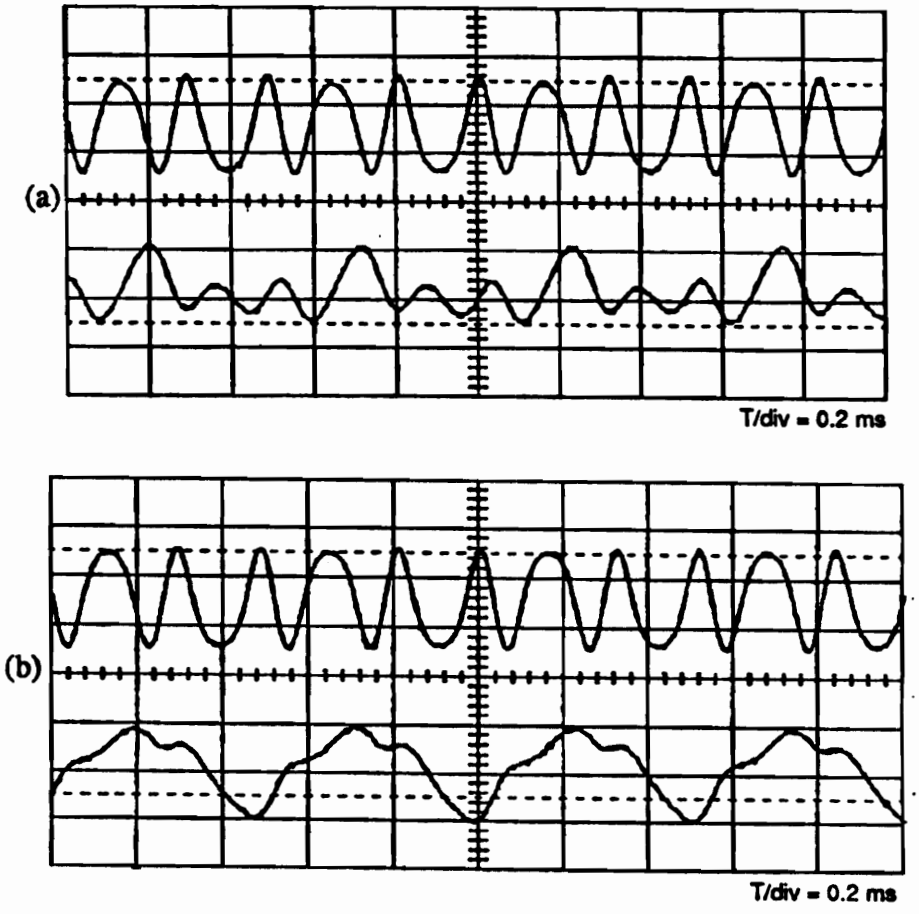

Figure 27. Comparison of the TIMI and homodyne Michelson interferometer for a multiple fringes: (a) t = 0 ms, (b) t = 100 ms.

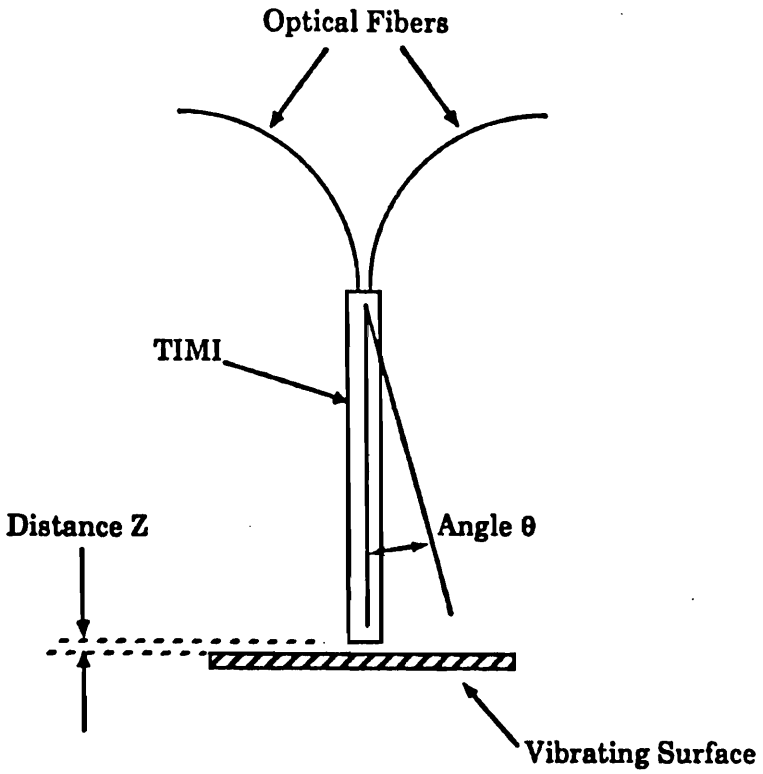

Figure 28. Experimental setup to measure sensor sensitivity to vertical and angular displacements.

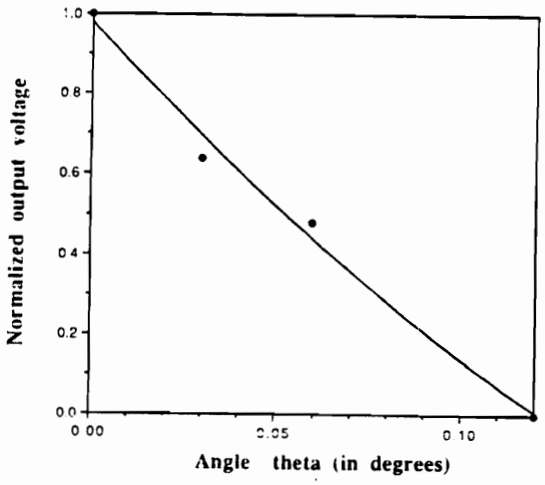

Figure 29. Dependence of output voltage on the angular orientation of the sensor. The graph shows the experimental points and a simple curve fit.

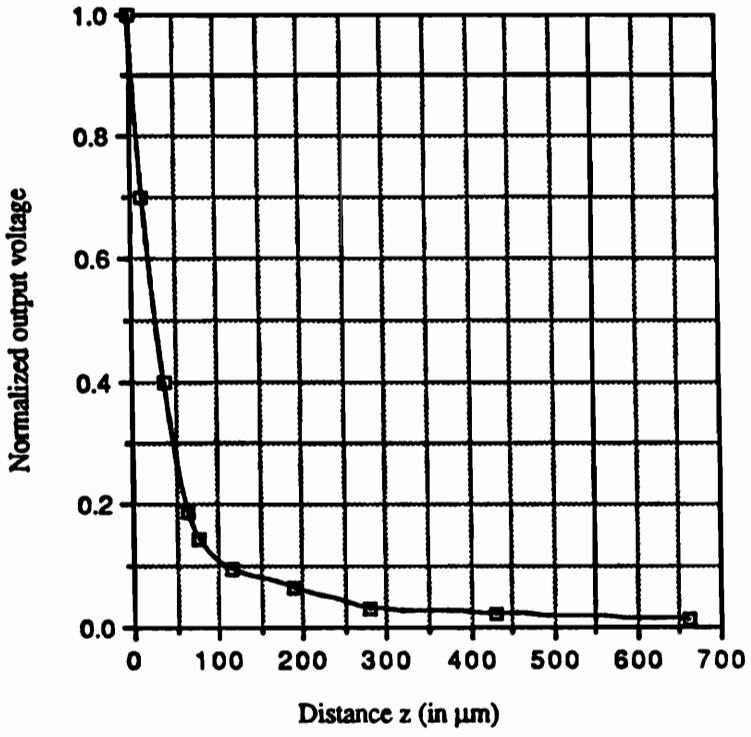

Figure 30. Dependence of output voltage on the lateral displacement of the sensor.

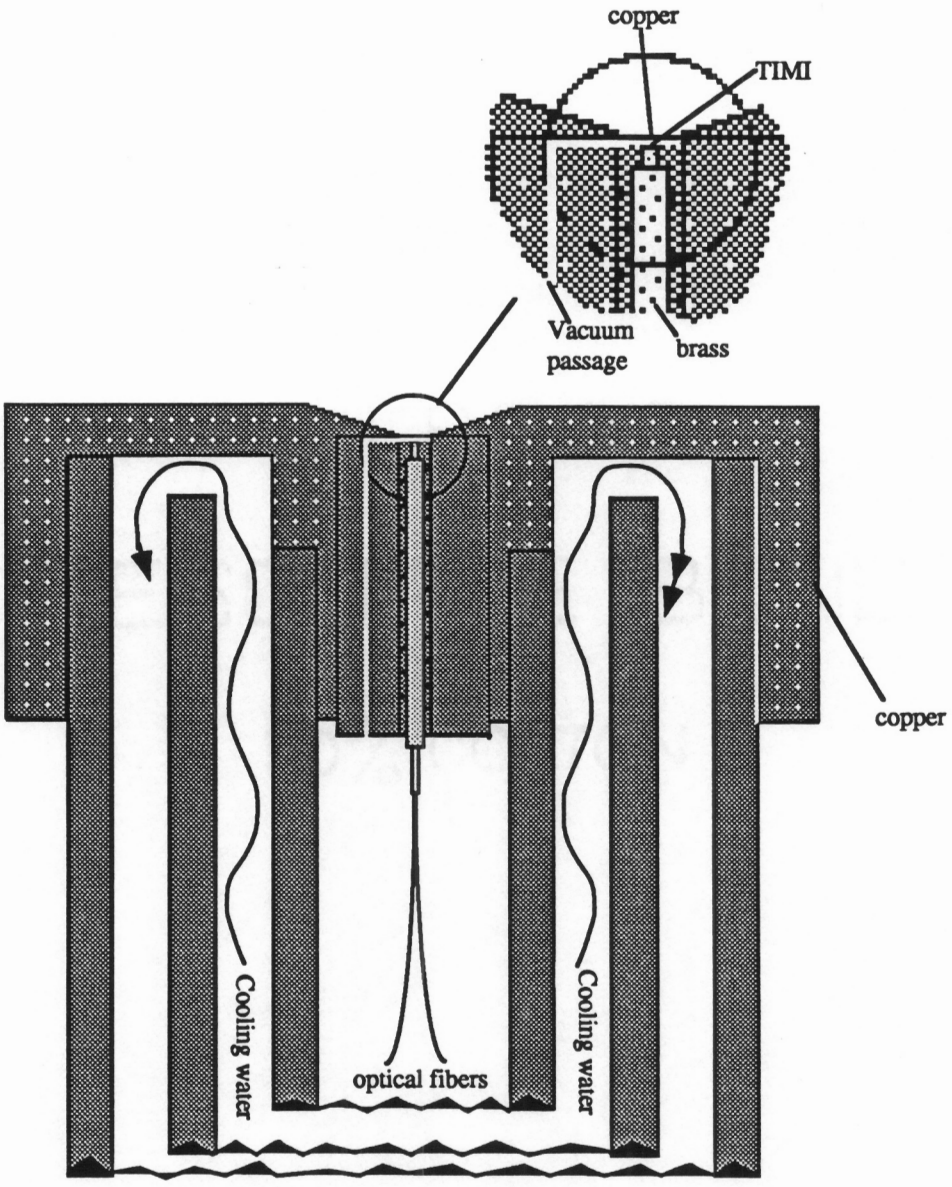

Figure 31. The TIMI mounted into the microphone cylinder, with diaphragm.

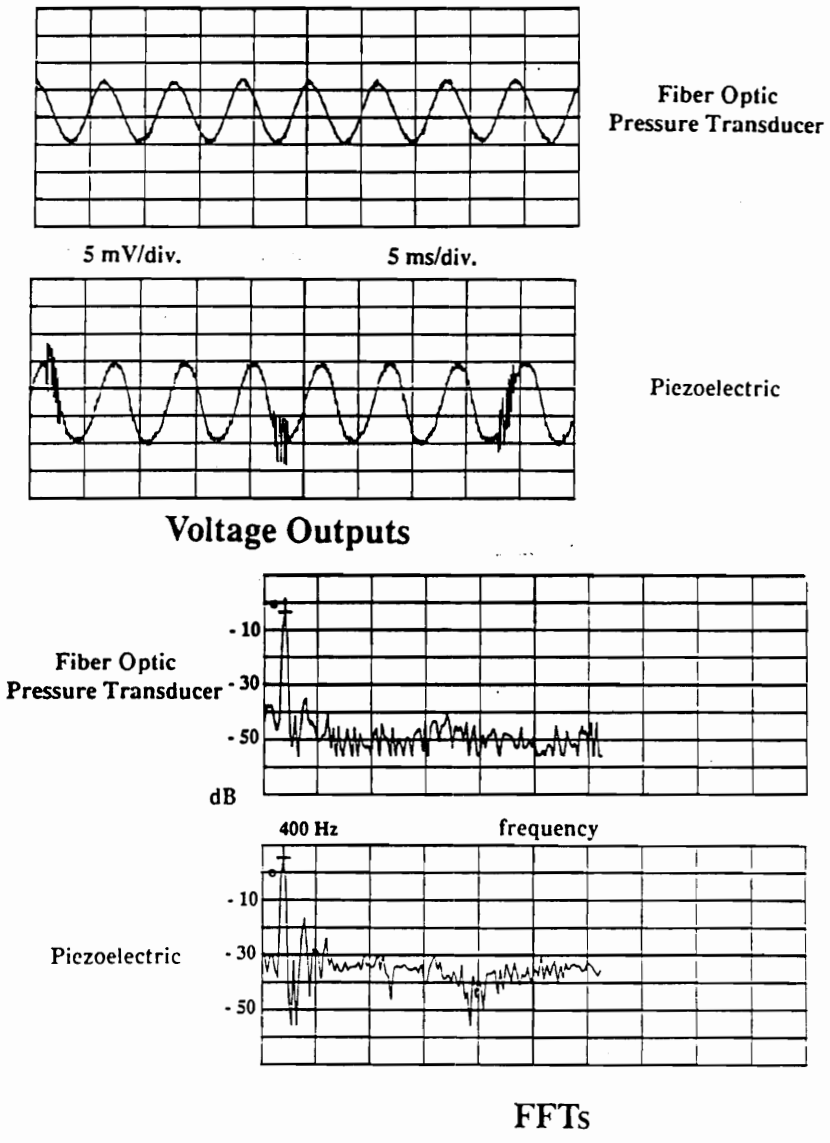

Figure 32. Oscilloscope trace showing output of TIMI and PZT microphones and FFTs.

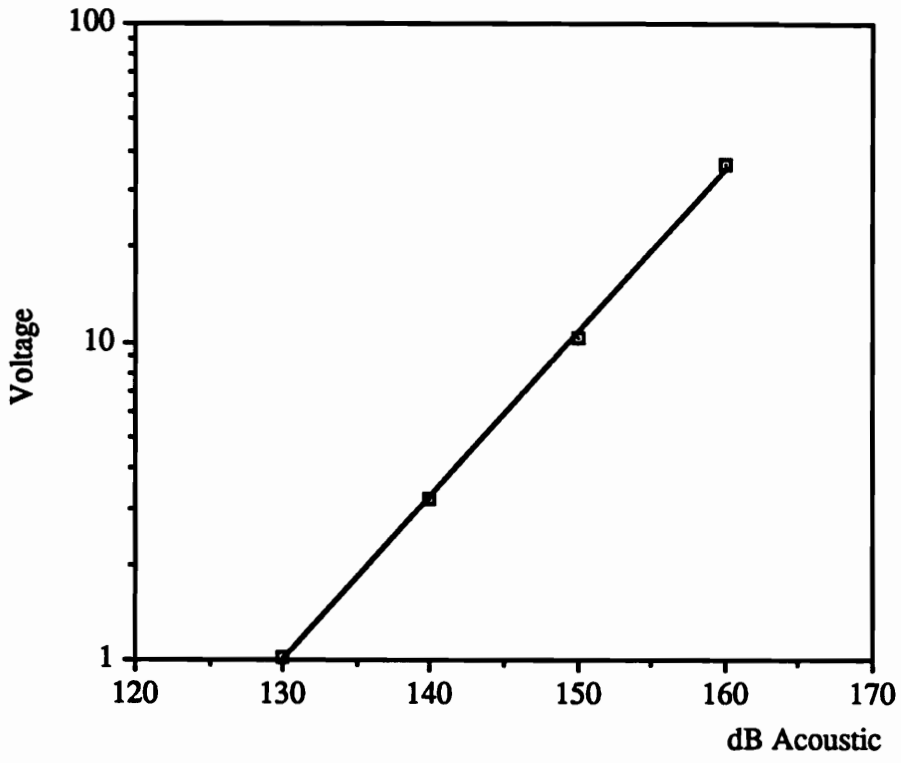

Figure 33. The output of the TIMI transducer is linear with intensity at 1000 Hz.

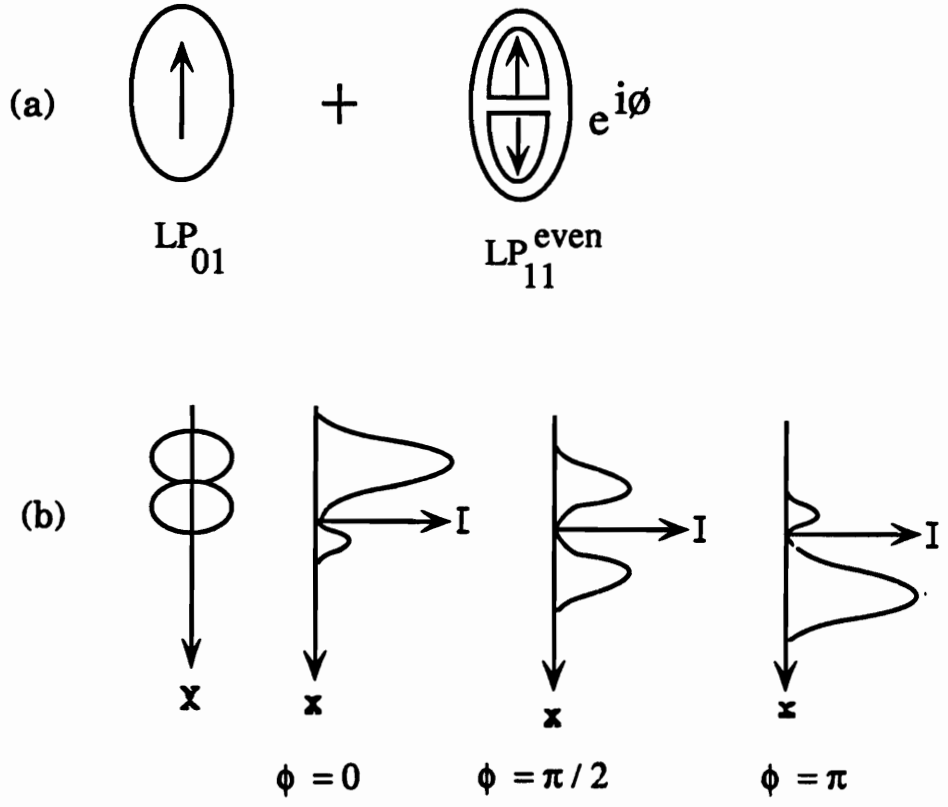

Figure 34. Evolution of the far-field, two-lobe pattern in two-mode, e-core fiber.

(a)

TABLE
DESCRIPTION OF SEGMENTS IN SPLICED-FIBER SENSOR

Fiber	Type	Core dimensions	Cladding diameter
Lead-in	e-core, singlemode @ 633 nm	1.25 μm x 2.5 μm	80 μm
Sensing	e-core, two-mode @ 633 nm	1.25 μm x 2.5 μm	80 μm
Lead-out	circular core, single mode @ 633 nm	4 μm diameter	125 μm

(b)

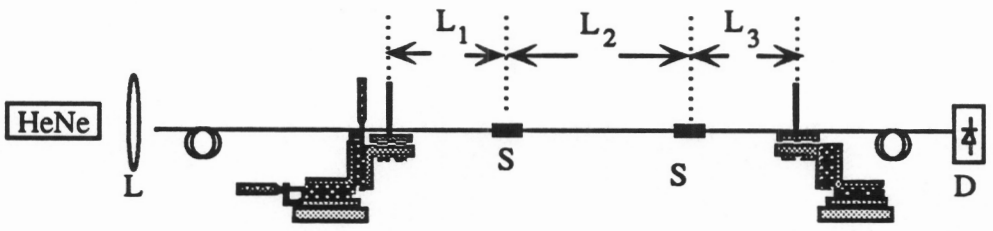

Figure 35. Spliced-fiber sensor. (a) description of fiber segments, (b) schematic of experimental setup. L_1: length of lead-in fiber. L_2: length of sensing fiber. L_3 length of lead-out fiber. L: Lens, S: Splice, and D: Detector.

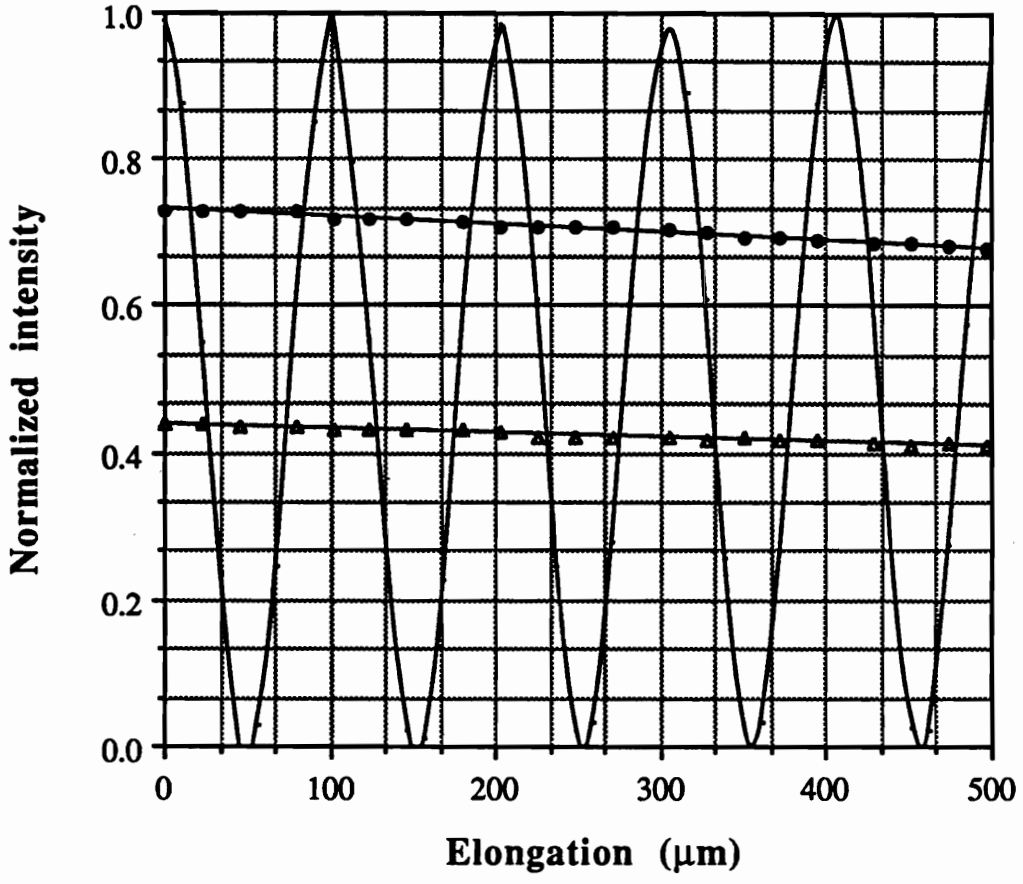

Figure 36. Intensity variation at sensor output. •: strain in lead-in fiber. Δ: strain in lead-out fiber. No symbol: strain in sensing fiber.

TABLE
FIBER LENGTHS IN SPLICED-FIBER SENSORS

Sensor #	L_1(cm)	L_2(cm)	L_3(cm)
1	23.5	11.0	50.0
2	24.0	21.5	38.0
3	24.0	24.0	36.0
4	24.2	41.0	18.0

TABLE
RESULTS OF STATIC STRAIN MEASUREMENT

Sensor #	$(\Delta L)_{2\pi}$: Experimental	$(\Delta L_2)_{2\pi}$: Calculated	Error
1	393.7 μm	101.9 μm	0.3 %
2	266.7 μm	111.1 μm	9.3 %
3	241.3 μm	107.0 μm	5.3 %
4	165.1 μm	99.4 μm	2.2 %

Figure 37. Table (a): fiber lengths in spliced-fiber sensors. Table (b): results of static strain measurement.

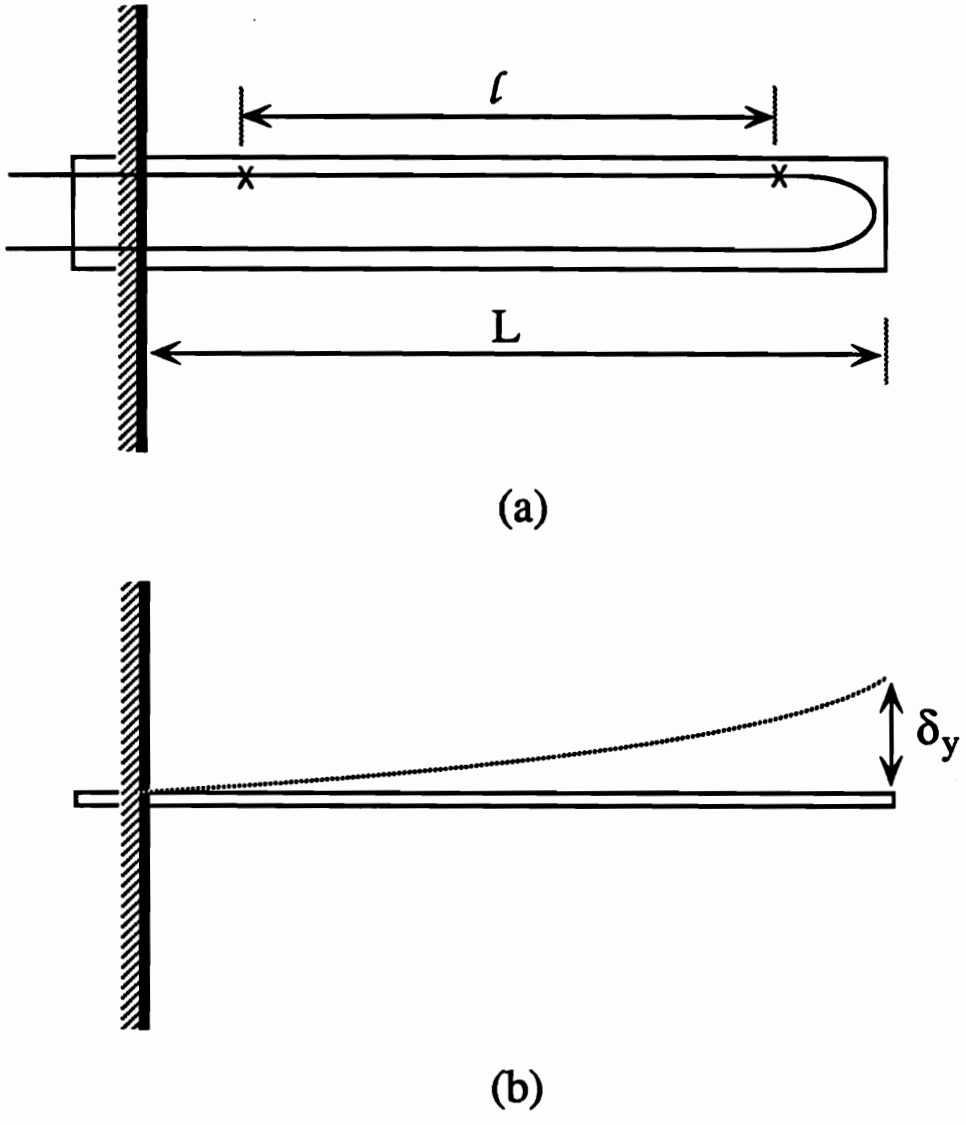

Figure 38. Schematic of fiber optic sensor attached to a cantilever beam. (a) Side view. (b) Top view.

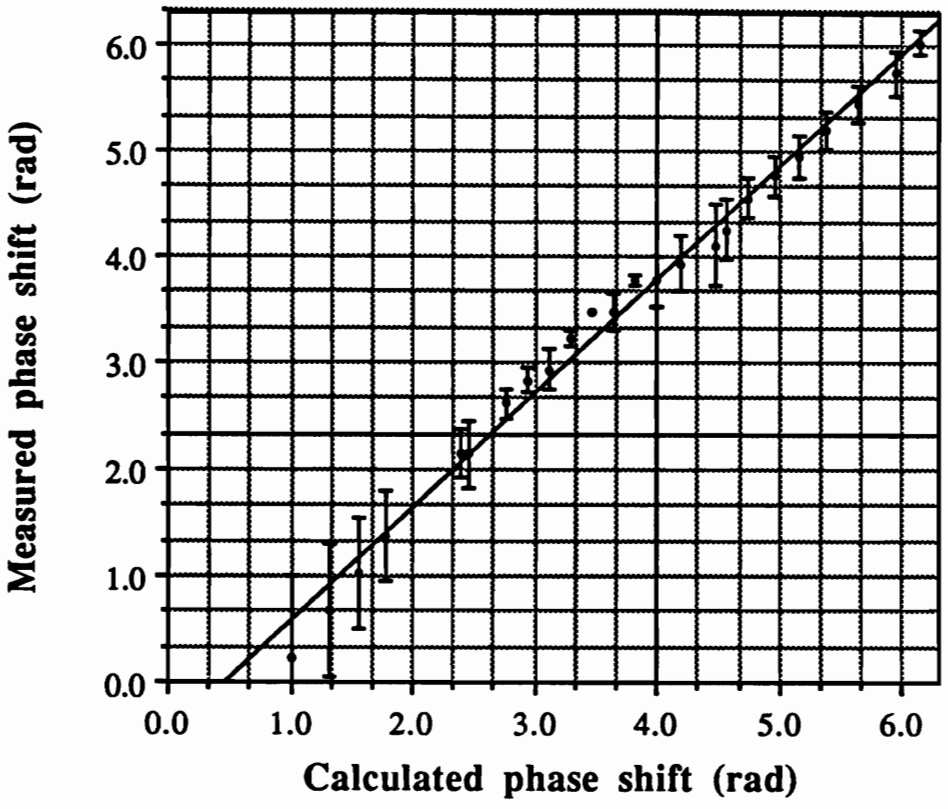

Figure 39. Phase-shift measurement in cantilever beam, from experiment in Figure 38.

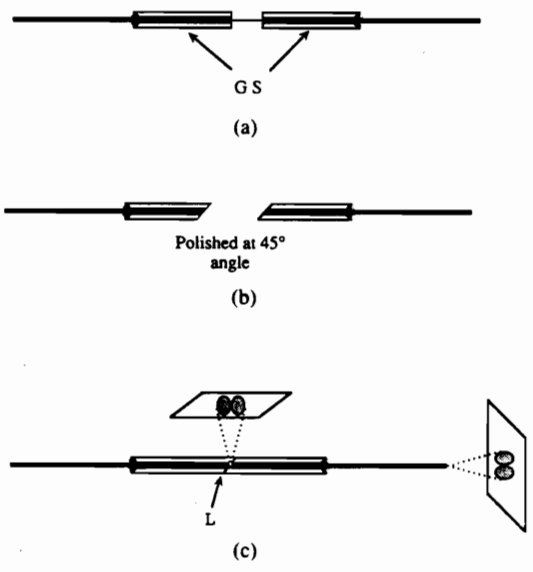

Figure 40. Fabrication procedure for the 45° splitter recombiner. L: Liquid with refractive index = 1.4. GS: Glass slides.

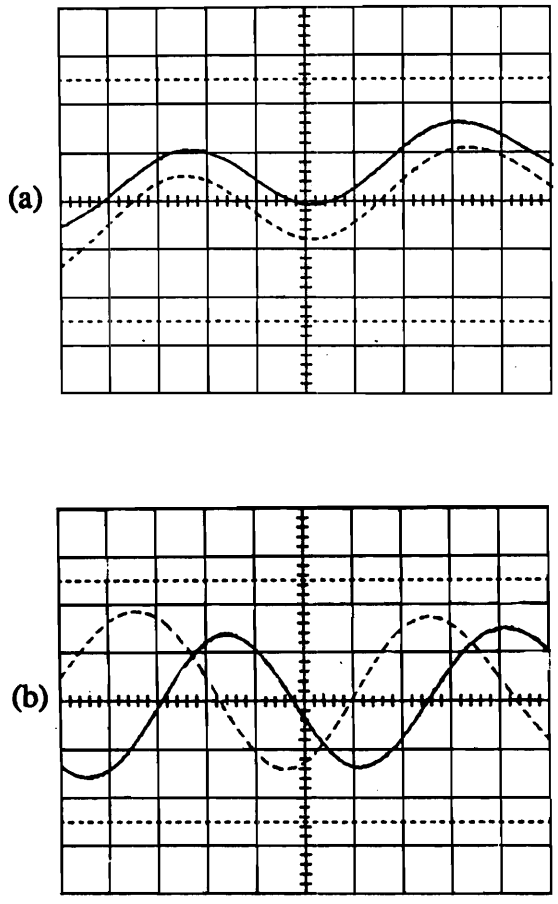

Figure 41. Oscilloscope trace of sensor output: (a) Signals are in phase. (b) Tweaked output leads to quadrature-phase shifted signals.

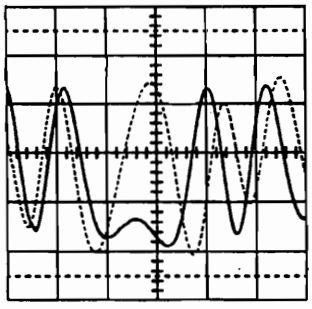

Figure 42. Oscilloscope trace of sensor output showing leading and lagging of the tweaked sensor operated in the nonlinear range.

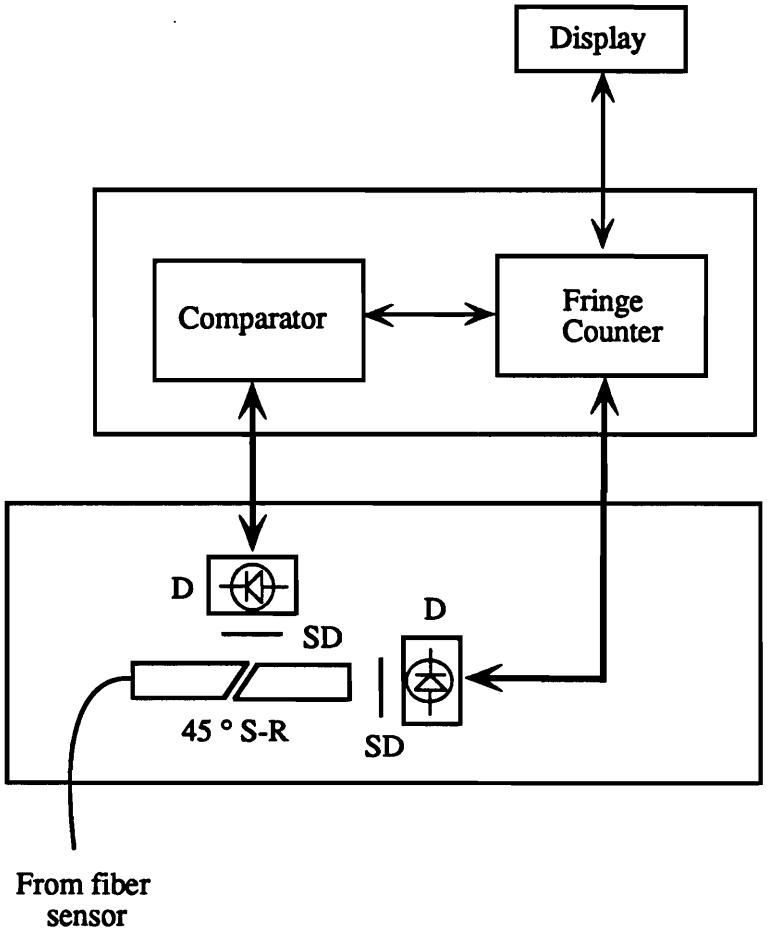

Figure 43. Compact detection scheme for processing the output signals.

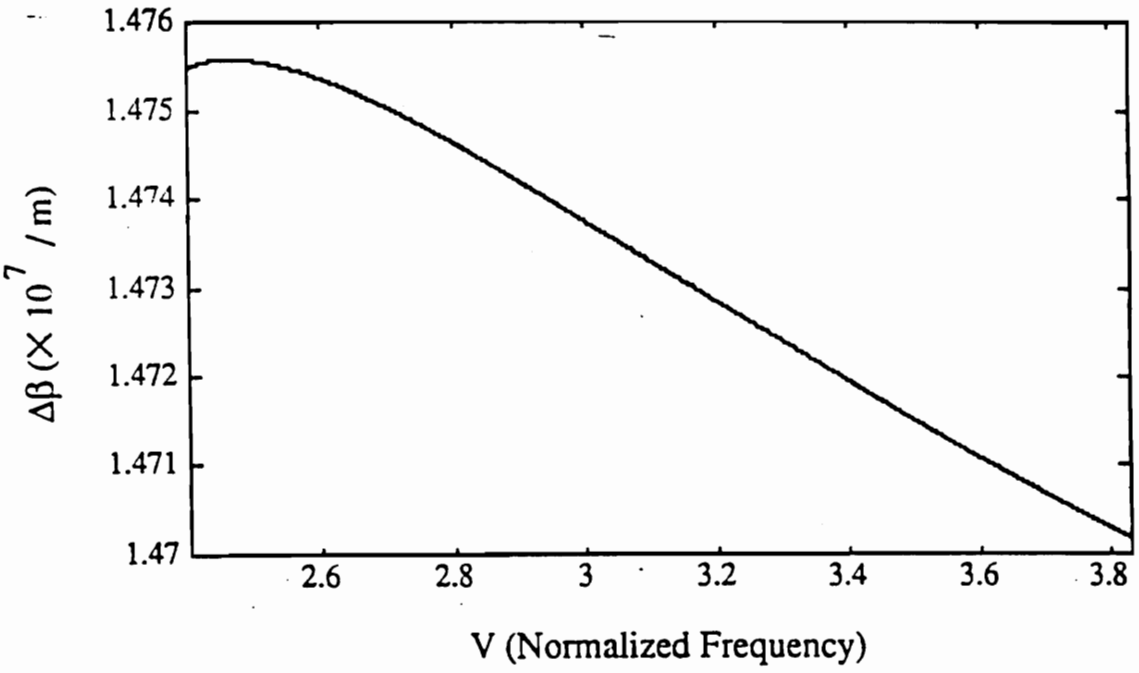

Figure 44. Variation of the differential propagation constant as a function of normalized frequency. $n_1 = 1.5$, $n_2 = 1.47$.

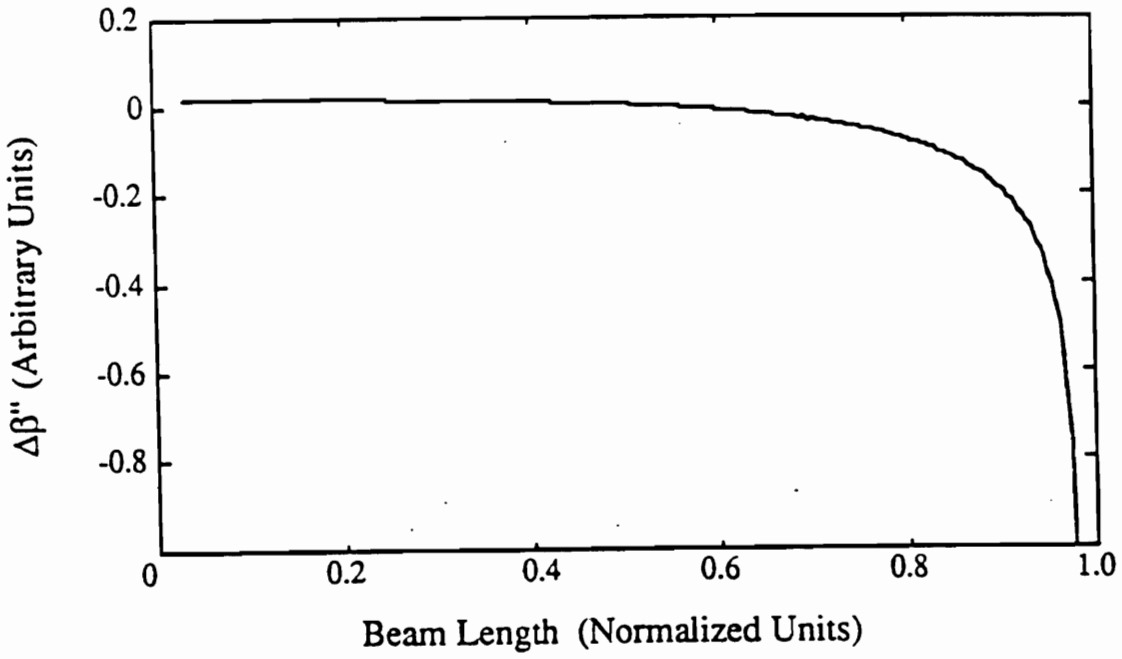

Figure 45. Variation of weighting function $\Delta\beta''(x)$ with length for a linear taper.

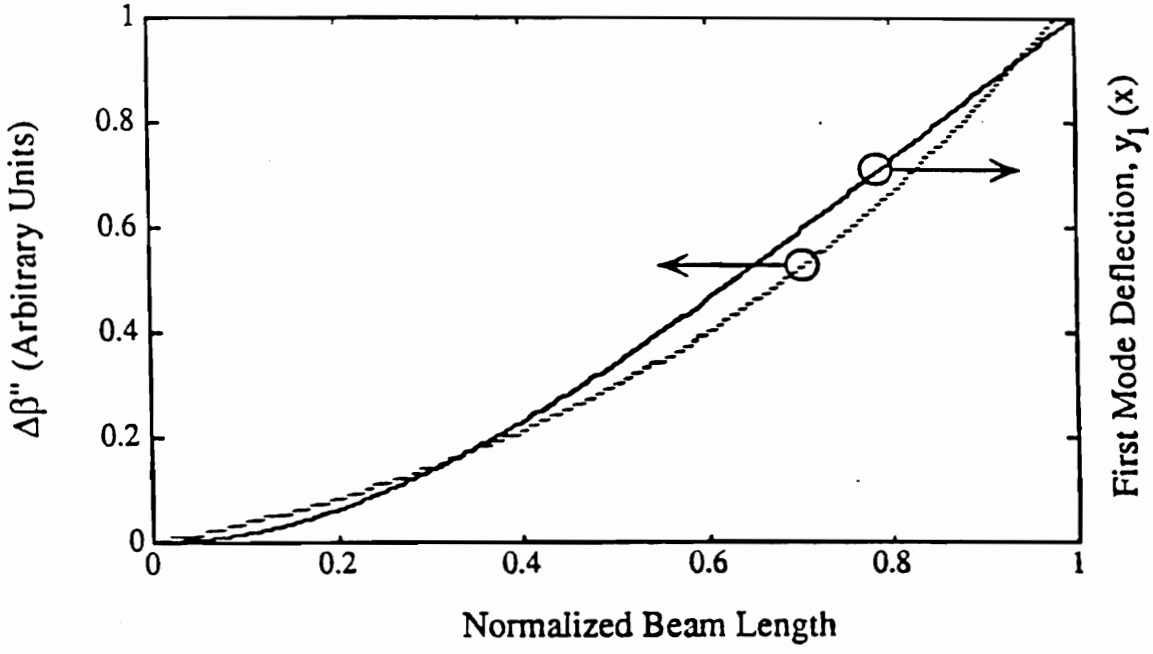

Figure 46. Superposition of weighting function and the first vibration mode shape of a clamped-free beam and a linear fiber taper (a_{min} = 1μm, a_{max} = 1.2 μm) as a function of normalized beam length.

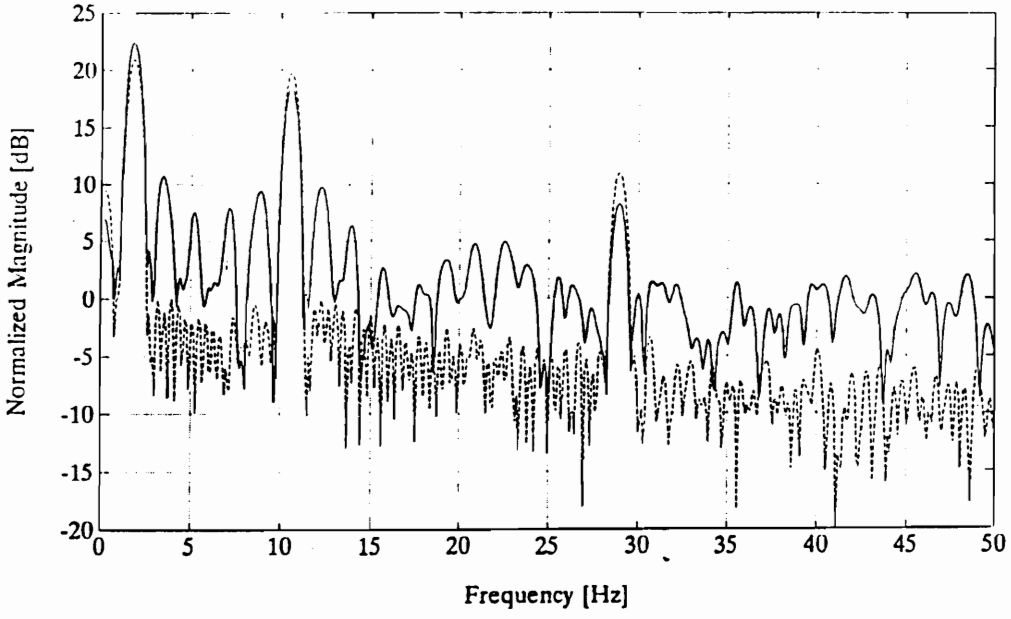

Figure 47. Fast Fourier transform of output signals for clamped-free beam comparing conventional e-core fiber sensor and piezoelectric sensor. Solid line: Fiber sensor output. Dashed line: Piezo-electric output.

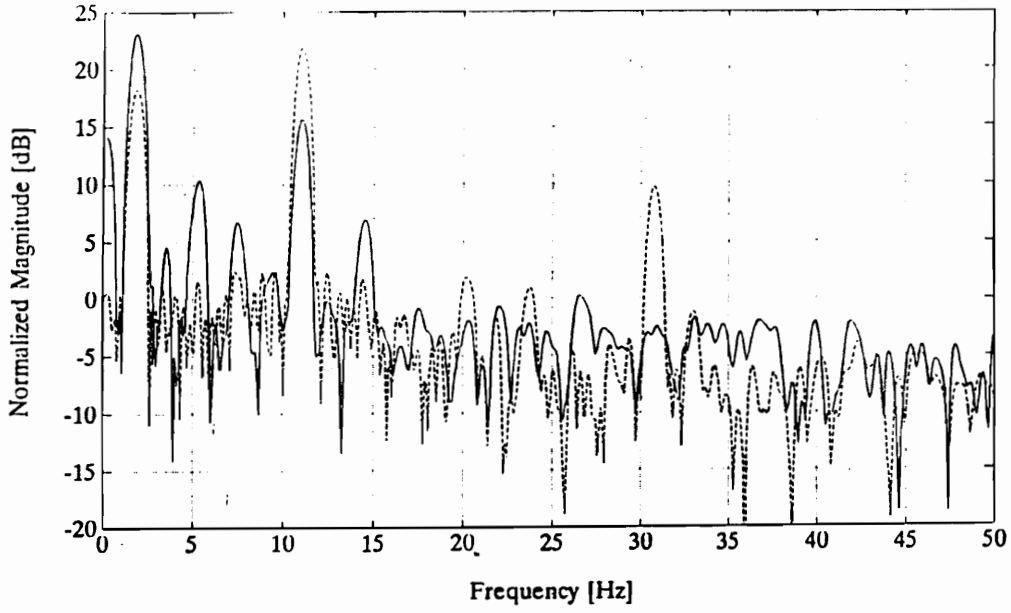

Figure 48. Fast Fourier transform of output signals for clamped-free beam comparing tapered e-core fiber sensor and piezoelectric sensor. Solid line: Fiber sensor output. Dashed line: Piezo-electric output.

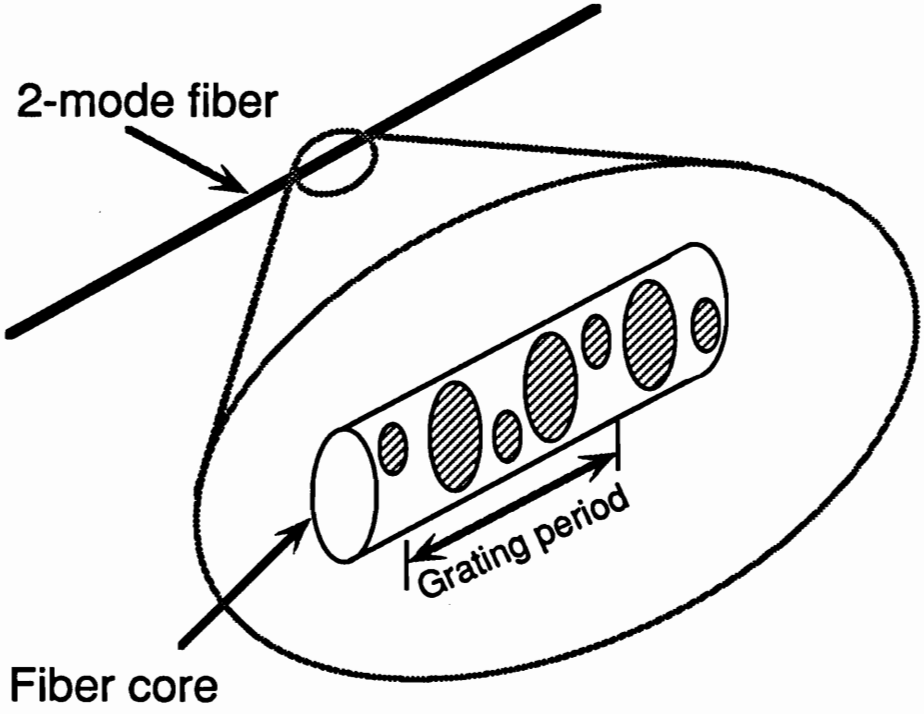

Figure 49. Photo-induced refractive-index changes in a two-mode fiber.

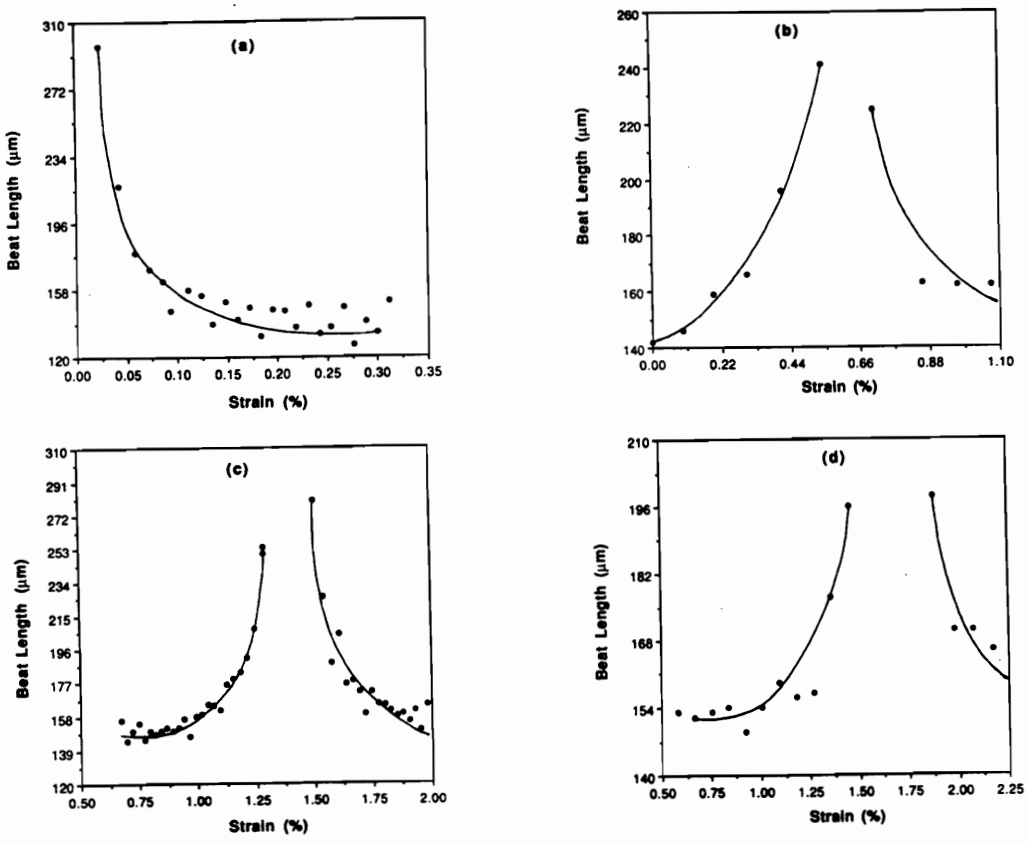

Figure 50. Experimental results showing variation of beat-lengths with strain induced on a fiber with grating. (a) Fiber with no strain during grating writing. (b) Fiber with 0.7% strain. (c) Fiber with 1.4 % strain. (d) Fiber with 1.8% strain. Filled circles are experimental data points, solid lines are best fits. Experimental error in beat-length measurement is 5 μm.

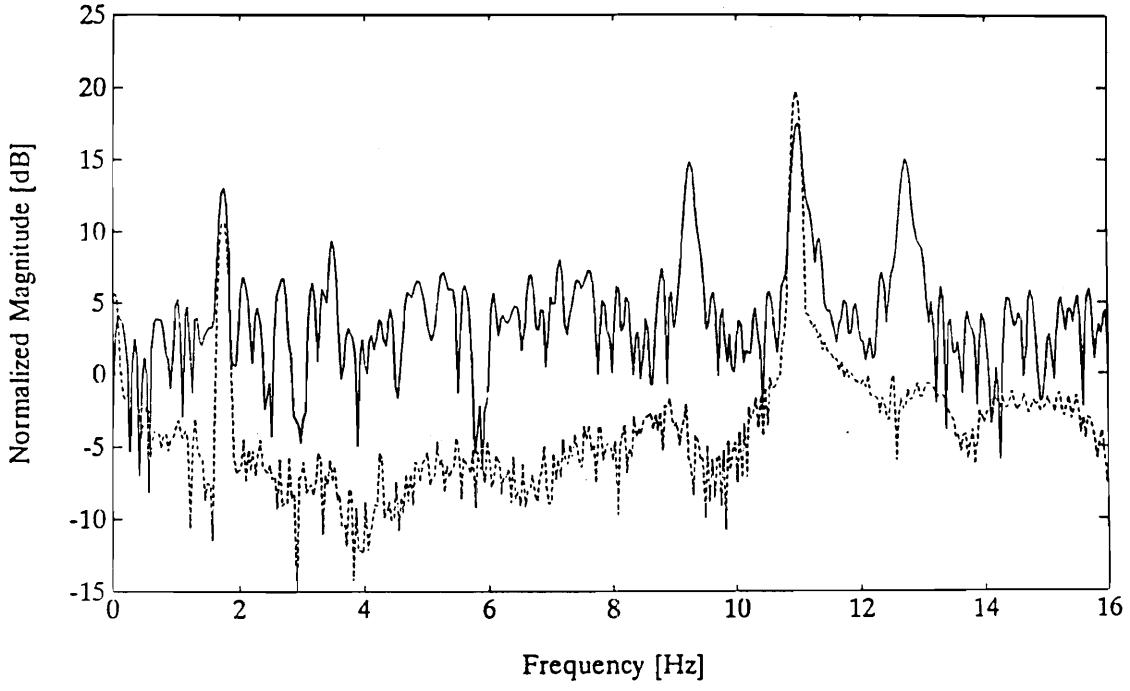

Figure 51. Fast Fourier transform of output signals from a conventional e-core, two-mode fiber sensor and a piezo-electric sensor attached to the beam. First vibration-mode frequency is 1.78 Hz and second vibration-mode is seen at 11.2 Hz. Solid line: Fiber sensor output. Dashed line: Piezo-electric output.

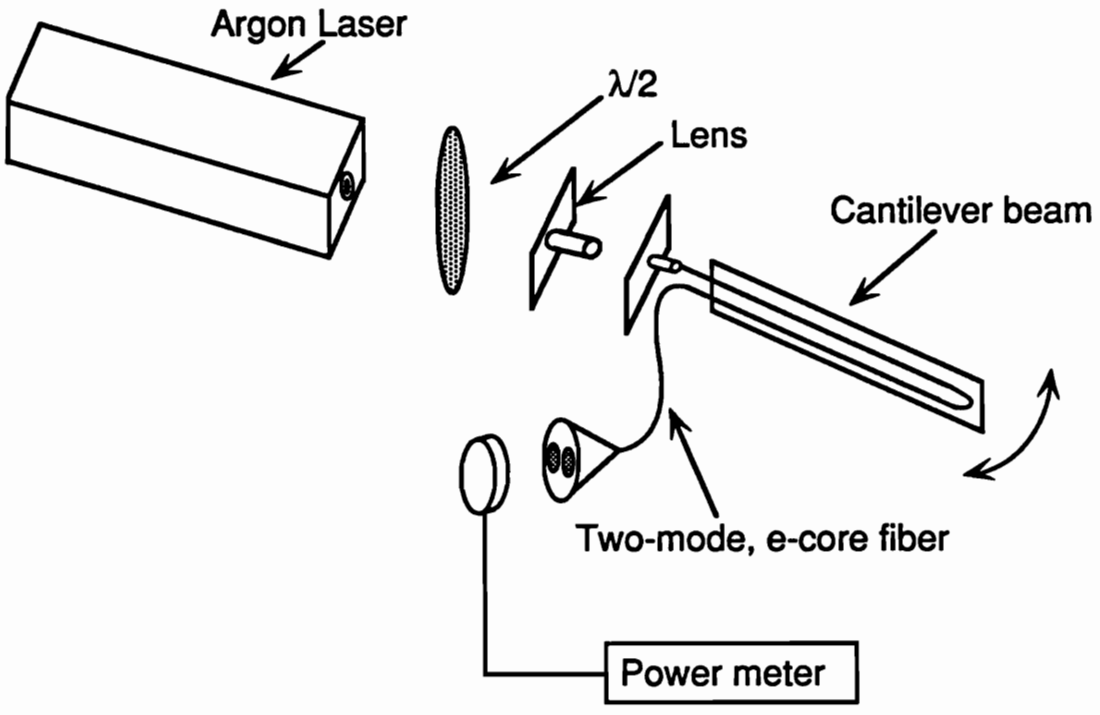

Figure 52. Experimental setup for writing spatially-weighted gratings in two-mode, elliptical-core fibers. The beam may be placed in any mode shape of interest.

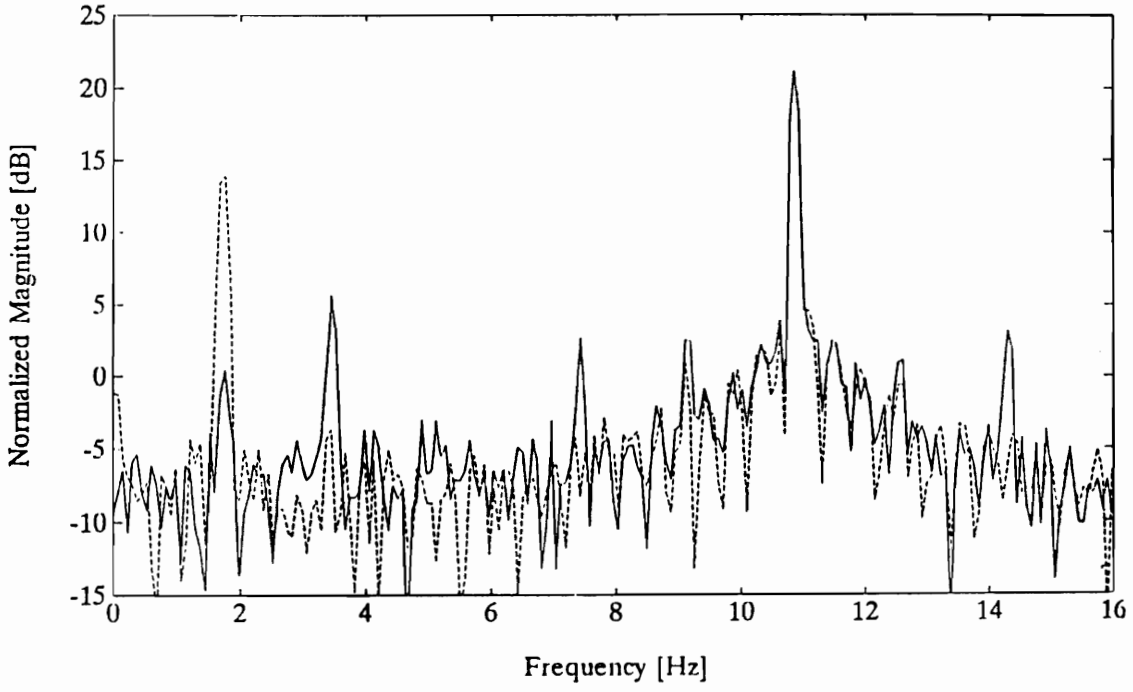

Figure 53. Fast Fourier transform of output signals from a grating-induced, second-mode enhanced, e-core, two-mode fiber sensor and a piezo-electric sensor attached to the beam. The first mode is suppressed by the fiber sensor by 15 dB when compared to the relative signal levels of conventional e-core fiber sensor experiments. Solid line: Fiber sensor output. Dashed line: Piezo-electric output.

Vita

Kent Austin Murphy was born on August 26, 1958 in Lynchburg, Virginia. He attended classes at Virginia Western Community College while working as a technician at ITT, Roanoke, Virginia. He received the Bachelor of Science degree (1986) in Engineering Science and Mechanics and the Master of Science degree (1989) in Electrical Engineering both from Virginia Polytechnic Institute and State University.

Mr. Murphy worked for four years in the research area of fiber optic components at ITT. He worked as an undergraduate for one year, graduate student for one year, research associate for two years, and a research scientist for three years at the Fiber and Electro-Optics Research Center (FEORC), at Virginia Polytechnic Institute and State University. His research interests included fiber optic sensors, devices and components.

Mr. Murphy is a member of the Optical Society of America (OSA), the Society of Photo-Optical Instrumentation Engineers (SPIE), and a Senior Member of the Institute of Electrical and Electronic Engineers (IEEE). He also won the 1991 Meritorious Contribution: Sensors for Smart Materials and Structures, from The International Society for Optical Engineering.